

# **MODELLING OF WELDMENT MICROSTRUCTURE IN NON-AGE HARDENING AL-BASED ALLOYS**

**Guowei Zhang**

A thesis submitted to The University of Birmingham for  
the degree of Master of Philosophy

Department of Metallurgy and Materials

School of Engineering

The University of Birmingham

April 2015

UNIVERSITY OF  
BIRMINGHAM

**University of Birmingham Research Archive**

**e-theses repository**

This unpublished thesis/dissertation is copyright of the author and/or third parties. The intellectual property rights of the author or third parties in respect of this work are as defined by The Copyright Designs and Patents Act 1988 or as modified by any successor legislation.

Any use made of information contained in this thesis/dissertation must be in accordance with that legislation and must be properly acknowledged. Further distribution or reproduction in any format is prohibited without the permission of the copyright holder.

## Acknowledgement

First, I would like to thank China Scholarship Council (CSC) supporting my study in UK, and thank to Department of Metallurgy and Materials at University of Birmingham to provide the facilities.

Second, I would like to thank my supervisor, Dr. Martin Strangwood and Prof. Moataz Attallah. During my study, whenever I had problems, my supervisor Martin could always give me valuable suggestions with patience. Special thanks to my best friends Frank and Carl to give me help in both my life in UK and study. Thanks to friends in the phase transformation and modelling group: Xi, Jinlong, Fei, Peter, Dayue. I would like to thank Paul, Frank, and Jeff for their help.

Lastly, I would like to thank my beloved wife and my parents for their love and support.

## **Abstract**

Aluminium-magnesium (5xxx) alloys have excellent properties such as: high strength to weight ratio, good formability, good corrosion resistance and good weldability. This results in an increasing use of 5xxx alloys in the automotive industry. Fusion welding is a very important joining technique and mechanical properties can be affected during the welding process. In order to model the microstructure and mechanical property evolution during welding, the microstructure and property changes for samples after isothermal heat treatment and welding need to be studied.

In the current study, the microstructure of an as-received material (AA5083 H22) was characterised; the softening kinetic was studied under isothermal heat treatments; the hardness and microstructure in the heat affected zone (HAZ) were studied (in chapter 6); and a method for predicting the thermal profile in HAZ was built based on numerical method using Comsol software (in chapter 7).

It was found that recrystallisation played the most important role during annealing for AA 5083 H22. The activation energy increased linearly with the fraction of recrystallisation from 126 kJ/mol to 150 kJ/mol. There was a transit point for the Avrami exponent, which varied from under 1 to about 1.9 after the transit point.

In the HAZ, the mechanic property (hardness) decrease was mainly caused by recrystallisation as well. The average grain size only increased by 1.3  $\mu\text{m}$  from the full recrystallisation region to the region near to the fusion boundary, which has little effect on the hardness decrease. The hardness increased near to the fusion boundary, which

could be attributed to the dissolution of second phase particles. The numerical method using Comsol software could predict the thermal profiles well, and the modelled size of the fusion zone was close to the size of real weldment fusion zone.

# Contents

Chapter 1 Introduction.....	1
Chapter 2 Literature review.....	3
2.1 Al-Mg based alloys.....	3
2.1.1 Microstructure Al-Mg wrought alloys.....	3
2.1.2 Strengthening mechanisms in Al-Mg alloys .....	11
2.2 Annealing phenomena in Al-Mg Alloys .....	16
2.2.1 Recovery.....	17
2.2.2 Recrystallisation .....	20
2.2.3 Grain growth.....	34
2.2.4 Techniques to reveal annealed microstructures .....	36
2.3 Thermal cycle in the heat affected zone (HAZ) of the weldment .....	39
2.3.1 Heat source .....	41
2.3.2 Comparison of analytical and numerical methods.....	47
2.4 Project aims .....	48
Chapter 3 Experimental methods .....	49
3.1 Materials .....	49
3.2 Sample preparation.....	50
3.3 Heat treatment .....	52
3.4 Microstructure investigations .....	53
3.4.1 Optical Microscopy .....	53
3.4.2 Electron Microscopy .....	54
3.4.3 Differential Scanning Calorimetry (DSC).....	54
3.5 Mechanical test.....	55
3.6 Software used in this project .....	55
Chapter 4 Characterisation of the as-received Material .....	56
4.1 Second phase particles.....	56
4.1.1 Composition .....	56
4.1.2 Second phase particle distribution.....	59
4.2 Grain microstructure characterisation .....	60

4.2.1 Grain size.....	60
4.2.2 Texture of as-received AA5083 .....	61
4.3 Summary .....	63
Chapter 5 Annealing phenomena .....	65
5.1 The effects of second phase particles on the DSC curve.....	65
5.2 Recrystallisation studied by DSC .....	68
5.3 Recrystallisation studied by Micro-hardness.....	72
5.3.1 Activation energy .....	76
5.3.2 Avrami exponent .....	77
5.4 Microstructure characterisation during annealing .....	79
5.5 Summary .....	82
Chapter 6 Microstructure analysis in HAZ.....	83
6.1 Recrystallisation in the HAZ .....	84
6.2 Grain growth.....	89
6.3 Summary .....	90
Chapter 7 Thermal profile modelling.....	91
7.1 Analytical method .....	91
7.1.1 Input parameters for the analytical method .....	93
7.1.2 Results of the analytical method.....	94
7.2 Numerical model method .....	97
7.2.1 The process of building the numerical model.....	97
7.2.2 Results of the numerical model .....	99
7.3 Summary .....	101
Chapter 8 Conclusions and future work .....	102
8.1 Conclusions .....	102
8.2 Future work .....	103
Reference.....	105

## Chapter 1 Introduction

With the environmental and economic concerns, there is a trend to produce lighter weight car to reduce the fuel consumption. Aluminium as a light metal is the ideal replacement for the steel and casting iron used in cars, because of its good properties such as: high strength to weight ratio, good formability, good corrosion resistance and so on. Aluminium-magnesium (5xxx) alloys as a group of non-age hardening Al-based alloys started to be used for the inner panel application in vehicles.

With increasing use of aluminium-magnesium alloys, joining aluminium alloys sheets need to be considered. There are two method to join the sheets: riveting (mechanical fastening) and welding. The riveting is mainly used in body panel joining, for inner panel joining, the welding especially fusion welding needs to carry out. So there is a requirement to have a better understanding of the microstructure and mechanical property evolution during welding process.

With the concern of economy, computer models need to be developed to predict effects of welding process on the mechanical property variation in HAZ. Although the models in the heat affected-zone (HAZ) of aluminium alloys have been developed for a long time, they mainly study heat-treatable alloys and focus on the effect of precipitation on the mechanical properties. There are few models focusing on the non-heat-treatable aluminium alloys. There is a need to build and develop model of properties variation in HAZ for non-heat-treatable aluminium alloys. In fact, the properties variation in HAZ of non-heat-treatable is more complex because of the annealing phenomena (recovery,



recrystallisation, grain growth and solid solution strengthening). For a successful model, it is required to have a comprehensive understanding about the mechanism of possible annealing phenomena and then obtain correct and accurate input parameter data.

The aim of this project is to study the annealing phenomena of Al-Mg alloys for the isothermal heat treatment and non-isothermal process in heat-affected zone (HAZ) and obtain the essential input parameters data for future microstructure modeling work in HAZ.

## Chapter 2 Literature review

### 2.1 Al-Mg based alloys

As the most abundant metal in the earth, aluminium has about 200 years history since it was first produced by Sir Humphry Davy in 1809. Due to the lack of commercial electricity generation, extraction was very hard until the early 1880s. The Hall-Héroult electrolytic process was developed in 1888 and provided an economic method for the extraction; this method is still the basis for the production.

Properties, such as low density, high specific strength and high corrosion resistance, are beneficial to application of Al and Al-based alloys in the fields of building construction, packaging, transportation and electrical conductors. Aluminium and its alloys can be divided into cast alloys and wrought alloys with respect to the fabrication process, and further divided into heat-treatable alloys and non-heat-treatable alloys based on composition. Composition is often used to influence the properties of both cast and wrought alloys. Alloys are classified by the major alloying elements that they contain.

#### 2.1.1 Microstructure Al-Mg wrought alloys

##### 2.1.1.1.a Composition

This Al-Mg alloys were developed in the 1930s to meet the requirements of good mechanical properties, weldability, formability and corrosion resistance. This series of alloys are based on the main alloying element Mg. From the Al-Mg phase diagram (Fig. 2.1), it is shown that the maximum solid solubility of magnesium in aluminium is about 2 wt % at room temperature, and 17.4 wt % at 723 K. However, wrought alloys

containing from 0.8 wt % to slightly more than 5 wt % magnesium are widely used [1].

At higher Mg levels,  $\text{Al}_3\text{Mg}_2$  can precipitate along grain boundaries and increase the susceptibility to intergranular corrosion and stress corrosion cracking (SCC) [2].

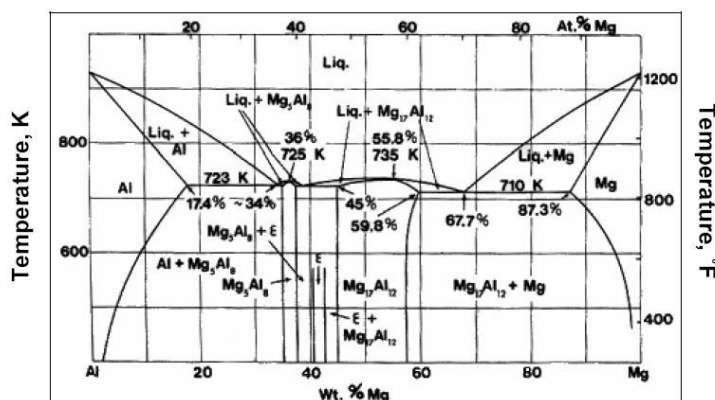


Fig. 2.1 The binary Al-Mg equilibrium diagram [3]

Apart from Mg, other minor alloying elements are also chosen to be added in this series alloys, such as: Fe, Mn, Cr, Cu and Si. Fe is added to increase the recrystallisation temperature and reduce the grain growth rate; Mn and Cr are added to reduce corrosion caused by Fe; Cu is added to reduce the pitting corrosion; Si is used to increase the casting fluidity [3].

#### 2.1.1.1.b Fabrication of Al-based alloy sheets

Al-based alloy sheets can be produced by many routes, with major difference being in the ingot or slab fabrication step. Traditionally, ingot casting (IC) is applied to produce a rectangular aluminium ingot, then the ingot goes through scalping and homogenising in preparation for the following hot or cold rolling steps. The IC route is expensive, and is not suitable for commercial production. Currently, direct-chill casting (DC) and continuous casting (CC) are widely applied in producing the Al-based alloy sheets.

DC route is a process in which the molten alloy is poured into a mould with a moveable bottom supported by a hydraulic ram. After a crust of solid metal has formed in the mould, the hydraulic ram is moved down so that the ingot can be cooled by water sprays to accelerate the solidification process of the rest of the ingot. The surface of finished DC product can meet the requirements for subsequent rolling work, without scalping.

DC route is a semi- continuous casting route; the real continuous process is CC. In CC the liquid aluminium-based alloy is injected between two water-cooled twin rollers, and this step accomplishes solidification and hot rolling. After the first step, slab or plate is formed, which could be subsequently rolled to produce sheet or foil. Casting and rolling are combined in twin-rolling casting (TRC) route, this is a very productive and economic fabrication method.

Because of the intermediate slab dimensions and heat transfer processes, the cooling rates are different for both routes. The cooling rate has an important effect on the microstructure and the mechanical properties of the alloy. The size of the intermediate slab produced by DC is larger than that of CC. The maximum thickness of DC ingot is around 650 mm and the average cooling rate ranges from 1 to 5 °C/s. The CC route can directly produce aluminium sheet and plate with a thickness range from 3 mm to 10 mm [1], the cooling rate is from 100 to 1000 °C/s.

The cooling rate affects the dendrite arm spacing (DAS); the amount of the alloying elements in solid solution; the size and distribution of the constituent particles; and the texture of the finished sheet. The relationship between the DAS and cooling rate is well

established as:

$$DAS = A Cr^{(-n)} \quad \text{Equation 2.1}$$

where DAS is the dendrite arm spacing, Cr is the cooling rate, A and n are constants.

It can be concluded that DC cast material would have larger DAS values, which results in larger grain size after homogenisation. Although the DAS has important effects on the microstructure of as-cast material, for the rolled sheet, it will not keep this structure any more. To obtain finished sheet, DC slab goes through hot and cold rolling and CC plate goes through cold rolling. The requirements for the final products could be achieved by deformation and following heat treatment.

The difference of solid solution caused by cooling rate could affect the microstructure and the properties. For high cooling rate routes, the diffusion time of alloying elements is shorter than that for slow cooling rates, so that a greater proportion of the alloying element content present can be trapped in solid solution in the  $\alpha$ -Al matrix. This has been investigated through changes in electrical resistivity. The electrical resistivity of AA5182 DC hot band has been measured at 5.882  $\mu\Omega\text{cm}$ , whilst that for CC band after annealing was 6.369  $\mu\Omega\text{cm}$  indicating greater solid solution in the latter case [4]. The results from Zhao et al. [5] showed that the hardness of AA5052 CC plate was 5 Hv higher than that of DC plate for similar percentage reduction and full recrystallisation. For work hardening alloys, solid solution accounts for the increased alloy hardness when the plate is fully recrystallised. The cooling rate could also affect the morphology and number density of second phase particles. For the same composition sheet, particles

compared with DC sheet (shown in Fig. 2.2) [5-7]. These second phase particles generally form during solidification interdendritically. In the case of CC, the short DAS results in a higher density of particles and higher solid solution of alloying elements in the matrix aluminium decreasing the size of the particles. The microstructure of both CC and DC showed this difference [5]. Morris et al. [8-11] studied the effect of fabrication route on the microstructure and texture of final non-aging hardening sheet. They found that the texture evolution during rolling followed the same path for both routes and  $\alpha$  and  $\beta$  fibres were well developed in both routes. However, after annealing, there was a difference with the DC sheet showing stronger recrystallisation texture than the CC sheet. This behaviour could be related to the mechanism of recrystallisation nucleation, for the CC sheet; there are more second phase particles which could stimulate nucleation and result in a more random texture [12].

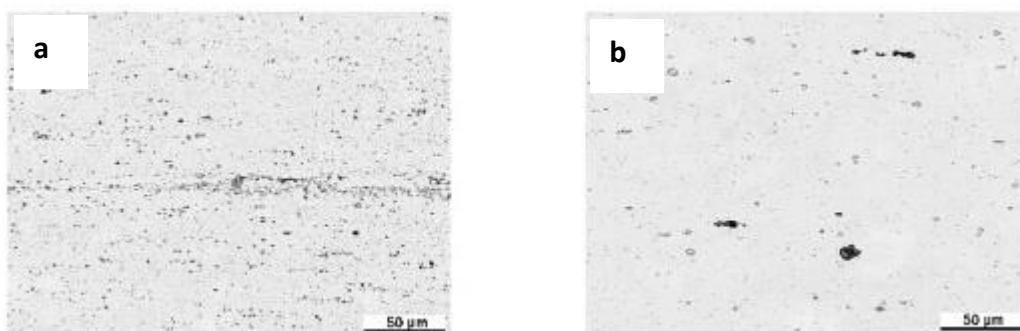


Fig. 2.2 Optical microscope image of second phase particle,(a) CC sample of AA5182, (b) DC sample of AA5182 [8]

#### 2.1.1.2 Second phase particles

Second phase particles could influence the microstructure and properties of the final product. For the AA5xxx, the major function of second phase particles is to control

the grain size. Apart from this effect, large particles could affect the recrystallisation mechanism known as particle stimulated nucleation (PSN).

Potential intermetallic phases in AA5xxx alloys have been summarized by Mondolfo [3] (shown in Table 2.1) and some possible morphologies of common intermetallic phases are listed in Table 2.2. According to the sequence of the formation of second phase, the particles can be divided into constituent particles and dispersoids. Constituent particles are known as primary precipitates, which form during solidification. Dispersoids are the secondary precipitates, which form during thermal processes after casting, and the particles size is smaller than that of constituent particles. Aluminium-based alloys containing Mg and Si and low Fe contents should exhibit a microstructure with  $\alpha$ -Al<sub>8</sub>Fe<sub>2</sub>Si particles, but in direct-chilled castings, the iron had a tendency to precipitate in the  $\beta$ -Al<sub>5</sub>FeSi platelet-like form[3]. It was showed when the ratio of Fe to Si was low, the  $\alpha$ -Al<sub>8</sub>(Fe, Mn)<sub>2</sub>Si intermetallic was more prominent than Al<sub>3</sub>(Fe, Mn), and during preheating and mechanical processing, these phases partially converted to Al<sub>6</sub>(Fe, Mn) [13]. For AA5182 alloy sheet at a low Fe:Si ratio, the main phase formed is Al<sub>6</sub>(Fe,Mn), with a small amount of Al<sub>15</sub>(Fe,Mn)<sub>3</sub>Si<sub>2</sub> (in the annealed condition). Zhao et al. [14] found CC AA5082 in the hot band condition contained more Mg<sub>2</sub>Si particles than DC AA5082.

Table 2.1 Phases formed on casting and aging in aluminium-magnesium alloys

(compositions in wt %) [3]

Mg	Mg<2 %	Mg>2%	Si>0.05%	Cu>0.2%			
	in solid soln.	Al <sub>8</sub> Mg <sub>5</sub>	Mg <sub>2</sub> Si	Al <sub>6</sub> CuMg <sub>4</sub>			
Si	Fe<0.3%	Fe>0.3%, Mg<2%	Fe>0.3%, Mg<<2%, Mn or Cr>0.1 %				
	Mg <sub>2</sub> Si	Al <sub>8</sub> Fe <sub>2</sub> Si	Al <sub>15</sub> (Fe,Mn) <sub>3</sub> Si <sub>2</sub> or Al <sub>13</sub> (Cr,Fe) <sub>4</sub> Si <sub>4</sub>				
Fe	Si<0.3 % Mg>2 %	Si>0.3% Mg<2%	Si>0.3% Mg<2% Mn>0.1%	Si<0.3% Mg>2% Mn>Fe	Si>0.3 % Mg<2 % Cr>0.1 %	Si<0.3 % Mg>2 % Cr>0.1 %	Si<2% Fe>0.3 % Cu<1 %
	Al <sub>3</sub> Fe	Al <sub>8</sub> Fe <sub>2</sub> Si	Al <sub>15</sub> (Fe,Mn) <sub>3</sub> Si <sub>2</sub>	Al <sub>6</sub> (Fe, Mn)	Al <sub>7</sub> (Cr, Fe) <sub>4</sub> Si <sub>4</sub>	Al <sub>7</sub> (Cr, Fe)	Al <sub>7</sub> Cu <sub>2</sub> Fe
Mn	Si<Mg	Si>2 Mg					
	Al <sub>6</sub> (Fe, Mn)	Al <sub>15</sub> (Fe, Mn) <sub>3</sub> Si <sub>2</sub>					
Cr	Si<Mg	Si>2 Mg					
	Al <sub>7</sub> (Cr, Fe)	Al <sub>15</sub> (Cr, Fe) <sub>4</sub> Si <sub>4</sub>					
Cu	Fe<Cu	Fe>Cu, Mg<2%					
	Al <sub>6</sub> CuMg <sub>4</sub>	Al <sub>7</sub> Cu <sub>2</sub> Fe					
Zn	Zn<2 %	Zn>2%					
	in solid soln.	Al <sub>2</sub> Mg <sub>3</sub> Zn					



Table 2.2 Morphologies of common intermetallic phases [15, 16]

Phases	Morphology
$\text{Al}_3\text{Fe}$	Needle or short rods
$\text{Al}_6(\text{Fe},\text{Mn})$	Square particles/plates (non-equilibrium)
$\text{Mg}_2\text{Si}$	Black Chinese script
$\text{Al}_8\text{Fe}_2\text{Si}$	Chinese script
$\text{Al}_{15}(\text{Fe},\text{Mn})_3\text{Si}_2$	Chinese script
Complex eutectic	Fine rounded dispersed particles containing $\text{Al}_8\text{Mg}_5$

### 2.1.1.3 Properties

The mechanical properties of Al-Mg series alloys change with composition and deformation state. For work hardening aluminium-based alloys, HXX is used to designate the condition [17]. The first X indicates the treatments used to attain the alloy's properties: 1 is cold-worked only; 2 is cold-worked then partially annealed; 3 is cold-worked then stabilised. The second X indicates the hardening/strengthening state: 0 and 8 are annealed and fully hard conditions, respectively; 2, 4 and 6 are one quarter, half and three quarters of hard condition, respectively. Sometimes, there is another number after the HXX to represent a special state or requirement for the products.

Al-Mg alloys are very widely-used commercial alloys, so the properties of certain temper need to be controlled by industrial standards, Table 2.3 shows some selected Al-Mg alloy properties.

Table 2.3 Typical properties and applications of selected non-heat-treatable wrought Al-Mg alloys [17, 18]

Alloy Designation	Temper	0.2% proof stress (MPa)	Tensile strength (MPa)	Elongation (% in 50 mm)	Typical applications
5005	0	40	125	30	General sheet material, high-strength foil, electrical conductor wire
	H38	185	200	4	
5050	0	55	145	24	Sheet and tube, rip tops for cans
	H38	200	220	6	
5052	0	90	195	25	Sheet, plate, tubes, marine fittings
	H38	255	270	7	
5454	0	120	250	22	Special-purpose sheet, plate, extrusions, pressure vessels, marine applications such as hulls and superstructures, dump-truck bodies, cryogenic structures
	H34	240	305	10	
5056	0	150	290	35	
	H38	345	425	15	
5083	0	145	290	17	
	H34	280	360	8	

## 2.1.2 Strengthening mechanisms in Al-Mg alloys

### 2.1.2.1 Work hardening

Work hardening has hundreds of year history as a method to improve a metal's strength properties. Until the concept of dislocations was introduced into material's study, the reason that cold, plastic deformation could improve the mechanical properties was

poorly explained. During this deformation, there is only about 1% of the work stored in the deformed materials with the rest released as heat [19]. The stored energy exists as increased dislocation density. It is important to study the density and distribution of excess dislocations in order to understand the following annealing phenomena.

According to Ashby's model [20], there are two kinds of dislocation accounting for work hardening: statistically-stored and geometrically necessary dislocations. The statistically-stored dislocations aggregated by deformation and were organised in mosaic patterns in each grains, and geometrically necessary dislocations were produced to satisfy the need to compatible deformation at features such as polycrystalline grain boundaries and regions around hard, non-deformable particles.

For polycrystalline materials, work-hardening can be divided into three stages according to the strain-stress curve: stage II, stage III, and stage IV. Stage I is for the single crystal case. Rollett et al. [21] reviewed all of these stages. Stage II has linear stress-strain curve with a slope of around  $G/200$  (where  $G$  is the shear modulus), and the geometrically necessary dislocations accumulated in this stage. Stage III is called 'parabolic hardening', which means that the hardening rate decreases with increasing strain. During stage III, dynamic recovery occurs, which accounts for the decrease in hardening rate. In Rollett's review, Stage IV was mentioned, but not explained. Stage IV is usually observed after large strains with a constant but very low work-hardening rate, which is around  $G/2 \times 10^4$ . It is believed that during Stage IV, the dislocation storage mode changed. In Ryen's work [22], Stage IV was related to shear band

formation and decreased subgrain and cell size, and this results in a good prediction for the work hardening rate during Stage IV, which is rate-independent of hardening.

The flow stress is influenced by the temperature, particle distribution, dislocation density and microstructure (grain and subgrain size), and can be expressed as:

$$\sigma = \sigma_t + \sigma_p + \alpha_1 Gb\rho_i^{\frac{1}{2}} + \alpha_1 Gb \left[ \left( \frac{1}{\delta} \right) + \left( \frac{1}{D} \right) \right] \quad \text{Equation 2.2}$$

Where the  $\sigma_t$  is the temperature-dependent component,  $\sigma_p$  is the non-deformed particle contribution,  $\rho_i$  is the dislocation density, and  $\delta$  and  $D$  are the subgrain and grain size, respectively [23]. During cold, plastic deformation, all components would change, but that of the dislocation density is the major part. After deformation,  $\rho$  increases from  $\rho_1$  to  $\rho_2$ . So, the increased stress is also expressed as:

$$\Delta\sigma = \alpha_1 Gb\rho_2^{\frac{1}{2}} - \alpha_1 Gb\rho_1^{\frac{1}{2}} \quad \text{Equation 2.3}$$

Where  $\rho_1$  and  $\rho_2$  are the dislocation density before and after deformation respectively [19].

#### 2.1.2.1 Solid solution strengthening

Solid solution strengthening has thousands of years history. Pure metal is too soft to be used for their mechanical properties. The yield stress of pure aluminium ranges from 7-11 MPa; for annealed AA5083, the yield stress can reach 200 MPa. At alloying levels below the solubility limit, the alloying elements dissolve in the matrix in the form of either substitutional or interstitial types, which is determined by the diameter of the element atoms compared with that of the matrix.

The solid solution strengthening is caused by the interaction between the interstitial solute atoms and the mobile dislocation. The solute is not homogeneously distributed in the matrix. The solute is enriched around the dislocation and forms a Cottrell atmosphere [24], so that extra stress is needed for the dislocation to break away. It is the reason that there is a peak from elastic deformation to plastic deformation for almost of interstitial alloying elements. After breaking away from the atmosphere, the dislocation moves forward and interacts with the solute through elastic interactions, which has i. There were a lot of models to describe the interaction between solute atoms and a moving dislocation. The solute atom has been treated as a single point defect and as a group or cluster, in the model of Mott and Nabarro and the model of Labusch, respectively [25]. The critical stress to break away Cottrell atmosphere could be expressed simply in the form of concentration:

$$\sigma = A c^{\frac{5}{3}} (\ln c)^2 \quad \text{Equation 2.4}$$

$$\sigma = B c^{\frac{2}{3}} \quad \text{Equation 2.5}$$

where A and B are constants and c is the concentration of the solute. Equations 2.4 and 2.5 are the model of Mott and Nabarro and the model of Labusch, respectively. In general, the expression could be written as:

$$\sigma = A c^n \quad \text{Equation 2.6}$$

For fcc substitutional solid solutions, the exponent n ranges from 0.5 to 0.75 for binary alloys [25]. Ryen et al. [26] studied the solid solution of commercial aluminium-based

alloys. For Mg,  $n$  changed in the range from 0.87 to 1.14, the slope increased with plastic strain from 12.1 to 47.7. Mn has a greater effect in solid solution, the slope changed from 54.8 to 120.2, and the exponent was around 1. For commercial alloys, there are other alloying elements in solution, which could have a synergistic effect [26].

#### 2.1.2.2 Grain Boundary Strengthening

For polycrystalline metals, grain boundaries block mobile dislocations, until pile-up stresses activate dislocation sources in adjacent grains. The relationship between grain size and the yield strength is known as Hall-Petch equation [27]. The equation is as follow:

$$\sigma_y = \sigma_0 + \frac{k_y}{\sqrt{d}} \quad \text{Equation 2.7}$$

Where  $\sigma_0$  is the friction stress (overall resistance of lattice to dislocation movement) and  $k_y$  is a positive constant of yielding associated with the stress required to extend dislocation activity into adjacent unyielded grains [28]. The value change with solute level, precipitate distributions, dislocation density and temperature, and is a constant for certain material. Petch slope  $k_y$  represents the effect of grain boundary compared with other hardening methods, such as work hardening and solid solution hardening. In general, grain boundary hardening decreases with increasing solute levels and strain.

The friction stress increases with increased alloy content. In Hansen's study [29], for 99.999% aluminium,  $\sigma_0$  was 5.49 MPa, and that of 99.5% aluminium increased to 17.64 MPa. This is related to the solid solution strengthening, the more solute the harder

dislocation movement is made. The Petch slopes were 1.372 and 0.784 N/mm<sup>1/3</sup>, respectively.

Lloyd et al. studied the Hall-Petch of various Al-Mg alloys [30]. The relationship between Petch slopes and strain showed that beyond the yield point the slopes dropped to a constant which was independent of strain. The slopes at the yield points were decreased with increased Mg content, and increased with the content of Mn. Mg has much higher solid solubility than that of Mn, Mg plays important part in solid solution hardening, but Mn was added to control the grain size. AA5083 has similar composition with Al5Mg0.7Mn, so the slope of Al5Mg0.7Mn could be used for modelling of AA5083 (ky was about 0.28 N/mm<sup>1/3</sup>).

## 2.2 Annealing phenomena in Al-Mg Alloys

Most of time, deformed metals need to be annealed before they are used. There are many reasons for this kind of annealing, such as stabilising properties, for further machining and to obtain certain textures. Sometimes, deformed metals will be exposed to a high temperature environment, such as welding process, and annealing will also occur. The properties and microstructure will change during the annealing process. Although annealing phenomena were known in ancient time, detailed study coincided with the invention of X-ray diffraction and electron microscopy.

In general, annealing phenomena are divided into recovery, recrystallisation and grain growth. Recovery refers the properties of materials partially restoring to their original value before deformation, irradiation or quenching [19]. Here, recovery is limited in the

annealing of deformed materials. The stored energy provides the driving force for both recovery and recrystallisation. Recovery is a process of re-arrangement of excess dislocations into stable structures such as sub-grain boundary. Recrystallisation is a process relating to high angle grain boundaries (HAGBs) sweeping from new strain-free nuclei to the neighbor deformed grain. After recrystallisation, the properties of materials would be nearly restored to their original values. Both grain growth and recrystallisation involve the migration of HAGBs, compared with recrystallisation, grain growth has low migration rate [31].

### 2.2.1 Recovery

Recovery occurs prior to primary recrystallisation and includes annihilation and rearrangement of dislocations [32, 33]. Compared to recrystallisation, recovery has not received as much study. It happens inside of grains, and cannot be seen by normal techniques, such as optical OM and SEM. Most of the relevant studies are conducted by DSC, electrical resistivity and mechanical properties. Over the last three decades, TEM and EBSD have been used to characterise recovered microstructures [32].

In experimental work, recovery is quantitatively measured by mechanical property change, such as hardness or yield stress [32, 34]. The remaining recovery effect could be expressed as:

$$R = \frac{\sigma - \sigma_i}{\sigma_o - \sigma_i} \quad \text{Equation 2.8}$$

Where  $\sigma_i$  is the yield stress of annealed condition, and  $\sigma$  and  $\sigma_o$  are the yield stress of before and after recovery, respectively.



The modelling work based on microstructure has been reviewed by Nes [34], which consisted of two elements: the subgrain size  $\delta$  and dislocation density  $\rho$  within the subgrains. Models could be divided into two types according to the subgrain formation sequence, as shown in Fig. 2.3. Type 1 assumed that subgrain boundaries existed before recovery, and type 2 deemed that dislocations were distributed homogenously before recovery. For Al-Mg alloys, type 1 behaviour has been observed directly by modern techniques, such as TEM, EBSD and 3DXRD. Similar microstructures to those seen in Type 1 behaviour are shown in Fig. 2.3 [35], the dislocation rearrange to form the subgrain boundaries. For Al-1Mg rolled to 20 %, subgrains were separated by low angle grain boundaries (misorientation was below 5 °), the distribution of dislocation was not homogenous, and some subgrains were nearly dislocation-free. In fact, during Stage III of work-hardening, dynamic recovery occurs, which would favour the formation of a subgrain structure.

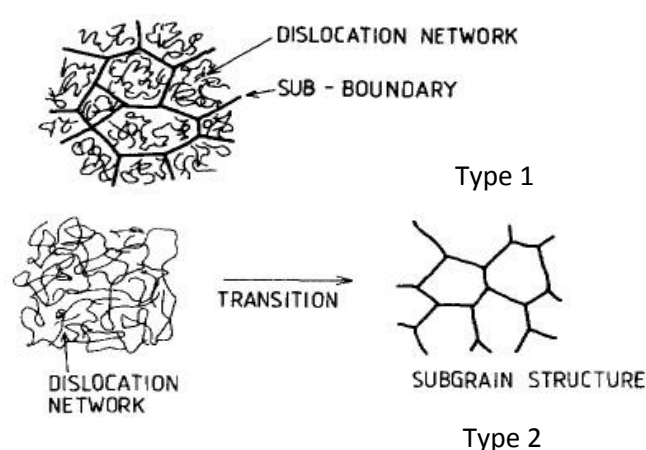


Fig 2.3 Subgrain microstructure of Models type 1 and type 2 [34]

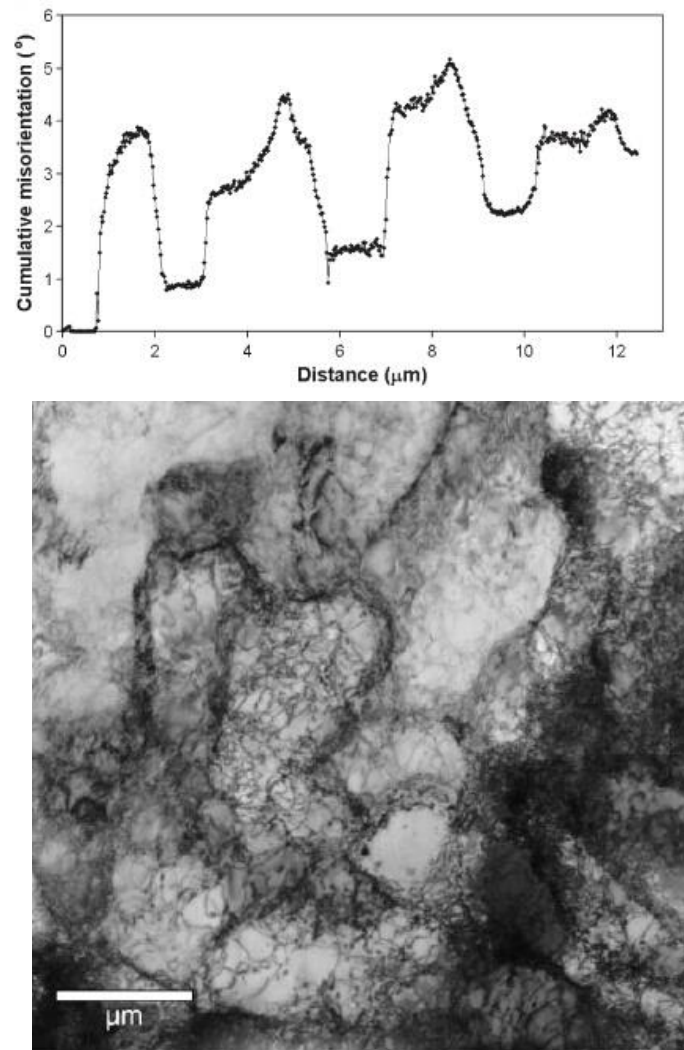


Fig 2.4 Al-1Mg (a) misorientation of LAGB. (b) TEM image [35]

There were several empirical relationships based on experimental work to describe the extent of recovery with time. One of the empirical relationships is expressed as[19]:

$$\sigma = c_2 - c_1 \ln(t) \quad \text{Equation 2.9}$$

Where  $c_2$  and  $c_1$  are constants.

Alcoa carried out a 17 year study on recovery in aluminium (2.4, 4 and 6 wt%) magnesium with different strain at room temperature[34]. The results showed that the

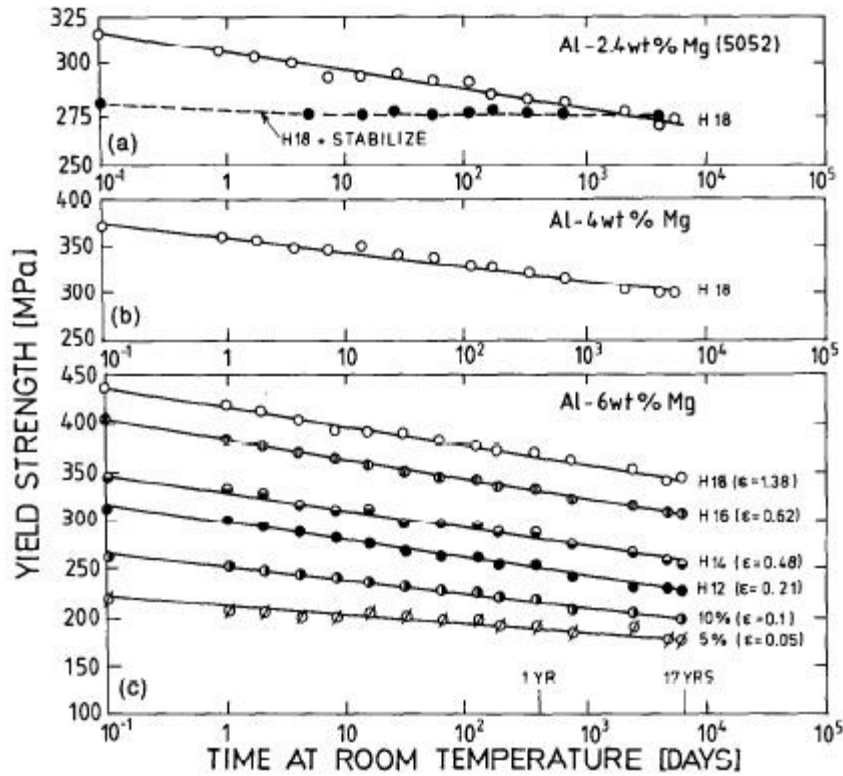


Fig 2.5 The classic Alcoa' experimental results [34]

mechanical property decrease following a logarithmic decay, which Equation 2.9 could fit well.

## 2.2.2 Recrystallisation

For deformed alloys, when the annealing temperature exceeds a certain value, recrystallisation starts. As for mechanical properties, they would go back to their original values; for microstructure, the deformed grains would be replaced with new strain-free grains [19]. Stored energy provides the driving force for both recovery and recrystallisation processes; compared with recovery, recrystallisation is related to high angle grain boundary (more than  $15^\circ$ ) migration [36].

### 2.2.2.1 Nucleation and grain growth during recrystallisation

Compared with recovery, the phenomenon of recrystallisation is easy to observe even by OM. It is obvious that for recrystallisation the microstructure evolution is new strain-free grains replacing the deformed grains, recrystallisation is treated as first order transformation, including nucleation and growth [37].

The stored energy in deformed metals ranges from 10 to 100 J/mol [19], and the driving force for normal solid-state transformation is  $\sim 1$  kJ/mol. For normal solid-state transformation, the thermal fluctuation model for phase transformation was well built, which could predict the kinetic of nucleation rate [38]. However, this model could not be used for recrystallisation. There is a critical size for an embryo to become a stable nucleus rather than disappear, and the critical size is expressed as:

$$R > \frac{2\gamma}{\Delta E} \quad \text{Equation 2.10}$$

Where the  $\gamma$  is the interfacial energy, and  $\Delta E$  is the driving force (i.e. stored energy for recrystallisation).

The  $\gamma$  is about  $0.5 \text{ J/m}^2$  for deformed metal. According to Equation 2.10, the critical size would be around  $0.1 \text{ }\mu\text{m}$ . It was impossible to produce a region by thermal fluctuations, and the rate of nucleation would be negligible [37, 39]. Until now, no experimental work can confirm the classical thermal fluctuation theory for recrystallisation.

In fact, recrystallisation is different from other solid-state transformations. Recrystallisation is a process that removes defects following recovery, the crystal structure does not need to change during this process, and there are some subgrains,

which are relatively dislocation-free regions (Fig. 2.4) that could act as potential nucleation sites. For deformed metals, only special sites are preferential for nucleation and the growth of nuclei [19].

Generally speaking, nucleation sites relate to heterogeneous microstructures, such as shear bands and regions around large second phase particles [19, 40]. Humphreys studied the nucleation of recrystallisation for deformed aluminium alloys with second phase particles [41]. It is well known that dislocations would accumulate at particles, which gives higher stored energy in these regions (because of high density of dislocation). In Humphreys' work, high voltage TEM was used to observe the microstructure, and the results showed that the subgrains away from particles were of average diameter 1.5  $\mu\text{m}$ , and the subgrains at particles were of average diameter 0.15  $\mu\text{m}$ . Although the size of subgrains at particles was smaller, according to the thermal fluctuation estimation, the size was above the critical size for the stable growth by subgrain boundary bulging into adjacent subgrains with higher stored energies. So the subgrains at particles could still act as nucleation sites.

The mechanism of PSN could be explained by a continuum model [19, 36, 41]. Dislocations accumulated around non-deformed particles during dislocation cause subgrains to rotate. Around the particle, there were subgrains with continuum misorientation, shown in Fig. 2.6. The small subgrains with higher dislocation densities would develop with higher polygonization rates. The process of polygonization would

consume the heavily deformed areas around particles and produce a favourably-sized nucleus for the further recrystallisation.

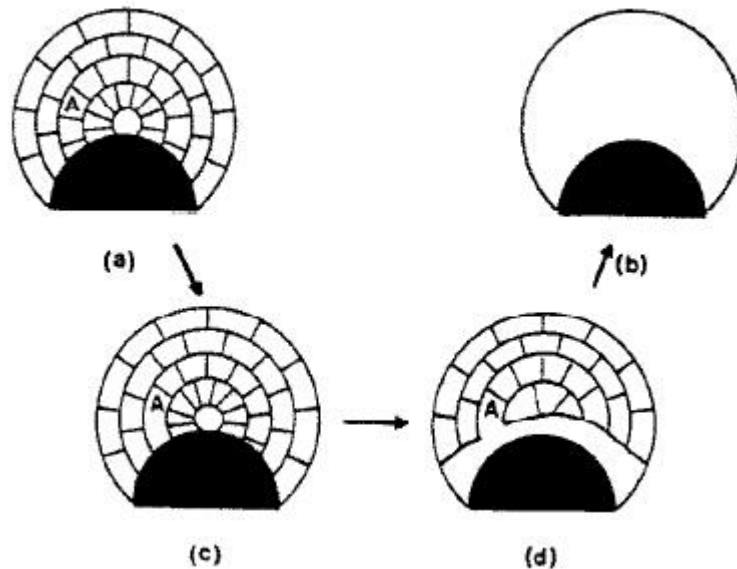


Fig. 2.6 Schematic of PSN [41]

The critical size of particle for the PSN was estimated by Humphreys [41], which has been generally accepted [42, 43]. The size was calculated combining the heavily deformed region at particles. The heavily deformed region was estimated to be  $\frac{1}{2}d$  (the diameter of the particle) by observation of HVEM, and the final size of nuclei produced at particle was around  $\frac{1}{2}d$ . The critical size or nucleation growing is above  $0.5 \mu\text{m}$ . So, the critical particle size for PSN was roughly  $1 \mu\text{m}$ .

Compared with subgrain size at second phase particle, the subgrains in matrix has size advantage. The size of matrix subgrain for aluminium-based alloys is usually of the order of  $1 \mu\text{m}$  [31, 40], and it is above the critical size for further growth. Experimental results always showed that nucleation originated from smaller nuclei around particles

and grain boundaries rather than in the bulk of the grains. This is caused by the boundary mobility difference due to different misorientations between subgrains. Direct boundary mobility studies are few for Al-Mg alloys, there were some results of Al-Si and pure aluminium showing a large difference in mobility caused by the misorientation[19]. Huang and Humphreys studied the mobility of LAGBs (ranging from 2.6 °to 5.6 °) in single crystals of Al-0.05%Si [44]. For deformed single crystals, most of subgrain grains grew continuously, but some subgrain with higher misorientation could grow discontinuously. It was found that the boundary mobility increased 50 times with a 3 °misorientation increase from 2.6 °to 5.6 °.

After nucleation, the new nuclei would grow into the surrounding, more-deformed subgrains. The growth rate is determined by two factors, one is the mobility of boundary between nucleus and surrounding subgrains and other is the driving force causing by the difference of stored energy. The growth rate could be expressed as [31, 36, 45]:

$$v=M* \Delta E \quad \text{Equation 2.11}$$

Where M is the grain boundary mobility, and  $\Delta E$  is the driving force.

#### 2.2.2.2 Texture evolution in recrystallisation

Texture is a very important method to characterize the orientation for metals, which is the relationship between material grain crystallography with the external coordinates of the sample. Texture could not only relate the orientation of materials with their properties but also help to explain lots of phenomena involving orientation change, such as solidification, phase transformation and recrystallisation [46]. Most techniques

involving diffraction can be used to obtain the texture information, such as XRD, TEM, and EBSD. According to the test resolution and area, the texture divides into micro-texture and macro-texture. Micro-texture is about the local crystallography relationships, such as between neighbouring grains, and the macro-texture is whole crystallography of the tested bulk with the sample coordinate. The micro-texture is usually represented by misorientation (angle and axis of rotation pair), and the macro-texture could be described by pole figure, inverse pole figure and orientation distribution function. About two decades ago, TEM was used to identify the micro-texture, and XRD was used to characterise the macro-texture. With development of EBSD techniques, both types of texture and related texture information can be measured by EBSD and related to microstructure [47-49]. Currently, a new technique—3DXRD is used to monitor the microstructure and texture change of aluminium alloys during recrystallisation [50-53]. The resolution of 3DXRD is about 0.6  $\mu\text{m}$ , it could not be an ideal technique to follow the formation of nuclei, but it is enough to study the growth of nuclei, and give orientation change information during recrystallisation.

Recrystallisation texture is usually compared with deformed texture, and researchers often need to identify the relationship between both textures. For f.c.c metals, during rolling processes, several orientations could be produced, shown in Table 2.4. Pole figures and inverse pole figures readily identify certain textures, but they are two-dimensional figures which makes it difficult to correlate all texture components. Full



orientation information could be described using the Orientation Distribution Function in Euler angle space. Orientations of rolled fcc metals followed two fibres known as  $\alpha$  and  $\beta$  (Fig. 2.7) [54]. At low degrees of deformation, orientations develop continuously along  $\alpha$  and  $\beta$  fibres; with increasing deformation, the homogeneous distribution of orientations is lost, and strong peak of deformed textures are formed.

Table 2.4 Texture components observed in rolled fcc metals [19]

Texture name and symbol	{hkl}	<uvw>	$\phi_1$	$\Phi$	$\phi_2$
Goss, G	011	100	0	45	90
Brass, B	011	211	0	45	90
S	123	634	59	37	63
Copper, C	112	111	90	35	45
Cube	001	100	0	0	0

The texture change during recrystallisation can be investigated by in-situ methods, such as 3DXRD and in-situ EBSD. Pure single aluminium crystal of S-orientation with a strain of 1.5 have been studied by 3DXRD [53]. The results showed that there was a new subgrain forming with different orientation compared with matrix orientation, which was about 10  $\mu\text{m}$ . There was no correlation between both orientations before and after annealing. Limited by the resolution of 3DXRD, it was hard to identify whether there was a small-sized subgrain with different orientation existing in the matrix before annealing or not. The 3DXRD study still confirmed that subgrains with different orientation (higher misorientation) had higher growth rates.

For single phase polycrystalline aluminium alloys, cube textures were usually found to

increase after recrystallisation [55-57]. The texture of deformed metals do not show the cube texture as a significant component, but there are some models to explain the cube

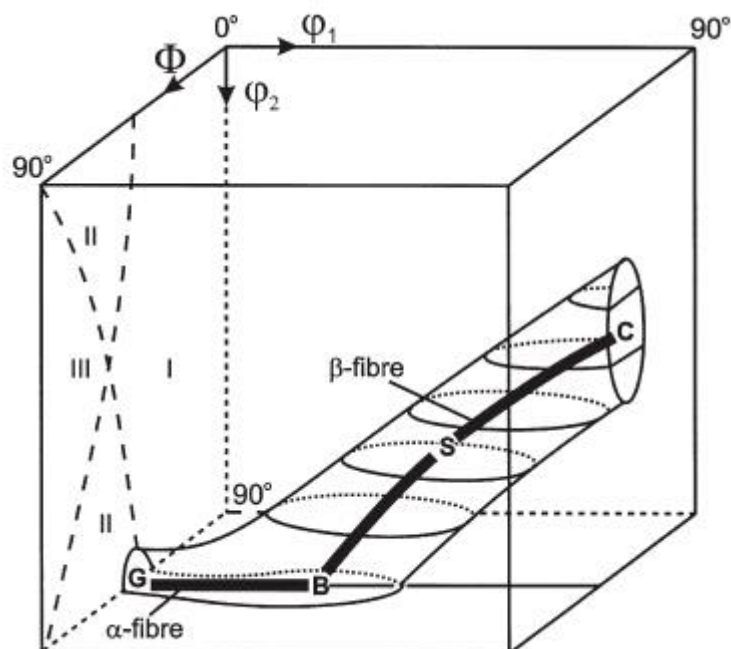


Fig 2.7 Schematic presentation of the fcc rolling texture in the first subspace of Euler angle space [54]

texture increase on recrystallisation. One is based on Dillamore and Katoh's work [58]. Cube orientation could develop in transition bands, a cube nucleus has a large misorientation with matrix, so the cube nucleus would have higher growth rate than that of other oriented subgrains. Another model deemed the cube-oriented elements were stable during hot rolling, and the cube-oriented elements would grow through SIBM, and this model is called cube-band model [59]. Al-1.2Mg-0.9Mn was studied in Vatne et al.'s work [59]; it showed that the pre-existing cube grains were metastable during deformation, and were deformed bands, and these bands were preferential nucleation sites for recrystallisation. Both of these models could explain the formation of cube

orientation reasonably, if combining the possible grain size change before and after recrystallisation, it could be concluded that Dillamore and Katoh's model is more reasonable. For cube-band model, only one nucleus could form in the band, this nucleus would consume surrounding subgrains with different orientation, and one possible result is that some grains with cube orientation would be much larger compared with matrix grains. There are few reports about such abnormal cube-orientation grain growth during recrystallisation.

For two phase polycrystalline aluminium-based alloys, the second phase particle have different effects on the recrystallisation depending on the size of the particles. If the particles are small, they would have the effect of Zener pinning, which could delay recrystallisation. In the small particle case, the cube-oriented nucleus is preferred, so the cube orientation is still strong after recrystallisation [60]. When the particle size exceeds the critical size for PSN, the texture will become more random. This always occurs in commercial Al-Mg alloys. There were large size Fe or Mn appearing in Al-Mg alloys, and PSN could act as the dominant mechanism for nucleation. As shown in Fig. 2.6, the orientation was determined by the nucleation at the particle, which could be deemed as random distribution.

#### 2.2.2.3 Factors influencing the rate of recrystallisation

Many factors affect the rate of recrystallisation: deformed strain; original grain size; solute content; annealing temperature; heating rate; and particle distribution[32, 33, 61] . The amount of deformation strain affects the recrystallisation rate through changes in

the stored energy and the number of nuclei, which is a function of strain [62] . Li et al. [15] studied the effect of prestrain on the properties of AA5182-O (shown in Table 2.5), and found the annealing time decreased with an increase of prestrain at certain annealing temperature. In Li 's [15] study, the final strength did not show an obvious trend with increase of prestrain, it indicated that, for lightly deformed alloys, the recrystallisation rate was mainly controlled by stored energy rather than the increased number density of sites for nucleation. However, for heavily deformed alloys, the effect of deformation on recrystallisation is a direct result of an increase in the density of nucleation sites,  $N_v$  in the deformed microstructure. In Go et al.'s study [63], the grain size of fully annealed AA5754 alloy varied inversely with deformation, ranging from 32 to 15  $\mu\text{m}$  as the prestrain was increased from 0.58 to 1.83. So, it could be concluded that the effect of number density of nucleation sites on recrystallisation rate increases with increase of deformation. The effect of grain size on the recrystallisation rate has been attributed to two main reasons: 1, the decrease of grain size results in increased stored energy; 2, a fine-grained condition provides a greater number density of active nucleation sites [63]. The explanation of the effect of grain size on recrystallisation is similar to that of deformation. Solute content could influence the recrystallisation by pinning both low and high angle grain boundaries (retarding recrystallisation) [19] and decreasing the stacking-fault energy (accelerating recrystallisation). In Al-Mg alloys, the effect of decreasing the stacking-fault energy is greater than that of pinning boundaries, and Zhao et al. [5] found direct chill (DC) AA5052 recrystallised faster

than continuous cast (CC) band of AA5052, due to the higher Mg content in solid solution for DC processing. Recrystallisation is a thermally activated process with the effect of annealing temperature being determined via activation energies. In Go et al.'s study [64], the annealing time decreased from 28 hours to 10 minutes as the annealing temperature increased.

Table 2.5 The annealing time for full recrystallisation under different prestrains and at different temperature [64]

Prestrain Temperature	0.05	0.10	0.15	0.20
300 °C	>3600 s	3600 s	>3600 s	3600 s
350 °C	>3600 s	1500 s	500 s	300 s
400 °C	600 s	200 s	30 s	20 s

#### 2.2.2.4 Modelling of Recrystallisation

Recrystallisation is usually modelling from the basis of the classic Johnson–Mehl–Avrami–Kolmogorov (JMAK) equation. The JMAK equation is described by the following simple relation between the volume fraction of recrystallised material and the annealing time t:

$$X_v = 1 - \exp(-Bt^n) \quad \text{Equation 2.12}$$

Where n is the Avrami exponent and B is a constant.

Assuming a random distribution of “nucleation” sites in two dimensions, site-saturation nucleation kinetics, and an isotropic and constant growth rate, the JMAK theory

predicts an Avrami exponent  $n$  of 2. However, because nucleation of recrystallisation is a highly heterogeneous process, which typically takes place at deformation heterogeneities such as shear bands, transition bands, and in deformation zones around large particles [65], the Avrami exponent usually is less than 2 for commercial Al-based alloys. Some published data of Al-Mg alloys about Avrami exponent shows in Table 2.6. Marthinsen et al. [65] found the Avrami exponent increased with increase of strain: the values ranged from 1.4 to 1.9, as the strain changed from 2.8 to 6.2, and they attributed the variation of Avrami exponent to the heavy deformation resulting in more random distribution of nucleation sites.

Table 2.6 Avrami exponents from literature [64-66]

Alloy	n
AA5083	2
AA5754	1.2
Al1Mg (prestrain=0.28)	1.67
Al1Mg (prestrain=0.7)	2

Apart from fraction of material transformed, the change in microstructure during recrystallisation needs to be described by more parameters. Vandermeer and Rath made a significant improvement of the JMAK approach [67], which was called the microstructural path methodology (MPM). MPM method increases two more parameters (extended interfacial area and the largest unimpinged grain intercept), which makes more realistic and more complex geometric recrystallisation models possible

[32]. The relationships of these parameters with annealing time could be expressed by the following equations:

$$X_{\text{vex}} = Bt^n \quad \text{Equation 2.13.1}$$

$$S_{\text{vex}} = Kt^m \quad \text{Equation 2.13.2}$$

$$D_L = St^s \quad \text{Equation 2.13.3}$$

The nucleation rate and growth rate are used  $\delta = 3m - 2n$  and  $r = n - m$ . When  $\delta = 1$ , this corresponds to a constant nucleation rate,  $\delta = 0$  corresponds to site saturated nucleation, and  $r = 1$  corresponds to a constant growth rate. Rossi et al. [68] used this method and found that for an Al-1% wt Mg alloy with two different strain 0.28 and 0.6, the  $\delta$  values were 0.6 and 0.08 respectively, which showed that the nucleation of heavy deformed alloy was close to that for site saturation.

Although the MPM method could give more detailed information about the recrystallisation process, the parameters of MPM can only be measured by optical microscopy and it is much more complicated to get accurate results in practice than for the JMAK equation. For modelling of recrystallisation, the Avrami exponent is Much more important than the other two parameters in MPM, so in this study the JMAK method will be used.

The above two analytical methods are useful in giving a broad description of a process, but both of the methods are established under isothermal annealing conditions. However, in the HAZ, the metal experiences an anisothermal cycle, so it is necessary to build a non-isothermal model to predict the strength development. Several reports

focused on deriving the non-isothermal crystallisation behaviour from the isothermal JMAK kinetic models [64, 69, 70]. The most important principle is to split the thermal cycle into finite time steps, then, during each step ( $\Delta t$ ), the thermal process is regarded as isothermal. Peel et al. [69] used a modified JMAK equation:

$$X_v = 1 - \exp\left(-0.693 \frac{t}{t_{0.5}}^n\right) \quad \text{Equation 2.14}$$

and introduced “effect time” at isothermal temperature which was to replace the non-isothermal annealing time. The effect time  $t_{\text{eff}} = \sum_0^n t_i \exp\left(\frac{-Q}{Rt_i}\right)$ , then the recrystallisation fraction could be expressed by:

$$X_v = 1 - \exp\left(-0.693 \left(\frac{t_{\text{eff}}}{A}\right)^n\right) \quad \text{Equation 2.15}$$

The model also does not consider any change in activation energy with temperature nor the effect of heating rate on recrystallisation which may cause some errors. In Peter’s JMAK model [70], each step of thermal cycle is regarded as an isothermal heat step, which change linearly as a function of  $\Delta t$ , but changes in the activation energy were still not considered.

Both the JMAK and MPM modelling methods could be classified as mathematical methods, and the input variables are based on the experimental results, directly. The information of nucleation and growth rates are included in the pre-coefficients (the constants for JMAK and MPM). The accuracy of this type model is mostly determined by the experimental data.



Compared with the mathematical models, with the computer capacity improved a lot, the simulation of the microstructure are developing very fast [71]. For a simulation, it must base on correct physical understanding of recrystallisation, then accurate nucleation sites and their own grain growth rate can be input into the simulation. Although the phenomenon of recrystallisation has been studied for a hundred years, most of results are good for qualitative analysis rather than quantitatively analysis. For example, it is believed that the PSN would be dominant for aluminium alloys with second phase large particles, but whether there is other nucleation mechanism and how much effect of other kinds nucleation occurs is hard to say during real recrystallisation. However, the difference between the simulation and experimental results could make researchers study the phenomena more detailed.

### 2.2.3 Grain growth

Grain growth after recrystallisation is different from growth during recrystallisation (i.e. rate of consumption of deformed grains by strain-free grains). The driving force of normal grain growth is the internal energy decrease caused by the reduction of boundary area. There are two types of grain growth according to the microstructure change, one is normal grain growth and another is abnormal grain growth.

The normal grain growth is a homogenous competing process, and the general rule is that larger grains grow and smaller ones decrease until vanish.

Compared with recovery and recrystallisation, the phenomenon of grain growth is easy to be observed by optical microscopy. The principal points derived from observations

before the 1950s are still valid up to now. Six principal points are summarised as following [72]:

1. Grains grow by the migration of boundaries, rather than coalescence of neighboring grains;
2. The rate of grain boundary migration is not constant, and may change with temperature and curvature;
3. A given grain might consume the neighbouring grain on one side and be consumed by other neighboring grains on another side;
4. The smaller the grain, the faster of the rate of consumption;
5. A grain boundary migrates towards its centre of curvature;
6. Stable grain boundary arrays tend to meet at angles of 120 °

The grain growth could be expressed as following[19, 31]:

$$R^n - R_0^n = c * t * e^{(-Qg/RT)} \quad \text{Equation 2.16}$$

A general form could be written as:

$$R^n - R_0^n = C * t \quad \text{Equation 2.17}$$

where  $R_0$  and  $R$  are the average grain diameter before and after grain growth, respectively;  $Qg$  is the activation energy for grain growth;  $c$ ,  $C$  and  $n$  are constants.

Under the assumptions [72] of constant grain boundary interfacial energy, the grain growth exponent  $n$  would be 2. In experimental work, the exponent was usually larger

than 2 [19]. The mobility of a grain boundary could be affected by several factors, such as solute content, second phase particles and temperature.

After recrystallisation, abnormal grain growth could occur rather than normal grain growth. During abnormal grain growth, only a few grains grow to extra-large size, compared with other matrix grains. Sometimes, the abnormal grain growth is called secondary recrystallisation. The reason is that the abnormal growth is similar with the primary recrystallisation that microstructure changes heterogeneously, including two stages: nucleation and growth of nucleus.

Most reports of abnormal grain growth indicate that incubation time and long annealing time are needed [31]; however, for the welding of aluminium sheet, the whole thermal cycle is short and could not provide enough time for abnormal grain growth. Reports about abnormal grain growth in welding of aluminium sheet have not been found and so it will not be considered in detail.

#### 2.2.4 Techniques to reveal annealed microstructures

Up to now, many techniques have been used to characterise the phenomena of annealing. All of the techniques could be divided into two types. One is direct methods, in which the microstructure change from these phenomena is observed; another is in-direct methods, in which the properties of materials are measured and related to annealing phenomena.

Direct methods include OM, TEM, XRD and EBSD. All of these methods have their advantages and disadvantages. OM is the earliest technique to characterise the microstructure. It is a very convenient method to investigate the recrystallisation and grain growth. For aluminium-based alloys, chemical etching to outline the grain boundary is problematic, although a two-step colour etching was named as universal method [73], the image of microstructure was too fuzzy to quantitatively be analysed. Anodising is usually used to reveal aluminium-based alloy microstructures. The basic theory of anodising is that there would be different thickness oxide layers forming during anodising, the thickness is determined by the orientation of the grain, and, under polarised light OM, different colours correspond to different orientation grains. Before recrystallisation is complete, there are grains which are in the deformed state; it is not possible to form the same thickness of oxide layer, so the final image of anodising cannot reveal the recrystallising microstructure clearly (shown in Fig 2.8).

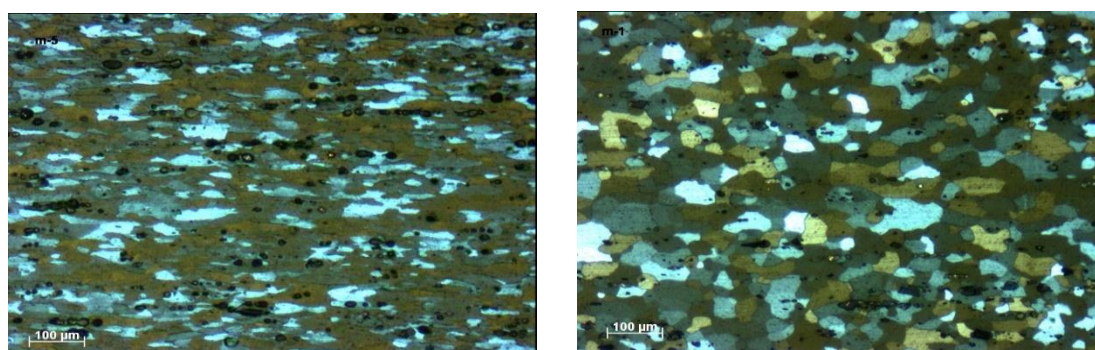


Fig 2.8 Anodising microstructure as received: a, AA5083 H22; b, full recrystallised AA5083 H22

TEM has very high resolution, and the high resolution TEM (HRTEM) could go to the atom scale. With the help of TEM, grain, subgrain and dislocation structures after

deformation have been studied intensively, and the mechanism of recovery and nucleation of recrystallisation are relatively clear up to now. There are two weak points of TEM to study microstructure. Firstly, the region suitable for TEM is very limited, it takes long time to get large data to analyse quantitatively; second, although TEM is suitable for local point orientation analyse, it is nearly impossible to determine the texture of whole sample, which represents the relationship between the grain's crystal information with sample coordinates.

Recently, EBSD has developed into a practical technique for researchers who study crystalline materials. The angular resolution and spatial resolution are  $0.2^\circ$  and 20 nm, respectively. These resolutions could make EBSD obtain the same accurate microstructure and texture results to TEM, but with larger areas investigated [48]. The acquisition speed has limited application of EBSD, until the use of low light TV cameras for pattern acquisition in 1992, and the acquisition speed had reached 5Hz in 1999 [48]. According to a recent report from Oxford-instruments [74], the maximum speed has reached 870 Hz, and it could get a reasonably clear image in about 10 minutes. The major problem about EBSD is the method to prepare the sample. To get a good image, the surface need to be free of strain caused by polishing, so most of the time chemical or electrical polishing needs to be used to get rid of the deformed layer after normal mechanical polishing. Sometimes, for very severely deformed materials, the lattice itself is distorted, so that it is hard to get good result without calibration of the phase parameter in the database of EBSD.

Indirect methods measure the properties which change with the annealing phenomena and it usually include measuring the thermal release or mechanical properties, and sometime the electrical resistivity is used to qualitatively analyse the annealing phenomena. Recovery, recrystallisation and grain growth are all thermal release processes, so they could be represented by thermal release. Compared with phase transformation, the total heat release of annealing phenomena is quite small, but it still can be investigated by high resolution DSC. Normally, there are two exothermic peaks to show the annealing phenomena of deformed metal, the lower temperature one corresponds to recovery and the higher temperature one is for recrystallisation [75]. In practice, changes in mechanical properties (strength and hardness) are widely applied to measure the kinetics of annealing phenomena. The reason is that the testing equipments is usually readily available and the results are more objective and repeatable.

### 2.3 Thermal cycle in the heat affected zone (HAZ) of the weldment

The microstructure of a weldment would change during the welding thermal cycle. The microstructure changes are complicated, and may possibly include recovery, recrystallisation, grain growth, precipitation, second phase particle dissolution, and phase transformation of the matrix (not for aluminium-based alloys). All of the phenomena mentioned above could occur in the Heat Affected Zone (HAZ), regardless whether fusion welding or non-fusion welding is being used. As for fusion welding, the centre of the weldment would melt, and solidification occurs when the heat source moves forwards.

The thermal cycle of HAZ determines the final microstructure. It is impossible to use thermocouples to monitor all of the thermal cycles in the HAZ. Modelling work has been carried out to obtain accurate temperature distributions through a weldment. The modelling work can be divided into two types: analytical models and numerical models. Both types of model are based on the thermal conduction equation. The governing equation is written as:

$$\frac{\partial T}{\partial t} = a \frac{\partial^2 T}{\partial r^2} \quad \text{Equation 2.18}$$

Where  $a$  is material thermal diffusivity,  $T$  is the temperature,  $t$  is the time and  $r$  is the heat flow direction.

Rosenthal [76] studied the thermal distribution of fusion welding in the 1940s and put forward the concept of ‘pseudo-steady state’ firstly, which is the base of the other analytical models. The pseudo-steady state is that no change temperature observed due to the moving heat source. Under the concept, a steady temperature distribution around the heat source would move in the direction of the welding.

There were some assumptions made for the original analysis [76], as follows:

1. The heat source moved at a constant speed with a certain heat input;
2. The heat source was treated as a point;
3. The latent heat of fusion in the fusion zone and the possible heat of phase transformation in HAZ were ignored;

4. The thermal properties of the parent metals were constant;
5. There was no heat loss from the surface of the plate;
6. There was no convection in the fusion zone.

For a three-dimensional plate (shown in Fig. 2.9), if a heat source moves along the x-axis at a speed of  $v$ , a variable  $\xi$  could be defined as:  $x' = x - vt$ . Through the  $x'$  the pseudo-steady state could be defined, in which the temperature will not change with time around the heat source. The thermal governing equation is written as:

$$\frac{\partial^2 T}{\partial x'^2} + \frac{\partial^2 T}{\partial y^2} + \frac{\partial^2 T}{\partial z^2} = -\frac{v}{a} \frac{\partial T}{\partial x'} \quad \text{Equation 2.19}$$

The pseudo-steady state heat conduction is:

$$\frac{\partial^2 T'}{\partial x'^2} + \frac{\partial^2 T'}{\partial y^2} + \frac{\partial^2 T'}{\partial z^2} - \left(\frac{v^2}{2a}\right) T' = -e^{x'v/2a} \frac{Q}{\lambda} \quad \text{Equation 2.20}$$

where  $T' = (T - T_0) - e^{x'v/2a}$ ,  $T_0$  is the reference temperature, normally taken as the ambient temperature;  $Q(x,y,z)$  is the heat source [76].

### 2.3.1 Heat source

#### 2.3.1.a Rosenthal heat sources

For the fusion welding of thick and thin plates, the heat source  $s$  were taken as point and line heat sources, respectively. Rosenthal's solutions for both plates were to deduce the correct Green's function. Equation 2.19 and Equation 2.20 are the solutions for the thick and thin plates, respectively:

$$T - T_0 = \frac{q_0}{2\pi\lambda} \left(\frac{1}{R}\right) \exp\left(-\frac{v}{2a}(R + x')\right) \quad \text{Equation 2.21}$$



$$T - T_0 = \frac{q_0}{2\pi\lambda} \exp\left(-\frac{vx'}{2a}\right) K_0\left(\frac{vr}{2a}\right) \quad \text{Equation 2.22}$$

Where the R and r is the distance of the interested point -Q to the heat source-P (shown in Fig.2.9) expressed for thick and thin plate solutions, respectively,  $T_0$  is the room temperature,  $q_0$  is the net energy input, and  $\lambda$  is the thermal conductivity.

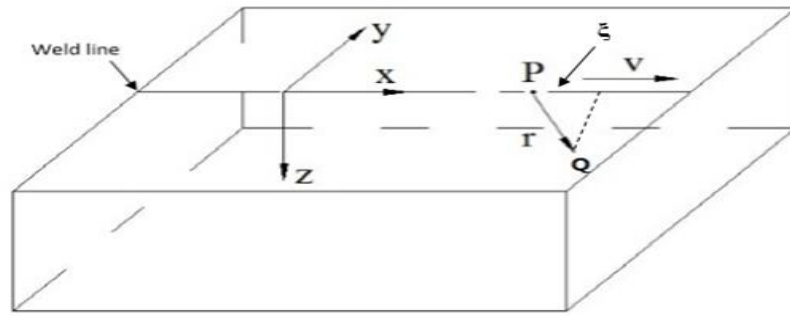


Fig. 2.9 Geometry for Rosenthal analysis

Christensen used a set of dimensionless symbols to simplify the original Rosenthal equations[77]. There are three parts of to Christensen's simplification:

1. dimensionless temperature

$$\theta = (T - T_0)/(T_m - T_0) \quad \text{Equation 2.23}$$

where  $T_m$  is another reference temperature, normally taken as the melting point;

2. dimensionless operating parameter

$$n = \frac{Qv}{4\pi a^2 \rho c ((T_m - T_0))} \quad \text{Equation 2.24}$$

3. dimensionless coordinates and radius vector

$$\xi = vx'/2a \quad \text{Equation 2.24.a}$$

$$\psi = vy/2a \quad \text{Equation 2.24.b}$$

$$\phi = vz/2a \quad \text{Equation 2.24.c}$$

$$\sigma_r = vR/2a \quad \text{Equation 2.24.d}$$

The dimensionless equations for Rosenthal's thick and thin plates were:

$$\theta = \frac{ne^{-(\sigma_r - \xi)}}{\sigma_r} \quad \text{Equation 2.25}$$

$$\theta = \frac{ne^{-\xi K_0(\sigma_r)}}{\delta} \quad \text{Equation 2.26}$$

It should be noticed that  $\delta$  is the dimensionless thickness:  $\delta = vd/2a$ .

In practice, the application of Rosenthal's solution is limited. According to Rosenthal's thin plate solution, the heat source is treated as a line heat source, which the input heat homogenously distributed along the thickness. The heat source of the thick plate is a point source which moves on the surface of the weldment. The line heat source and point heat are dimensionless in physics, so the temperature at the heat source is infinitely high; this is not true for experimental work. So, for an accurate prediction of the thermal cycle, the point heat source must be replaced by other heat sources, such as the Gaussian heat distribution heat source and double-ellipsoidal heat source.

### 2.3.1.b Gaussian heat distribution

Eagar and Tsai used a 2-D Gaussian distribution to replace the point heat source [78].

Fig.2.10 shows the 2-D Gaussian distribution. The Gaussian equation can be expressed as:

$$q(r) = q_m * e^{-r^2/2\sigma^2} \quad \text{Equation 2.27}$$

$$q_m = q/2\pi\sigma^2 \quad \text{Equation 2.28}$$

Where  $q$  is the net input power,  $q_m$  is the maximum input heat density,  $\sigma$  is the standard deviation of the Gaussian function, and the value is  $r$ .

If the Gaussian heat source moves on the  $x$ - $y$  surface, then Equation 2.27 would be converted into:

$$q(x,y) = q_m * e^{-(x^2+y^2)/2\sigma^2} \quad \text{Equation 2.29}$$

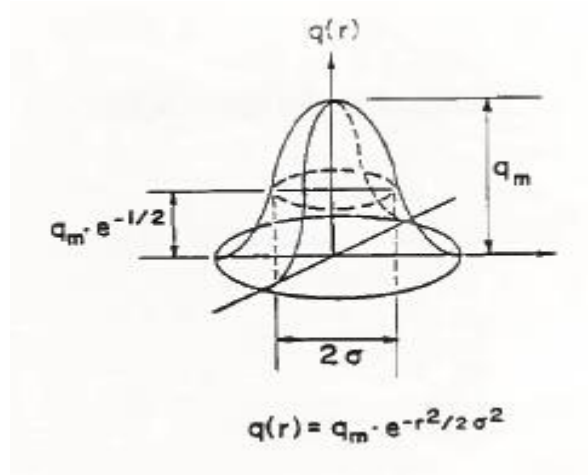


Fig.2.10 Gaussian distributed heat source [78]

Although the temperature distribution with Gaussian distribution have been solved, the expression is very complex even in the dimensionless form:

$$\theta = \frac{n}{\sqrt{2\pi}} \int_0^{v^2 t/2a} \frac{\tau^{-1/2}}{\tau+u^2} e^{-\frac{\xi^2+\psi^2+2\xi\tau+\tau^2}{2\tau+2u^2}} - \frac{\phi^2}{2\tau} \quad \text{Equation 2.30}$$

where  $\tau = v^2 t/2a$  and  $u = v\sigma/2a$ . Compared with the point heat source, the solution of the Gaussian heat distributed heat source could predict the weld geometry more

accurately. Eagar and Tsai [78] compared the predicted results with a series of experiments gas tungsten arc welds made on carbon steel, and the comparisons results are shown in Fig. 2.11. The results of the distributed heat source show good agreement between the prediction and experimental results, and the Rosenthal solution only give one possible trend with a relatively large error.

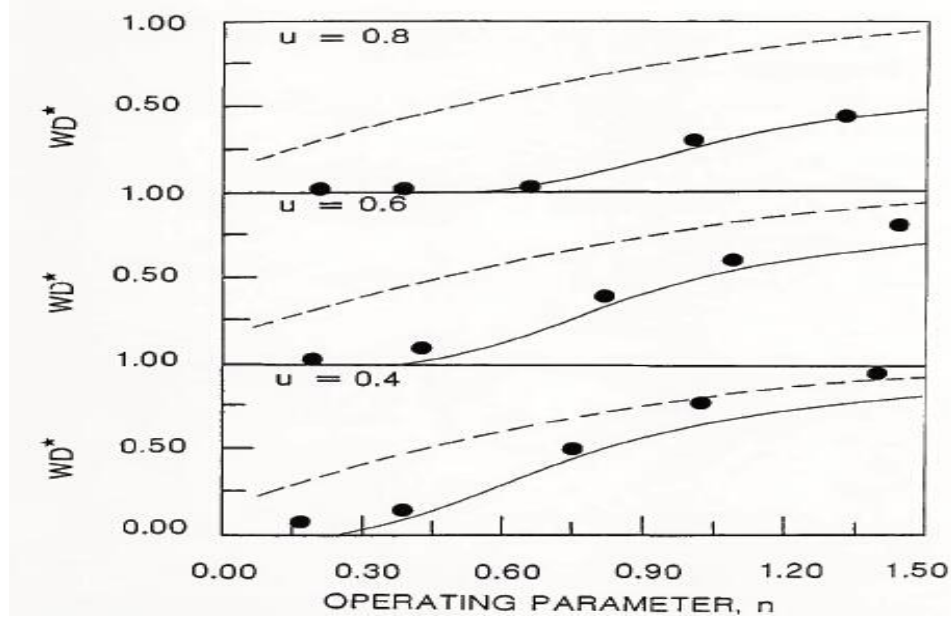


Fig. 2.11 Dimensionless weld depth of three values of heat distribution. The solid lines are the predictions of the distributed heat source, the dashed lines are the prediction of the Rosenthal solution, and the data points are the experimental results [78]

### 2.3.1.c Double-ellipsoidal heat source

The double-ellipsoidal heat source is a 3-D heat source model put forward by Goldak et al [79]. The heat source is shown in Fig. 2.12. If the heat source moves on the x-y plane in the direction of x, the heat distribution would be:

$$\text{Front part: } q(x, y, z) = \frac{6\sqrt{3}r_f Q}{(a_f + a_r)bc\pi\sqrt{\pi}} * e^{-(3x^2/a_f^2 + 3y^2/b^2 + 3z^2/c^2)} \quad \text{Equation 2.31}$$

$$\text{Rear part: } q(x, y, z) = \frac{6\sqrt{3}r_r Q}{(a_f + a_r)bc\pi\sqrt{\pi}} * e^{-(3x^2/a_r^2 + 3y^2/b^2 + 3z^2/c^2)} \quad \text{Equation 2.32}$$

where  $r_f = 2a_f/(a_f + a_r)$ ,  $r_r = 2a_r/(a_f + a_r)$ .

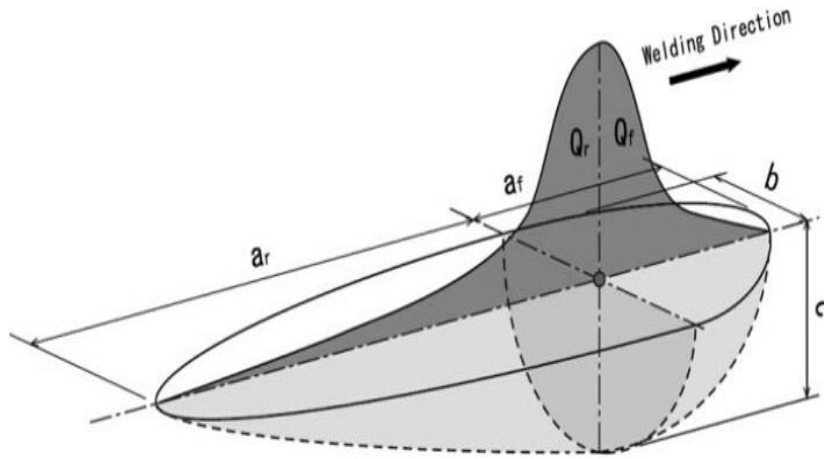


Fig. 2.12 Double ellipsoid heat source configuration [80]

Although there is some analytical solution for the double ellipsoid heat source [81], most of the applications have combined with a computer numerical calculation since Goldak [79]. Goldak compared the results calculated through the double ellipsoid heat source with the experimental results of Christensen [77]. The calculated results showed good agreement with the experimental results. For submerged arc welding on thick mild steel with 32.9 V, 1170 A at a welding speed of 5 mm/s, the experimental result showed that the cooling time (800 to 500 °C) took 37 seconds, and the calculated results showed that it would take 39 seconds, which was only a 4% difference.

After comparing the three different kinds of heat source, it is easy to find that they all have their own advantages and disadvantages. The Rosenthal's point and line heat sources could be calculated without the help of a computer, but it is still used for a

rough estimation. Rosenthal heat sources can give good prediction results for the regions of weldment where the temperature is 20% lower than the melting point [77, 79]. Although there is a Green's function for the Gaussian distributed heat source, it is harder to calculate in analysis method. Currently, Gaussian and double-ellipsoidal heat sources are widely used in the FEM models. Definitely, double-ellipsoidal heat source can give the most accurate prediction, extra parameters need to be determined, such as:  $a_f$ ,  $a_r$ ,  $c$ . In fact, the Gaussian heat source is an example of double-ellipsoidal heat source, when  $c=0$ ,  $a_f = a_r = 1/2b$ . For a shallow penetration weld, such as TIG and MIG weld, there is little difference between the prediction of Gaussian and double-ellipsoidal heat sources. However, for the deep penetration weld, such as electron beam and laser welds, the depth  $c$  of the heat source cannot be negligible, and this will increase the difficulty of the calculation.

### 2.3.2 Comparison of analytical and numerical methods

The analytical method is based on the solution of the thermal conduction function under the basic assumptions of Rosenthal's solution [76]. The first step is to obtain the correct Green's function. It is easy to obtain the Green's function when the heat sources were treated as point and line heat sources. Equation 2.21 and Equation 2.22 are the solutions for the point and line heat sources, respectively. There is a modified Bessel function in the line heat source solution which make the calculation more difficulty. When the heat source is replaced with a Gaussian distributed heat source, the Green's function is much harder to calculate without the help of a computer.

For the analysis method, after deducing the Green's functions, the weldment would be treated as a solid geometry and divided into lots of separate points in the Cartesian coordinate system. Then the temperatures of each point are calculated one by one.

For numerical models, the aim is also to solve the partial differential Equation 2.18. The weldment is meshed as a number of small elements, then the temperature of each node is solved from the welding line to the lower temperature parent matrix. It should be noted that, as the analytical method, the accuracy is still dependent on the input of heat source distribution.

## 2.4 Project aims

The project aims to study the annealing phenomena of Al-Mg alloys for the isothermal heat treatment and the non-isothermal process in a heat-affected zone (HAZ) and obtain the essential input parameter data for future microstructure modeling work in HAZ.

The microstructure will be characterised in as-received metal and HAZ. The mechanical property (hardness) will be tested for samples isothermal heat-treated and in the HAZ of weldment. In addition, the prediction of the thermal profiles in the HAZ will be carried out using Comsol software.

## Chapter 3 Experimental methods

### 3.1 Materials

Al-Mg alloy sheets of AA5083 H22 (1.6 mm in thickness) were used in this study. The “H22” refers to the condition whereby the strain-deformed material undergoes through higher-temperature recovery and the tensile strength of the material decreases to quarter way between the annealed and full strain-deformed conditions.

Samples of aluminium-based alloy sheets had been metal inert gas (MIG) welded as part of an earlier project [82] using an AA5356 filler wire and the process parameters summarised in Table 3.1. The welding direction was perpendicular to the rolling direction of the sheets. The weldment of AA5083 (H22)-W8 was used to study the property (hardness) with the microstructure evolution. In an earlier project [82], thermal cycles measurement in the HAZ by thermocouple have been carried out in the weldment of AA5251 (H34) sheets, and these thermal data and fusion zone size of the weldment were used to build a thermal profile model.



Table 3.1 Welding parameters in the welding of AA5083 H22 and AA5251 H34 [82]

	Wire feed rate	Welding speed	Arc time	Average voltage	Average current	Net power	Heat input	Filler diameter
	m/min	m/min	s	V	A	W	kJ/m m	mm
AA5083 -W8	6.5	1	26	14.1	109	1229. 5	0.09	1.2
AA5251 -W8	6.0	0.9	30	19.0	111	1669. 5	0.14	1.2

### 3.2 Sample preparation

Samples (10 x 5 mm, rolling direction, RD, and transverse direction, TD, respectively) were cut from the as-received sheet, Fig. 3.1, for heat treatment and hardness, OM and EBSD testing. Specimens (3 x 3 mm, RD x TD, cut by Struers's Minitom) for differential scanning calorimetry (DSC) were prepared to masses of around 50 mg for both AA5083 and AA 5251. The specimens of weldment were cut in the center of weldment AA5083 W8 with the same size of specimens of as-received material.

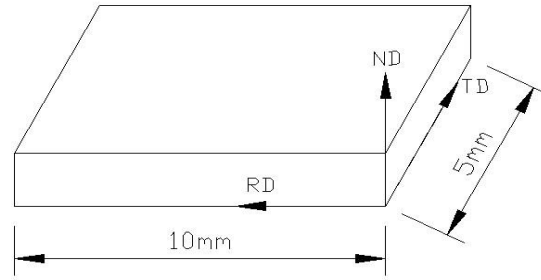


Fig. 3.1 Dimensions and orientation of as-received sheet samples

The process of specimen preparation was the same for the hardness test, optical microscope (OM) and scanning electron microscope (SEM). The cut specimens (as-received, heat treated, and weldment) were cold-mounted in Struers Durofix resin. The mounted specimens were grounded by SiC paper in the sequence of 240, 400, 800 and 1200 grit, then polished with 15, 6, and 3  $\mu\text{m}$  diamond suspensions. The final polishing was conducted with the Struers's OPS (0.05 $\mu\text{m}$ ).

For OM investigation, specimens were electrolytic-etched (anodised) in Barker's reagent (5 ml  $\text{HBF}_4$ , 195 ml  $\text{H}_2\text{O}$ ) using a stainless steel cathode at room temperature with a potential of 15 V for 60 seconds. For the EBSD investigation, the deformed layer of specimens surface, which caused by the grinding and polishing, need to be removed by electropolishing. The electropolishing process was similar to anodising, but a different electrolyte (5ml  $\text{HClO}_4$  in 95 ml  $\text{C}_2\text{H}_5\text{OH}$ ) was used, the process was conducted at under 0  $^\circ\text{C}$  at 20 V for 90 seconds. Fig. 3.2 shows the equipment used for both anodising and electropolishing.

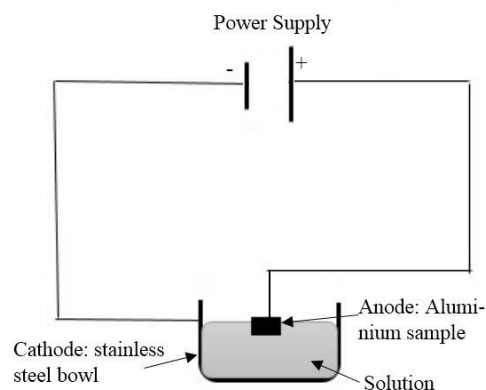


Fig. 3.2. Schematic diagram of the set-up for both anodising and electropolishing

### 3.3 Heat treatment

Recrystallisation annealing was carried out in an ELITE air furnace. Although the furnace chamber was relatively small, there was still a temperature difference between the thermocouple of the furnace and other points in the chamber. Another thermocouple was used to calibrate the temperature of the region where the specimen was placed. When the temperature recorded by the second thermocouple reached the pre-set value and was stable, the sample was inserted into the furnace. After the heat treatment was completed, the sample was taken out as soon as possible and water quenched. Table 3.2 lists the annealing parameters.

Table 3.2 Isothermal annealing parameters for AA5083 H22

Temperature (°C)	Time (s)
250	3600, 5400
275	300, 600, 900, 1800, 2700, 3600, 5400
290	300, 600, 900, 1800, 2700, 3600
300	300, 600, 900, 1800, 2700, 3600
325	300, 600, 900, 1800, 2700, 3600
350	300, 600

### 3.4 Microstructure investigations

#### 3.4.1 Optical Microscopy

Two optical microscopes were used: a Zeiss Akioskop-2 and a Leica DMRX. Samples were studied in polished and anodised conditions. The Zeiss Akioskop-2 optical microscope, equipped with AxioVision 4.6.3 image analysis software, was used to characterise the second-phase particles size and area fraction (along the thickness). The Leica DMRX polarised light microscope with AxioVision 4.6.3 software was used to analyse the grain size, grain shape, the fraction recrystallised and the dimensions of the weldment. In wrought materials, the grain morphology was dependent on the investigated plane. For grain size determination, more than 300 grains were measured on the RD  $\perp$  ND plane. Particle size and area fraction were determined using

AxioVision 4.6.3 software by measuring ten images at a magnification of 500x for each sample.

### 3.4.2 Electron Microscopy

A Philips XL30 scanning electron microscope (SEM), equipped with an Oxford INCA energy dispersive X-ray spectroscopy (EDS) system was used to study the morphology and composition of base-metal, heat-treated samples and weldments from as-polished samples. To identify the composition of second phase particles, ten particles were measured on the  $RD \perp ND$  plane. The SEM was operated at 15 kV for EDS and 20 kV for second electron imaging; the working distance for both was 10 mm.

EBSD was used to characterise the grain size for as-received materials and weldments, and study the micro-texture through the basemetal, heat affected zone (HAZ) and columnar grain zone. Investigations were carried out by field-emission gun FEG-SEM JEOL 7000, equipped with an Oxford INCA crystal EBSD system.

Electropolished samples were used for EBSD, which was carried out on the  $RD \perp ND$  plane. The tested specimen surface was tilted at an angle of  $70^\circ$  from the original stage position, the working distance was 15 mm and the step size was 1  $\mu\text{m}$ .

### 3.4.3 Differential Scanning Calorimetry (DSC)

The recrystallisation kinetics of the as-received materials were studied by DSC. The measurement was carried out by a calorimeter in flowing argon atmosphere. Specimens

were thermally cycled in fully recrystallised Al pans at heating rates of 10, 20, 50 °C/min from 75 °C to 410 °C. A similar mass, fully annealed pure aluminium specimen was used as a reference [75]. For each test sample, the DSC program was performed twice. After the first run, the calorimeter was left to cool down to below the initial temperature without opening the DSC enclosure. The second run was used as a baseline. After subtracting the second run from the first run, any exothermic or endothermic peaks were identified.

### 3.5 Mechanical test

For a weldment, there are different regions which correspond to different microstructures. Microhardness measurements were carried out using a Mitutoyo Vickers-hardnesstester on the RD  $\perp$  ND plane of as-polished specimens. For all specimens, the microhardness was tested at mid-thickness with a 300 g load for 10 seconds. As a general rule, the spacing between the indentations was at least 4 times larger than the diagonal of the indentation. For each sample, at least 10 hardness points were tested.

### 3.6 Software used in this project

Thermal-calc was used to predict the possible phases in the AA5083 and their dissolution temperatures. Matlab 2010a and Comsol Multiphysics 4.4 were used to model the thermal profile for the analytical and numerical methods, respectively.

## Chapter 4 Characterisation of the as-received Material

The composition of as-received AA5083 base metal was determined by EDS with a Philips XL30 scanning electron microscope (SEM) (shown in Table 4.1).

Table 4.1 Composition of AA5083 (in wt %)

	Mg	Si	Mn	Fe	Cr	Zn	Ti	Al
Experimental	4.53	0.15	0.50	0.27	0.05	0	0	Balance
Literature [83]	4-4.90	0.40	0.40-1	0.40	0.05-0.25	0.25	0.15	Balance

### 4.1 Second phase particles

From the analysis of optical microscope and SEM combined with EDS images, the AA5083 alloy in this study mainly contained two kinds of second phase particles: iron-rich (bright) and Mg-rich (dark) (shown in Fig. 4.1). Because of the possible particle stimulation nucleation (PSN) effect during recrystallisation [19], the composition and distribution of the second phase particles were studied.

#### 4.1.1 Composition

Iron-rich particles are divided into two groups according to their compositions (Table 4.2):  $\text{Al}_6(\text{Fe}, \text{Mn})$  and  $\alpha\text{-Al}(\text{Fe}, \text{Mn}, \text{Cr})\text{Si}$ , in which  $\text{Al}_6(\text{Fe}, \text{Mn})$  is dominant. During homogenisation,  $\text{Al}_6(\text{Fe}, \text{Mn})$  can be reshaped and transformed into  $\text{Al}(\text{Fe}, \text{Mn}, \text{Cr})\text{Si}$  [15, 84]. The phase transformation depends on the content of Si. The content of Si in AA5083 is relatively low (0.15 wt %) [3], so there is still more  $\text{Al}_6(\text{Fe}, \text{Mn})$  is still more than  $\alpha\text{-Al}(\text{Fe}, \text{Mn})\text{Si}$ .

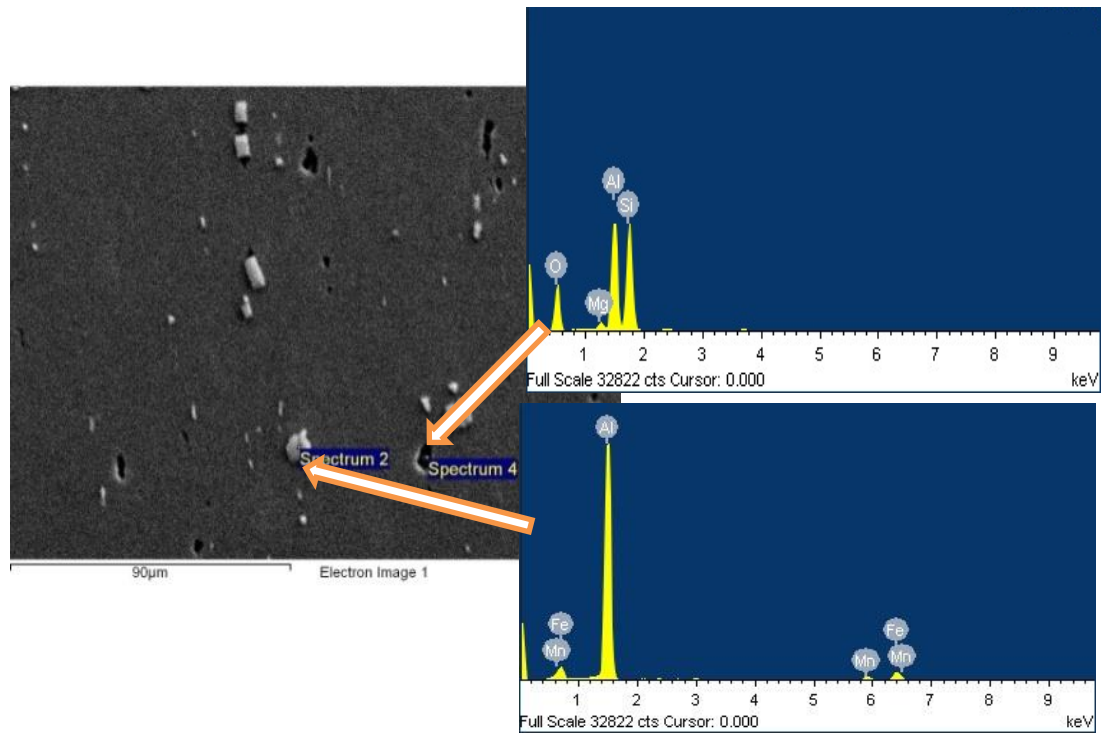


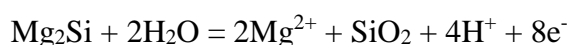
Fig. 4.1 SEM image of second-phase particle morphology and EDS spectra at two different points

Table 4.2 Composition of iron-rich particles (all in atom %)

Al	Si	Cr	Mn	Fe	Al/(Cr+Mn+Fe)	Al/Si
85.62	0.00	0.18	4.06	10.15	5.95	0
84.27	0.00	0.00	5.39	9.94	5.50	0
83.99	0.00	0.00	2.22	13.04	5.50	0
85.44	0.00	0.28	5.04	9.12	5.92	0
85.33	0.00	0.27	4.99	9.41	5.82	0
85.27	0.00	0.00	4.09	10.64	5.79	0
77.21	4.86	0.81	6.14	10.99	4.30	15.89
77.36	5.07	0.71	6.43	10.43	4.40	15.26



According to the EDS results of the Mg-rich particle, the average ratio of Mg to Si in the Mg-rich particles is 1.75:1. This ratio is slightly lower than that for stoichiometric  $\text{Mg}_2\text{Si}$  (shown in Fig. 4.2). After polishing, the position corresponding to Mg-riched particles was a little lower than the Al matrix. Tanem[85] found that different sample preparations could cause different ratios of Mg to Si for the same material, and it was believed that Mg was dealloyed from the  $\text{Mg}_2\text{Si}$  phases during mechanical grinding and polishing [85, 86]. During grinding and polishing, there was an electrochemical reaction occurring, the  $\text{Mg}_2\text{Si}$  was anode and the Al-matrix was cathode. The reaction was:



$\text{Mg}^{2+}$  was gone with water, and  $\text{SiO}_2$  was deposited on the remaining particles to prevent further electrochemical reaction. This could explain well the phenomena that the ratio of Mg to Si was lower than the stoichiometric  $\text{Mg}_2\text{Si}$ .

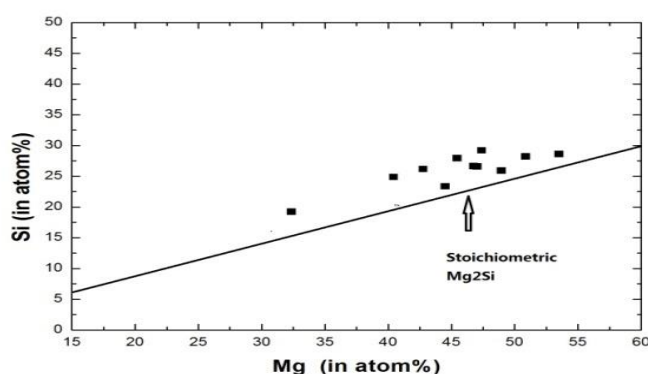


Fig. 4.2 Summary EDS results of the Mg/Si ratio of Mg-rich particle and stoichiometric composition of  $\text{Mg}_2\text{Si}$

#### 4.1.2 Second phase particle distribution

The as-received AA5083 alloy contains particles that range widely in size (from 0.5 $\mu$ m to 7 $\mu$ m). The particle sizes of interest with respect to PSN are above 1  $\mu$ m [41]. Tables 4.3 and Fig 4.3 show the characterisation distribution of the second phase particles. The area fraction of iron-rich particles and Mg-rich particles are  $1.5 \pm 0.3\%$  and  $0.35 \pm 0.18\%$ , respectively. The area fraction of the iron-rich particles is much bigger than that of the Mg-rich particles.

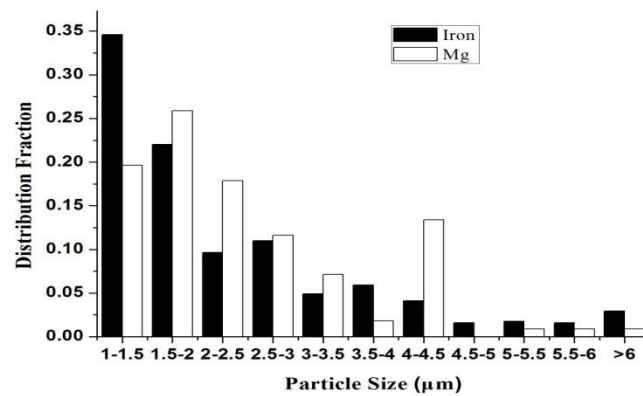


Fig. 4.3 Particle size distribution in the middle of the RD-ND plane

Table 4.3 Particle size, average diameter and particle density

Position			Area Fraction(*10 <sup>-2</sup> )	Average Diameter ( $\mu$ m)	Particle Density (number/mm <sup>2</sup> )
ND-RD plane	Middle	Iron	$1.50 \pm 0.31$	$2.4 \pm 0.1$	2820
		Mg	$0.35 \pm 0.18$	$2.5 \pm 0.4$	731
	Top	Iron	$1.7 \pm 0.34$	$2.3 \pm 0.4$	3260
		Mg	$0.50 \pm 0.3$	$2.4 \pm 0.2$	855
ND-TD plane	Middle	Iron	$1.50 \pm 0.3$	$2.4 \pm 0.2$	2622
		Mg	$0.43 \pm 0.2$	$2.4 \pm 0.3$	807
	Top	Iron	$1.62 \pm 0.26$	$2.3 \pm 0.2$	3160
		Mg	$0.52 \pm 0.2$	$2.4 \pm 0.2$	727

The distribution of the second phase particles is not homogenous according to the different positions of certain observation planes, and the density of the middle of the ND-RD plane is lower than that of the top position of the ND-RD plane. This could be attributed to the different strain distributions from the top to the middle thickness of the sheet. During rolling, a large second phase particle could be crushed into several smaller ones along the rolling direction (shown in Fig. 4.4). With a larger strain of the top position, more crushed smaller particles would be produced.

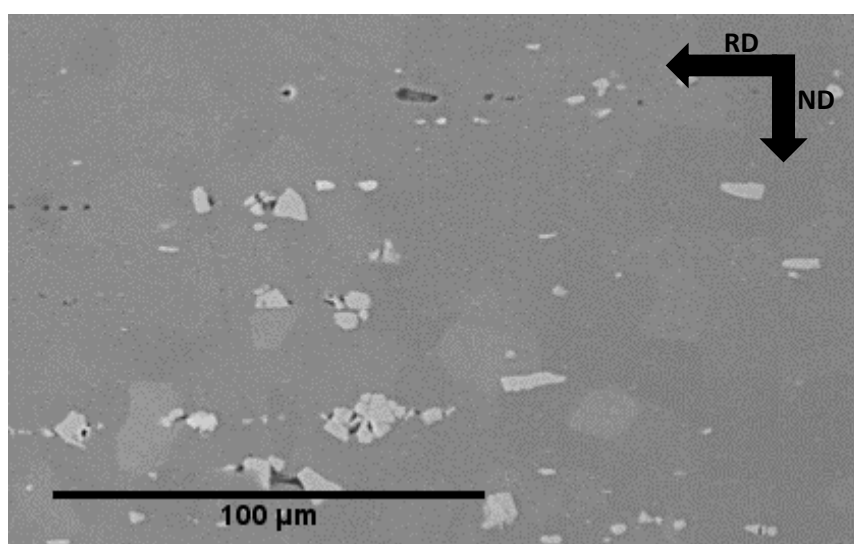


Fig. 4.4 SEM image showing the crushed second phase particles

## 4.2 Grain microstructure characterisation

### 4.2.1 Grain size

Both anodising and EBSD were used to reveal the grain microstructure of the as-received material. It can be seen from Fig. 4.5 that the grains are elongated along the RD in the as-received AA5083 H22. The average grain size changes across the thickness on the observation plane of RD-ND. Near to the surface, the average grain

size is  $10.2\ \mu\text{m}$ , and in the middle of the plane of RD-ND, the average grain size increases to  $13.7\ \mu\text{m}$ .

Table 4.4 Grain size of the as-received AA5083 sheet

Position		Length( $\mu\text{m}$ )	Width( $\mu\text{m}$ )	Equivalent Diameter( $\mu\text{m}$ )
Longitude	Middle	$26\pm 11.7$	$8.9\pm 3.6$	$13.7\pm 5.0$
	Near to surface	$18.6\pm 6.9$	$6.7\pm 2.3$	$10.2\pm 3.2$

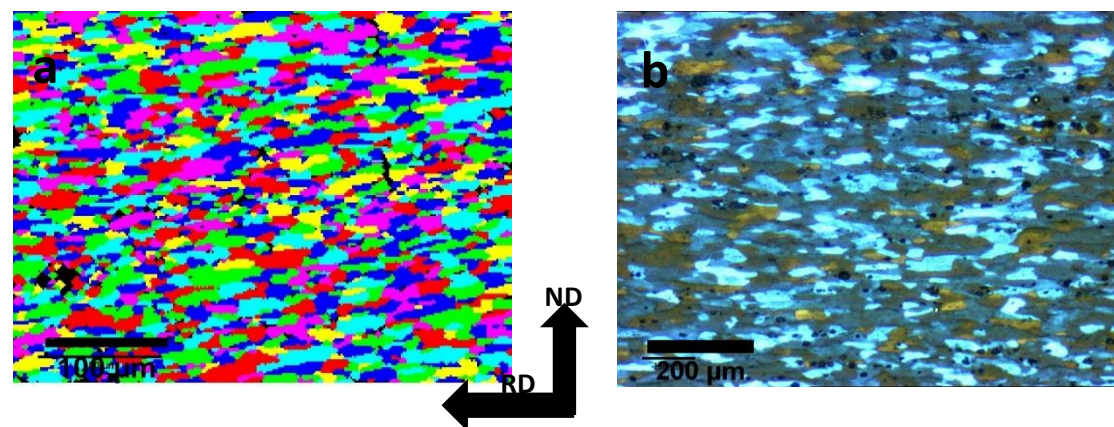


Fig. 4.5 Microstructure of as-received AA5083, a: revealed by EBSD; b: revealed by polarised OM after anodising

#### 4.2.2 Texture of as-received AA5083

Fig. 4.6 presents the orientation imaging microscopy (OIM) image of as-received material, which shows that there are obvious orientations (rolling direction //  $\langle 111 \rangle$ , rolling plane //  $\{101\}$ ). Based on the colour in the images, OIM images could provide

a rough judgement about whether there is orientation or not, but can not provide quantitative information about texture.

Fig. 4.7 is the inverse pole figure of the as-received material. With the help of the Oxford INCA crystal EBSD system, the textures could be quantitatively measured, and the results are shown in Table 4.5. There are three main textures in the as-received material: Brass, S and Copper. The three textures are the three major components of  $\beta$ -fibre (shown in Fig. 2.6) [19]. According to Hirsch and Lucke's results [54], the  $\beta$ -fibre was dominant only when the reduction reached 95% during the rolling process, so, it can be concluded that the as-received materials must have experienced a severe reduction.

Table 4.5 Textures of the as-received materials

Texture	Area percentage
Brass {011}<211>	14.8
S {123}<634>	32.3
Copper{112}<111>	22.5

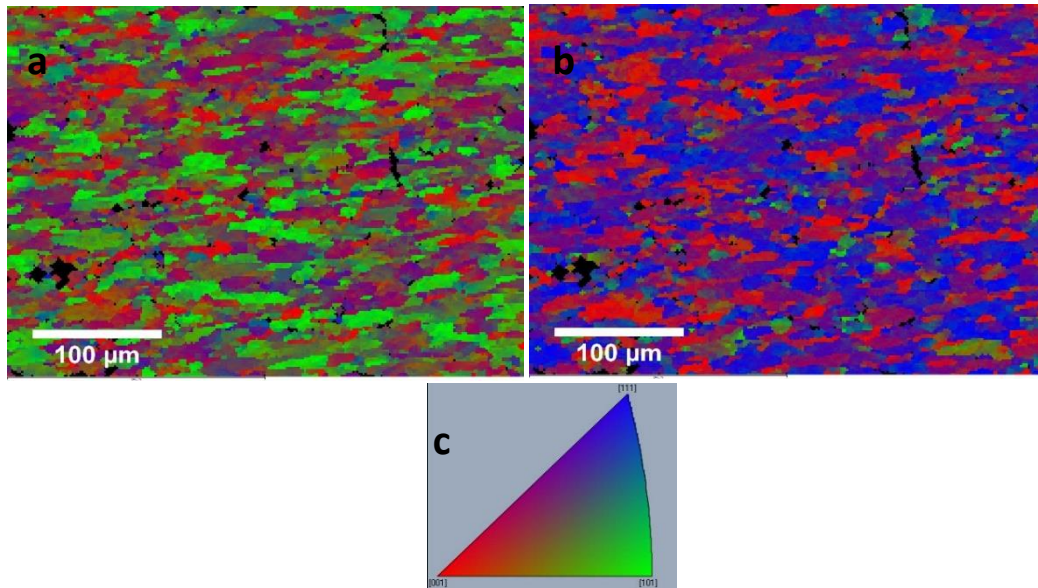


Fig 4.6 OIM image, a: the normal direction; b: the rolling direction; c: the relationship between index and colour

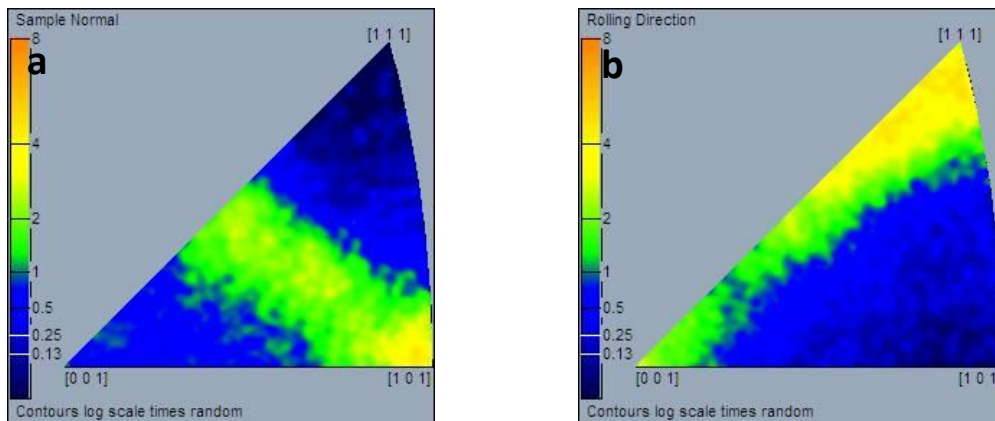


Fig 4.7 Inverse pole figure of as-received AA5083, a: the normal direction; b: the rolling direction; c: the relationship between index and colour

### 4.3 Summary

The microstructure (second phase particle, grain size and texture) was measured for the AA5083 H22 sheet. Second phase particles were divided into two kinds: iron-rich and Mg-rich. The distribution of large particles ( $D > 1 \mu\text{m}$ ), which could have a particle

simulated nucleation mechanism effect on the recrystallisation process, was found to be inhomogeneous through thickness. In addition, the average grain size varied with the thickness as well. The texture analysis showed that there were three typical deformed textures: Brass, S and Copper, which were the components of  $\beta$ -fibre that were formed after severely rolling reduction.

## Chapter 5 Annealing phenomena

### 5.1 The effects of second phase particles on the DSC curve

The annealing phenomena were studied by DSC. The DSC testing was run twice for the same sample without opening the chamber, and the second run provided the baseline.

Fig. 5.1 shows the two runs of AA5083 H22 with a 20 °C/min heating rate. After comparing these, two peaks emerged. One is endothermic (from 150-220 °C) and the other is exothermic (from around 310 °C).

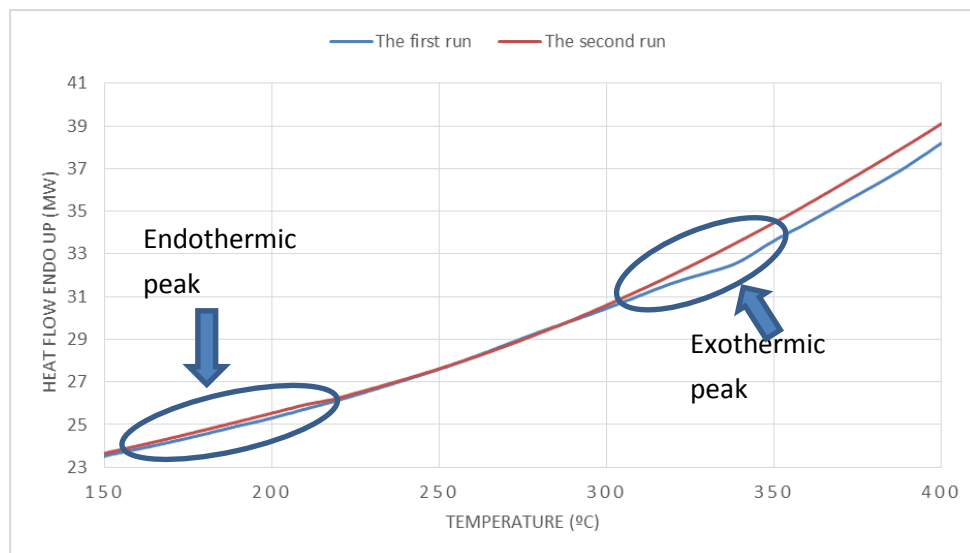


Fig 5.1 DSC curve after the subtraction of two runs with 20 °C/min



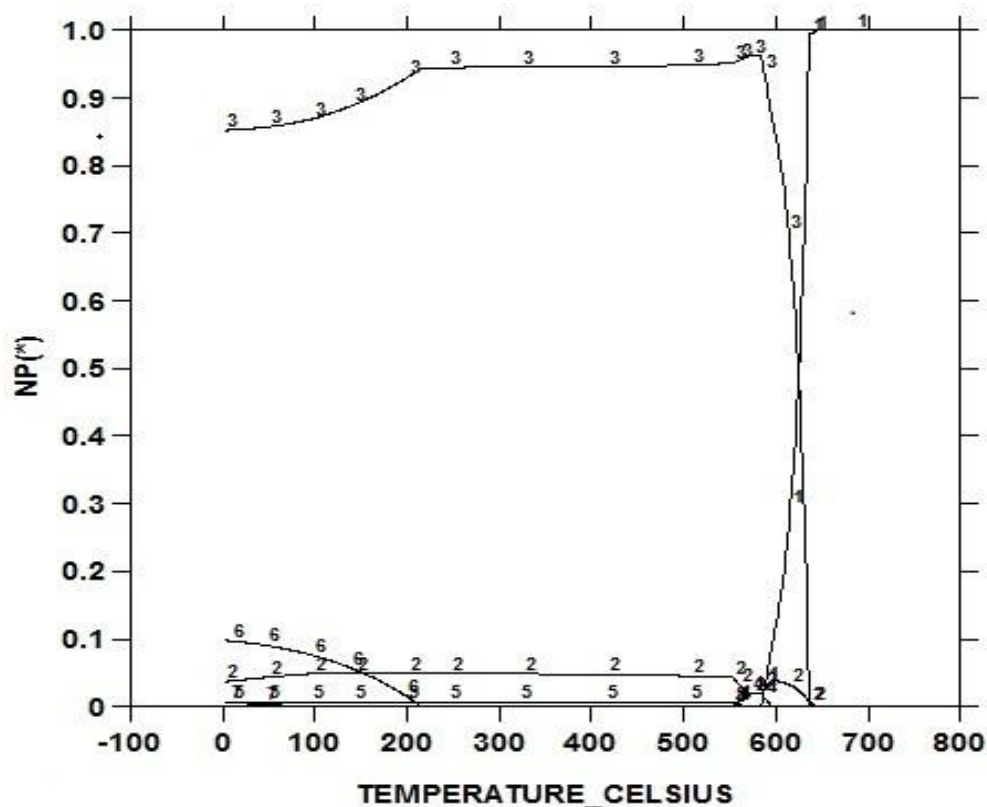


Fig. 5.2 Phase diagram calculated through Thermo-Calc: 1, Liquid; 2,  $\text{Al}_6\text{Mn}$ ; 3, Al; 4,  $\alpha$ -phase, 5,  $\text{Mg}_2\text{Si}$ ; 6,  $\text{Al}_2\text{Mg}_3$ .

For commercial Al-alloys, there are lots of second phase particles which could precipitate or dissolve during the heating process then affect the peak of recovery, recrystallisation and grain growth. For commercial AA5083, according to the Thermo-calc calculation results, only  $\text{Al}_2\text{Mg}_3$  would change in the temperature range related to recovery and recrystallisation. The equilibrium dissolution temperature of  $\text{Al}_2\text{Mg}_3$  is around 220 °C, so the first endothermic peak of the DSC curve could be related to the dissolution of  $\text{Al}_2\text{Mg}_3$ .

Commercial AA5083 H22 has gone through partial annealing which favours to the precipitation of  $\text{Al}_2\text{Mg}_3$  along the grain boundary. The grain microstructure could be revealed by 10%  $\text{H}_3\text{PO}_4$  at 60 °C for 90 seconds. The mechanism of this etch is that

$\text{Al}_2\text{Mg}_3$  had low potential compared to the aluminium matrix ( $\text{Al}_2\text{Mg}_3$  has a corrosion potential of about  $-1.29\text{V}$  (SCE) compared to the  $-0.73\text{V}$  (SCE) of the matrix [87]), and would be dissolved as an anode in corrosion conditions. However, this etch method could not be used to reveal the microstructure change after annealing at a higher temperature than  $230\text{ }^\circ\text{C}$  [82]. The explanation of the failed etch is the dissolution of  $\text{Al}_2\text{Mg}_3$  particles at temperatures under  $230\text{ }^\circ\text{C}$ .

The hardness test and electrical resistivity were also compared with the DSC results. Larger samples ( $10 \times 60 \times 1.6$  (mm), RD x TD x ND) were heat-treated to certain temperatures in a normal furnace at the same heating rate as the DSC test, and the hardness and electrical resistivity were tested before and after heat treatment. The hardness was carried out directly on the RD x TD plane without mounting. The results of hardness and electrical resistivity are shown in Tables 5.1 and 5.2, respectively. It is well known that a solid solution would increase the electrical resistivity, so the increase in electrical resistivity was attributed to the dissolution of  $\text{Al}_2\text{Mg}_3$ . When the temperature rises over the  $310\text{ }^\circ\text{C}$ , the hardness starts to decrease, so the initial temperature of recrystallisation for this DSC test is around  $310\text{ }^\circ\text{C}$ .

Table 5.1 Electrical Resistivity ( $10^{-8}\ \Omega\cdot\text{m}$ )

	230 $^\circ\text{C}$	275 $^\circ\text{C}$	310 $^\circ\text{C}$	400 $^\circ\text{C}$
Before heat- treatment	$6.05 \pm 0.3$	$6.04 \pm 0.2$	$6.03 \pm 0.3$	$6.01 \pm 0.2$
After heat-treatment	$6.13 \pm 0.2$	$6.12 \pm 0.2$	$6.16 \pm 0.05$	$6.15 \pm 0.2$

Table 5.2 Hardness Testing before and after heat-treatment (Hv)

	220 °C	275 °C	310 °C	400 °C
Before heat-treatment	101.9 ± 0.5	100.5 ± 1.1	100.8 ± 0.9	100 ± 1
After heat-treatment	100.7 ± 0.6	101.1 ± 1.2	99.7 ± 0.7	74.6 ± 1.3

## 5.2 Recrystallisation studied by DSC

The recrystallisation is an exothermic process, and the fraction of recrystallisation can be calculated by the following equation:

$$F_R = \frac{E_r}{E} \quad \text{Equation 5.1}$$

where  $F_R$  is the fraction of the recrystallised fraction,  $E_r$  is the energy released at a certain temperature and E is the total energy released.

Fig 5.3 shows the method for identifying the initial and finishing temperature of recrystallisation. The method aims to establish the intersection of two tangent lines on both sides of the transition point [88]. After obtaining the two temperatures, the exothermic peak would be taken out and analysed separately, as shown in Fig. 5.4. The total energy and the energy released at a certain temperature were calculated using Matlab software, which divided the calculating area into basic trapezoids with the same temperature step  $\Delta T$ .  $\Delta T$  was determined by the collection rate of DSC.

The relationship between the recrystallisation fraction and temperature could also be built based on Fig.5.4. Fig 5.5 shows the corresponding results with 3 different heating

rates: 10, 20, and 50 °C/ min. The three curves are S-shaped, which is similar to the shape of isothermal recrystallisation.

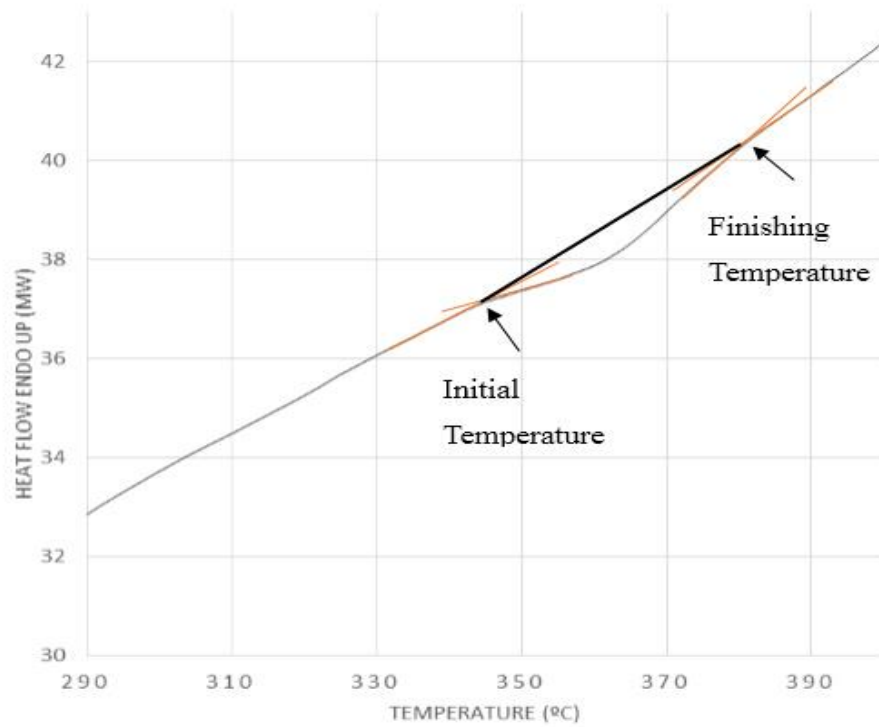


Fig. 5.3 Method for identifying the initial and finishing temperature of recrystallisation

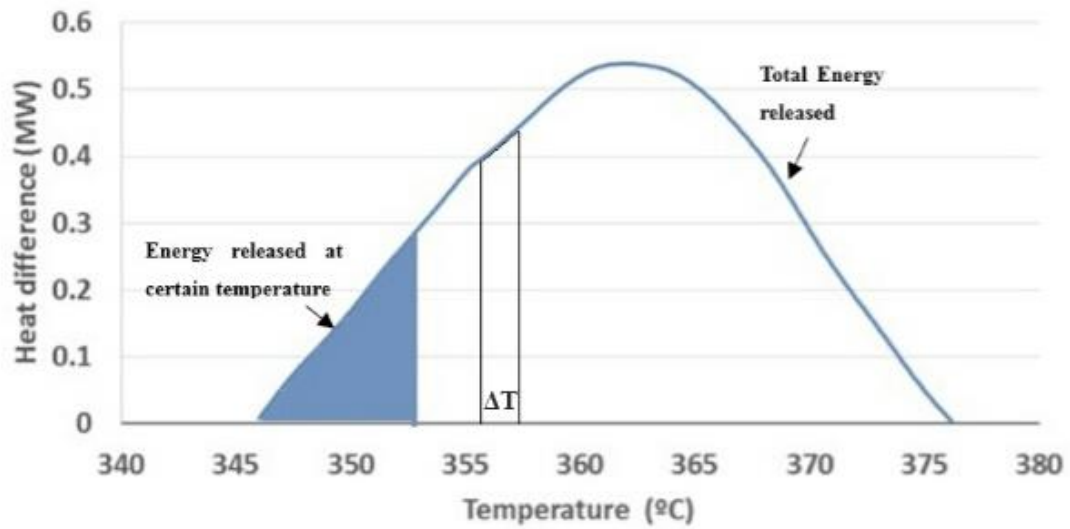


Fig. 5. 4 The recrystallisation fraction calculation method

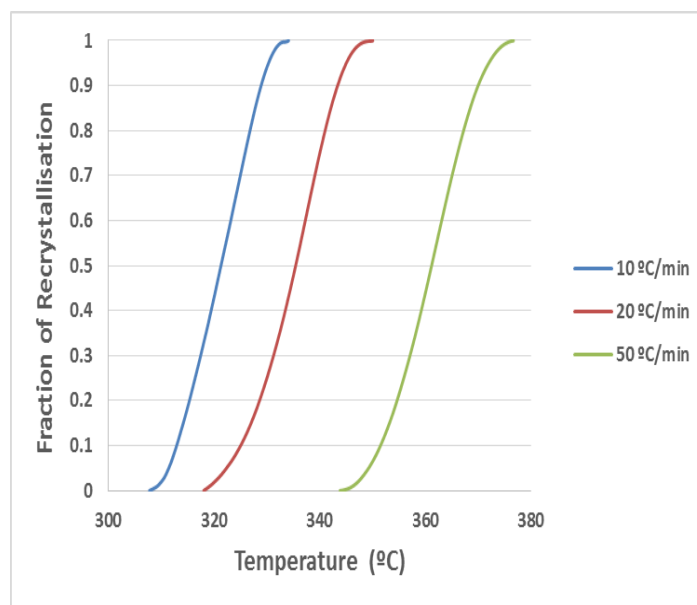


Fig. 5.5 Curve of temperature versus fraction of recrystallisation with different heating rate

The activation energy could be derived from the DSC results with different linear heating rate processes. There are lots of methods available to calculate the activation energy. All of these methods are from the basic well known equation:

$$\ln t = \frac{E}{RT_{iso}} + C \quad \text{Equation 5.2}$$

where  $t$  is the time required for certain recrystallisation fractions at different isothermal heat-treatment temperatures.

The equation is only applied in isothermal heat treatment. For the DSC linear heating rate, a concept of equivalent time needs to be introduced, which is the time required for isothermal heat treatment to have the same recrystallised fraction as non-isothermal heat treatment. The Kissinger method [89] was widely used to obtain the activation energy from the results of DSC. It can be expressed as:

$$\ln\left(\frac{r}{T_p^n}\right) = -\frac{E}{RT_p} + \ln\left(\frac{C_1}{E}\right) \quad \text{Equation 5.3 [89]}$$

Where  $r$  is the linear heating rate,  $T_p$  is the peak temperature for certain recrystallised fraction, and  $E$  is the activation energy.

Three different heating rates are employed in the current study, which are sufficient to calculate the activation energy. The temperatures were 325.3, 337.9, and 360.5 °C, which produced a 0.5 recrystallised fraction at the different heat rates (10, 20 and 50 °C/min). Fig 5.6 is the plot of  $\ln\left(\frac{r}{T_p^n}\right)$  versus  $\frac{1}{RT_p}$ . The activation energy is the slope of the curve, and the value is 142.2 kJ/mole. In fact, the fraction results from DSC are continuous, and it is possible to obtain the activation energy for different recrystallised fractions. Fig. 5.7 shows the activation energy from the 0.1 to 0.9 recrystallised fraction. The energy increases linearly with the fraction of recrystallisation from 126 to 150 kJ/mol.

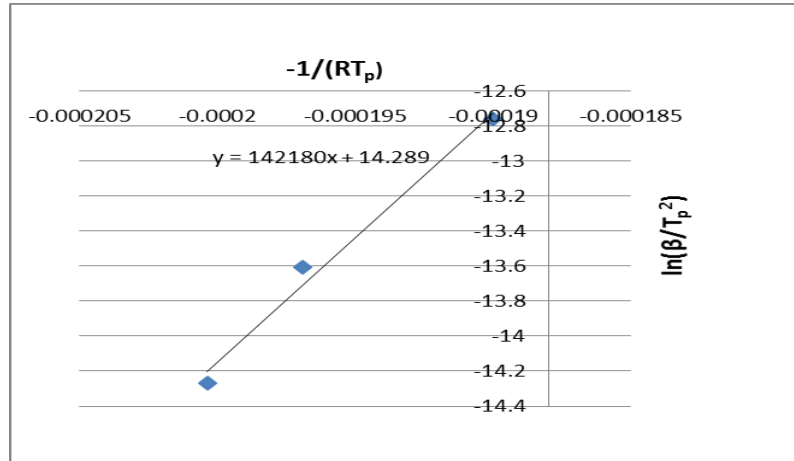


Fig 5.6 Plot of  $\ln(\frac{r}{T_p^n})$  versus  $\frac{1}{RT_p}$  with 0.5 recrystallised fraction

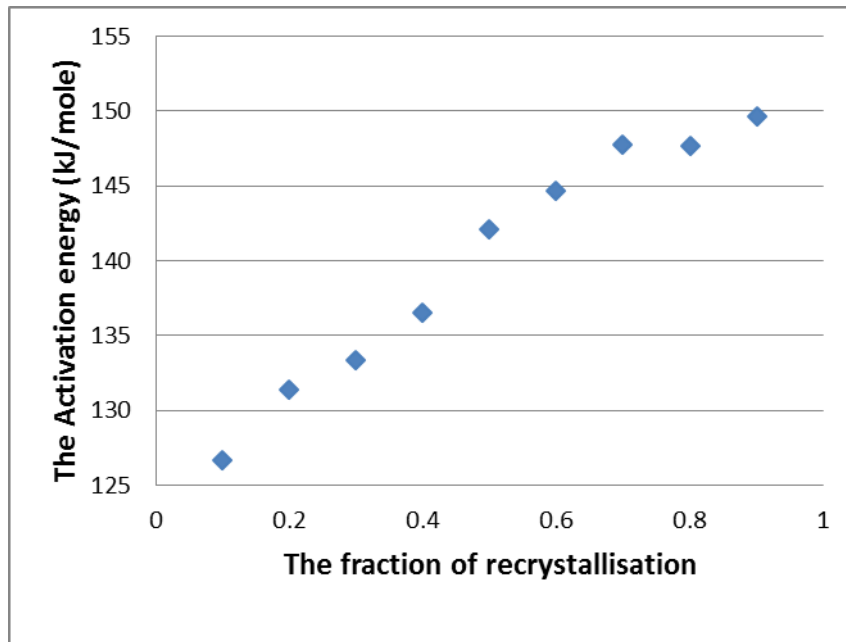


Fig. 5.7 Activation energy for different recrystallised fractions

### 5.3 Recrystallisation studied by Micro-hardness

Micro-hardness is used to study the recrystallisation. The fraction is calculated by the softening equation:

$$F = \frac{H - H_i}{H_o - H_i} \quad \text{Equation 5.4}$$

Where  $H_i$  is the microhardness following heat treatment, and  $H_o$  and  $H$  are the hardness of full annealed and as-received states, respectively.

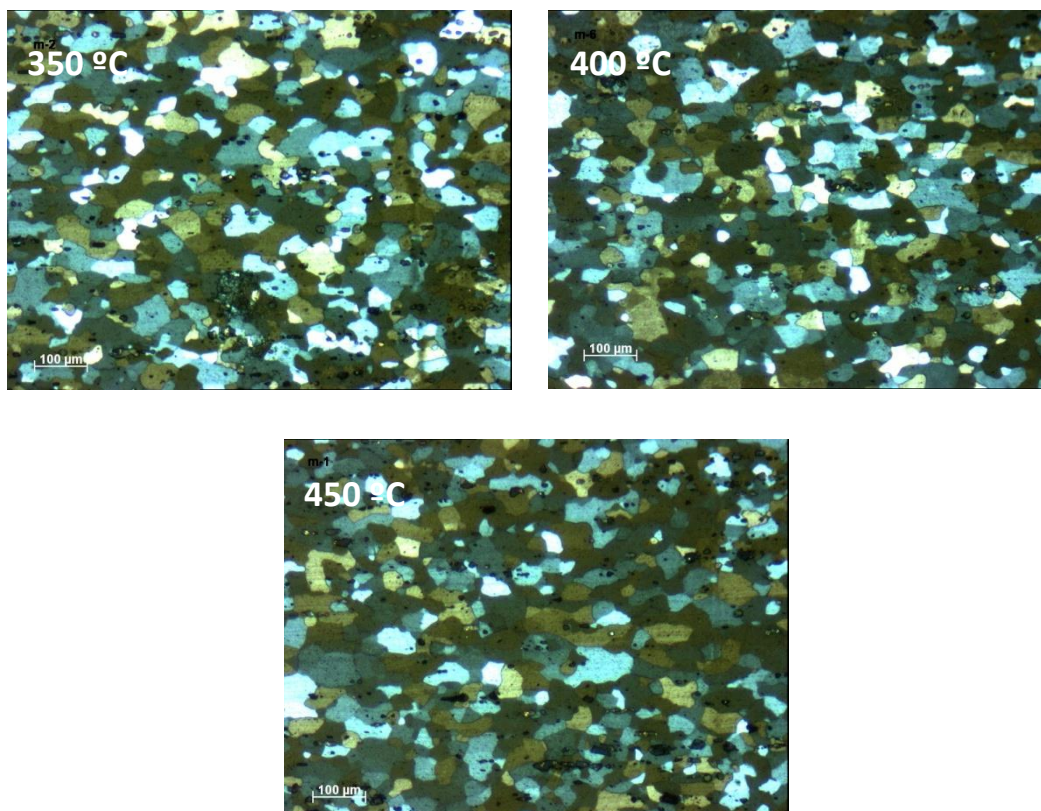


Fig 5.8 Grain microstructure of the samples after 1 hour of heat treatment at 350, 400, and 450 °C

The hardness of the as-received material is  $96.7 \pm 0.4$  Hv. The hardness of the annealed state needs to exclude the effects of precipitation, solid solution and grain growth. From the calculation of the Thermo-calc (shown in Fig. 5.2), there is no reaction related to precipitation or solid solution for the range from 350 to 450 °C. The samples were heat treated at 350, 400 and 450 °C for one hour. Fig. 5.8 is the grain microstructure of these three states after anodising. It is hard to find obvious difference among the three states. Table 5.3 shows the grain size and hardness the samples after one hour of heat treatment.



There is little difference between the grain size and hardness of the three states, so it can be concluded that no grain growth occurred during these heat treatments. The hardness of the full annealed state is 72.3 Hv (the average value of these three states).

Table 5.3 Grain size and the hardness of samples after one hour of heat treatment

Temperature ( °C)	ECD (μm)	Hardness (Hv)
As-received	13.7±5.0	96.7 ±0.8
350	16.0±8.2	72.2 ±0.4
400	16.7±7.7	72.3 ±0.7
450	16.5±7.2	72.5 ±0.5

The heat treatment temperature ranged from 250 °C to 450 °C, and the holding time ranged from 5 to 60 mins (holding times of 75mins and 90 mins were only for the 275 °C heat treatment). All of the hardness of the heat-treated samples were measured. Following heat treatment at 250 °C for 60 mins, the hardness of the sample only dropped to 96.3 ± 0.6, and was virtually the same as that of the as-received material. When the temperature exceeded 325 °C, the recrystallisation was nearly complete within 5 min, and there were insufficient data points for the calculation of the Avrami exponent and activation energy. Only the hardness data of 275, 290 and 300 °C were useful for the current study. Fig5.9 shows that the hardness changes with time at the different isothermal heat treatment temperatures: 275, 290 and 300 °C. With the increase in temperature, the rate of recrystallisation increased. Full recrystallisation would take

around 1800s and 3600s at 290 and 300 °C, respectively. The hardness only decreased to 75.5 Hv when the sample was heat-treated at 275 °C for 5400s.

The hardness might correspond to certain fractions of recrystallisation through the softening Equation 5.4. Fig. 5.10 shows the curve of the recrystallised fraction versus time.

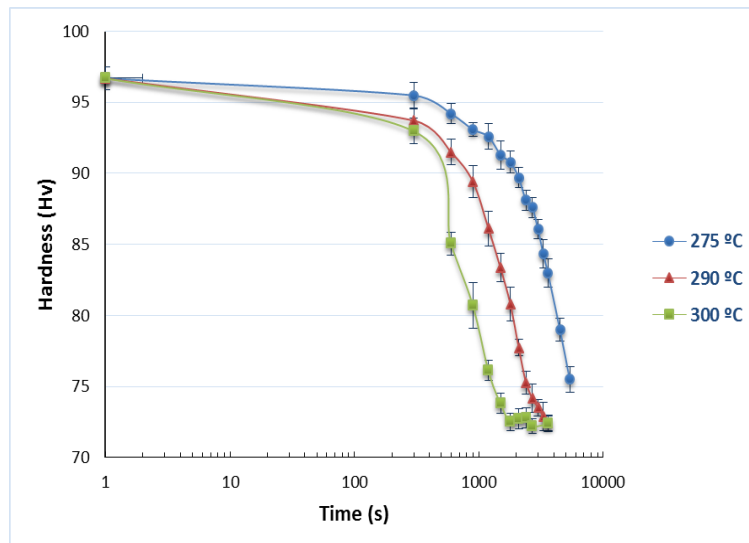


Fig 5.9 Relationship between hardness and time

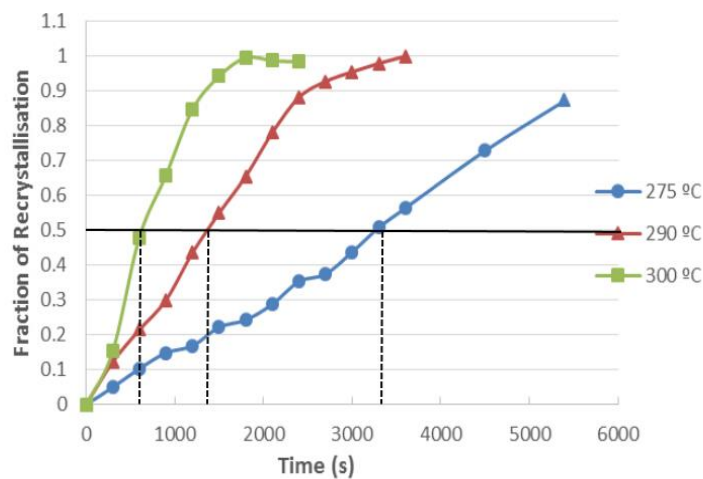


Fig. 5.10 Curve of the recrystallised fraction versus time

### 5.3.1 Activation energy

The fraction results could be used to calculate the activation energy for the recrystallisation. The calculation was based on Equation 5.2

$$\ln t = \frac{E}{RT_{iso}} + C \quad \text{Equation 5.2}$$

The time required for 0.5 fraction recrystallisation usually used to be calculated the activation energy [90, 91]. In fact, it is hard to determine the accurate same recrystallised fraction for different isothermal heat treatments. For the discrete recrystallised fraction data points, the time for certain fractions needs to be calculated using the interpolation method. For a typical fraction vs time curve, the middle section could be treated as a straight line, which makes the interpolation very simple. The calculated time for 0.5 recrystallisation is listed in Table 5.4.

Table 5.4 Calculated time for 0.5 recrystallisation

Temperature ( °C)	275	290	300
Time (s)	3226	1315	635

Fig. 5.11 shows the calculated result for the activation energy of recrystallisation. The value is 145.6 kJ/mol. This value is similar to the result from the DSC measurement. Both methods are reasonable for evaluating the activation energy.

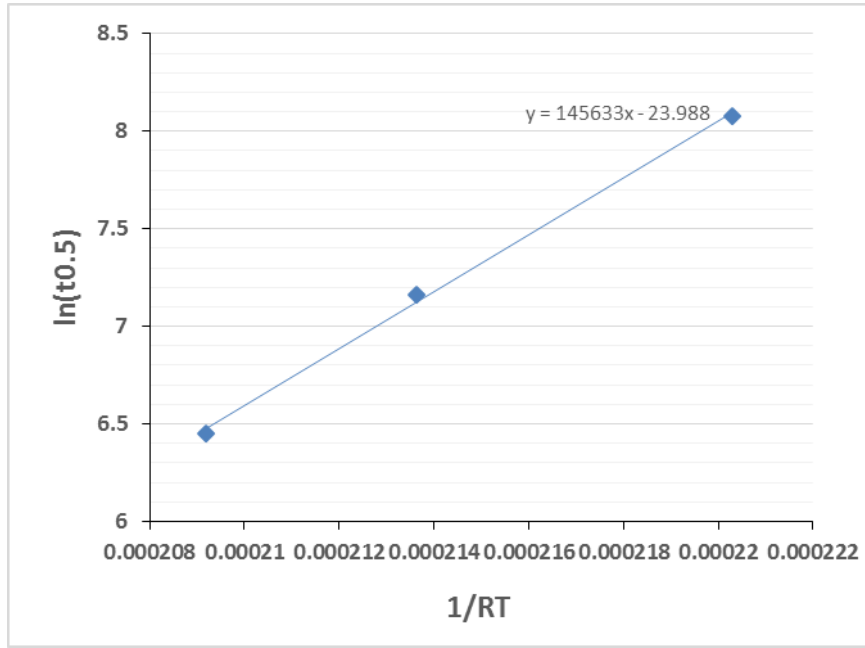


Fig. 5.11 The curve of  $1/(RT)$  versus  $\ln(t_{0.5})$

### 5.3.2 Avrami exponent

The JMAK equation is proposed to study the kinetics of phase transformation [19]. The classic JMAK equation is:

$$X = 1 - \exp(1 - kt^n) \quad \text{Equation 5.5}$$

Where  $X$  is the recrystallised fraction,  $k$  is a constant and  $n$  is the Avrami exponent.

Equation 5.4 could be easily transformed into:

$$\log_{10}(-\ln(1 - X)) = n \log_{10}t + \log_{10}k \quad \text{Equation 5.6}$$

$n$  is the slope of plot of  $\log_{10}(-\ln(1 - X))$  against  $\log_{10}t$ .

The Avrami exponent of 275 °C and 290 °C changed with the recrystallised fraction.

Initially, the slopes are 0.96 and 0.91 for 275 °C and 290 °C, respectively. With the increase in the recrystallised fraction, the exponents increased to 1.80 and 1.9. For the

curve of 300 °C, there are fewer data points for the lower recrystallised fraction. For the curve of 300 °C, the starting point does not affect the overall trend line, and the slope is 1.84.

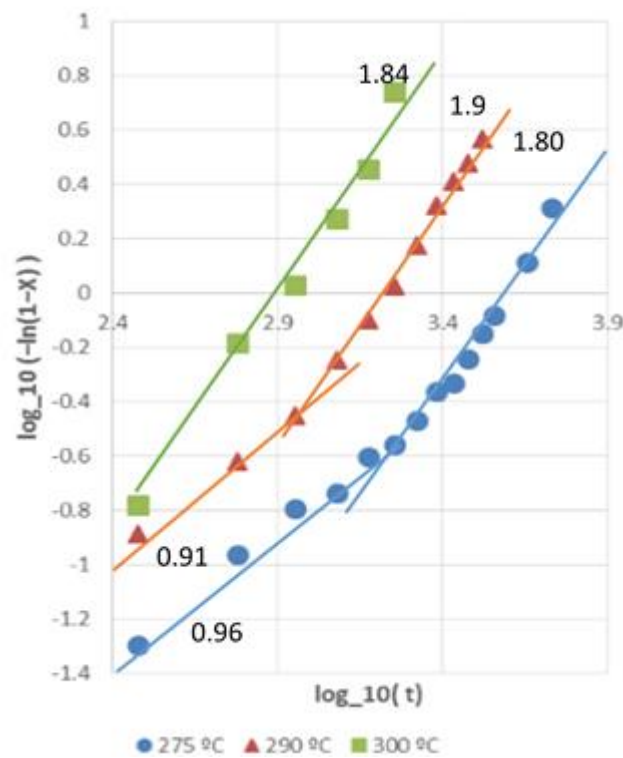


Fig. 5.12 Plot of  $\log_{10}(-\ln(1-X))$  versus  $\log_{10}t$

The initial predicted Avrami exponent is 4, which is based on the assumption that the nucleation sites are random, and the rates of nucleation and ensuing grain growth are constant. In fact, the experimental Avrami exponent is always below 4. Table 5.5 shows the Avrami exponent resulting from the above two factors. One of the factors was the nucleation rate. For site saturated nucleation (nucleation only occurring at the beginning of recrystallisation), the theory Avrami exponent is 3. Another factor which could affect the Avrami exponent is the growth dimension factor. When the recrystallisation nucleus

grows in 1 or 2 dimensions, the Avrami exponent would decrease by 1.

Table 5.5 Theory Avrami exponent [19]

Growth Dimension	Site saturated nucleation	Constant nucleation rate
3-D	3	4
2-D	2	3
1-D	1	2

It should be noted, for the theory of Avrami exponent deduction, that the nucleation sites are randomly distributed and that there was no nuclei incubation time. In real recrystallisation, nucleation always occurs at the preferential sites, such as grain boundary and sites near to the second phase particles. This would result in a lower Avrami exponent. In Marthinsen's modelling work[65], the predicted exponent was 2 under the assumption that nucleation occurs at appointed sites. In the literature [65, 92], there was no exponent less than 1. This is because, in the current study, the as-received AA5083 H22 had undergone industrial recovery stabilisation heat-treatment, so the stored energy is reduced; when it goes through recrystallisation, it would need more time to form nuclei. The same exponent trend was observed by previous researchers in the annealing process of AA5251 H34 [82].

#### 5.4 Microstructure characterisation during annealing

In the EBSD experiment, the quality of the Kikuchi pattern in each scanned point would produce image quality (IQ) mapping. The IQ mapping can be used to analyse the

annealing phenomena. The Kikuchi pattern could be affected by several factors, such as: the grain boundary, residual stress, the surface deformation caused by sample preparation, and so on. If only recrystallised grains are compared to the deformed matrix, the recrystallised grain have better Kikuchi quality than that of the deformed matrix, and the new recrystallised grain would appear brighter in IQ mapping.

For material with second phase particles, there is another quality influence factor of sample flatness caused by electric polishing. In the aluminium matrix, the second phase particles have a different potential. Compared with the matrix aluminium, Mg-riched particles have lower potential and Fe-riched particles have higher potential. During electrical polishing, the Mg-riched particles were anode and would be consumed, then leave small pits; the Fe-riched particles were cathode, and the matrix around them was the anode, which would be consumed. Fig. 5.13 shows the flatness of sample after polishing. It should be noticed that some Fe-riched particles could be detached from the matrix. The detachment would reduce the density of the Fe-riched particles.

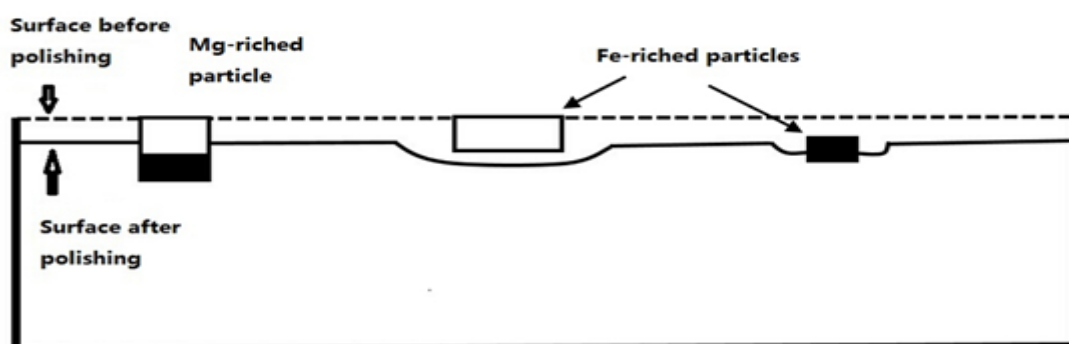


Fig.5.13 The changes of the surface flatness after electric polishing

For EBSD technique, the sample need to be tilted  $70^\circ$  relative to the normal incidence of the electron beam[48]. For the surface shown in Fig. 5.13, the regions near to the second phase have different flatness from the matrix, so the relative angle in those regions always deviates from the optimized angle. The deviation resulted in a bad Kikuchi pattern (dark in quality image).

Fig. 5.14 shows the IQ mappings of the sample after heat-treatment at  $275^\circ\text{C}$  for 15, 25, 40 and 55 mins, respectively. It could be seen that there are no observable recrystallised grains appearing in the sample of 15 mins heat-treatment. The first 15 mins could be defined as the incubation time during which the nucleation would occur. During incubation period, the softening mechanism is different from the growing period of recrystallisation. When the heat-treatment time was increased to 25 mins, observable recrystallised grains appeared in the sample. Most of the new recrystallised grains relate to second phase particles. This phenomenon is obvious in the sample after 55 mins of heat-treatment. It can be concluded that the PSN is a dominant nucleation mechanism for the current researched material.



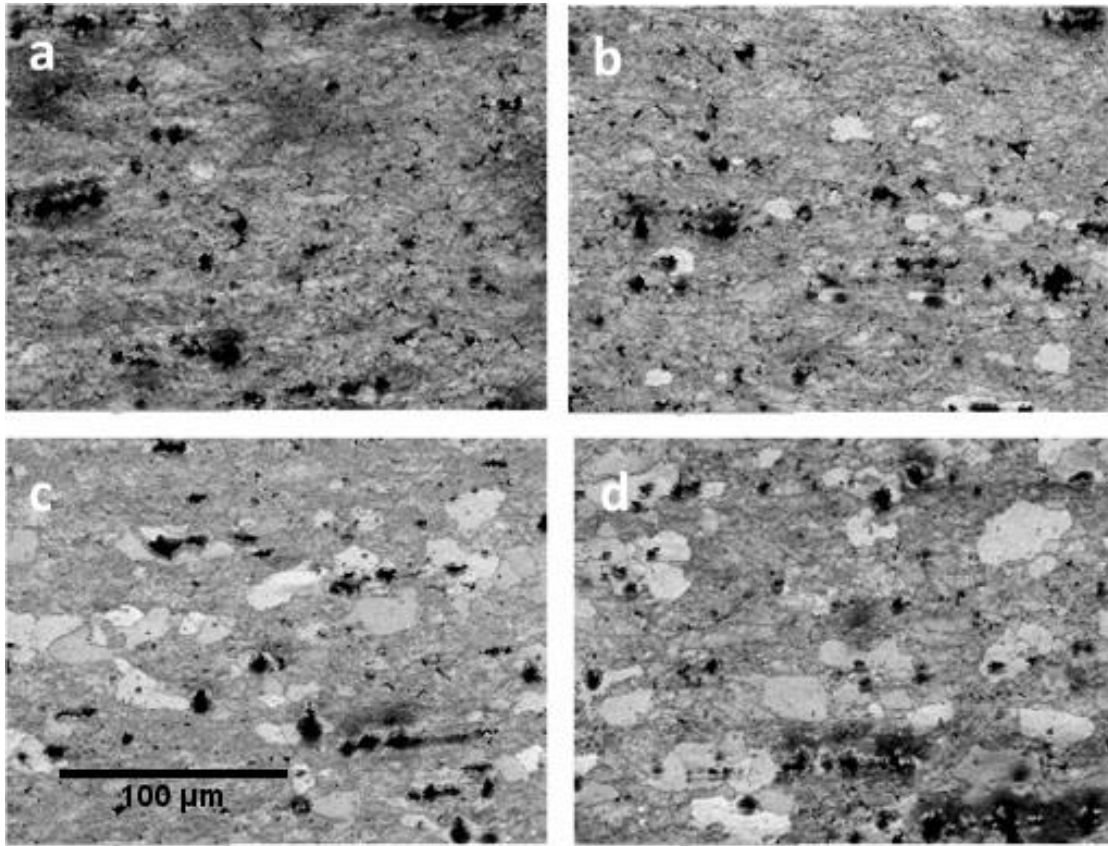


Fig. 5.14 The IQ mappings of sample after heat-treatment at 275 °C for 15 (a), 25 (b), 40 (c) and 55 (d) mins, respectively (the four images have the same magnification)

## 5.5 Summary

The annealing phenomena were studied for AA5083 H22. The activation energy of recrystallisation was determined by DSC and hardness testing, respectively. The results of both methods showed a reasonable agreement. The activation energy was around 145 kJ/mol when the recrystallised fraction was 50%. The Avrami exponent for the recrystallisation of the kinetic JMAK equation was calculated. The lower exponent corresponds to the nuclei's incubation period, and the higher exponent corresponds to the grain growth period of recrystallisation. The EBSD results confirmed that the major recrystallisation nucleation mechanism is particle stimulation nucleation (PSN).

## Chapter 6 Microstructure analysis in HAZ

When deformed materials are annealed, recovery, recrystallisation and grain growth occur. In the HAZ, the peak temperature is high enough to activate these annealing phenomena, so it is possible that recovery, recrystallisation, and grain growth would occur in sequence, from base metal to fusion boundary. However, the temperature varies sharply in the HAZ (it takes a few second to reach the peak temperature in the HAZ), some annealing phenomena could be restrained.

Fig. 6.1 is the hardness testing results from the fusion zone towards the unaffected metal of W8. The hardness was tested from the fusion boundary (FD) to the base metal at the step of 0.32mm. The curve can be divided into three parts: 1. 0~-2.5 mm, 2. -3.2 ~-2.5 mm, and 3. <-3.2 mm. In the first part, the hardness trend has a “v” shape, and the lowest value is about 72.5 Hv. In the second part, the hardness changes abruptly. In the third part, the hardness changes with a gentle slope.

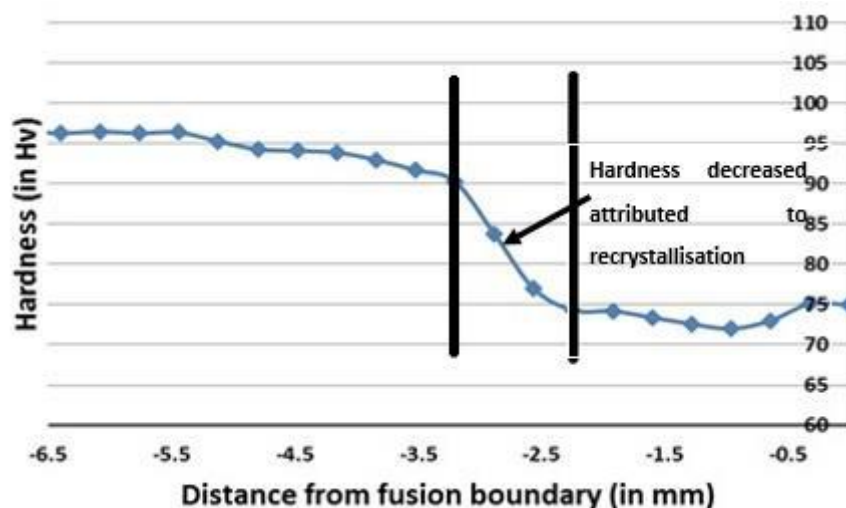


Fig. 6.1 The relationship between hardness and distance from fusion boundary (DFB)

## 6.1 Recrystallisation in the HAZ

The microstructure of weldment revealed by anodising is shown in Fig. 6. 2. It could easily be distinguished that, in frame 7 of Fig. 6.2, the microstructure changes sharply. The distance of the frame 7 in Fig. 6.2 to the fusion boundary corresponds to the distance of the second part of the hardness results in Fig. 6.1. Because of the obvious microstructure change, the phenomenon of between -3.2 to -2.5 mm in weldment can be classified as recrystallisation. However, the technique of anodisation is weak in characterising the microstructure of deformed materials, so it is difficult to provide more details about the phenomenon occurring from -3.2 mm to the unaffected zone of the weldment.

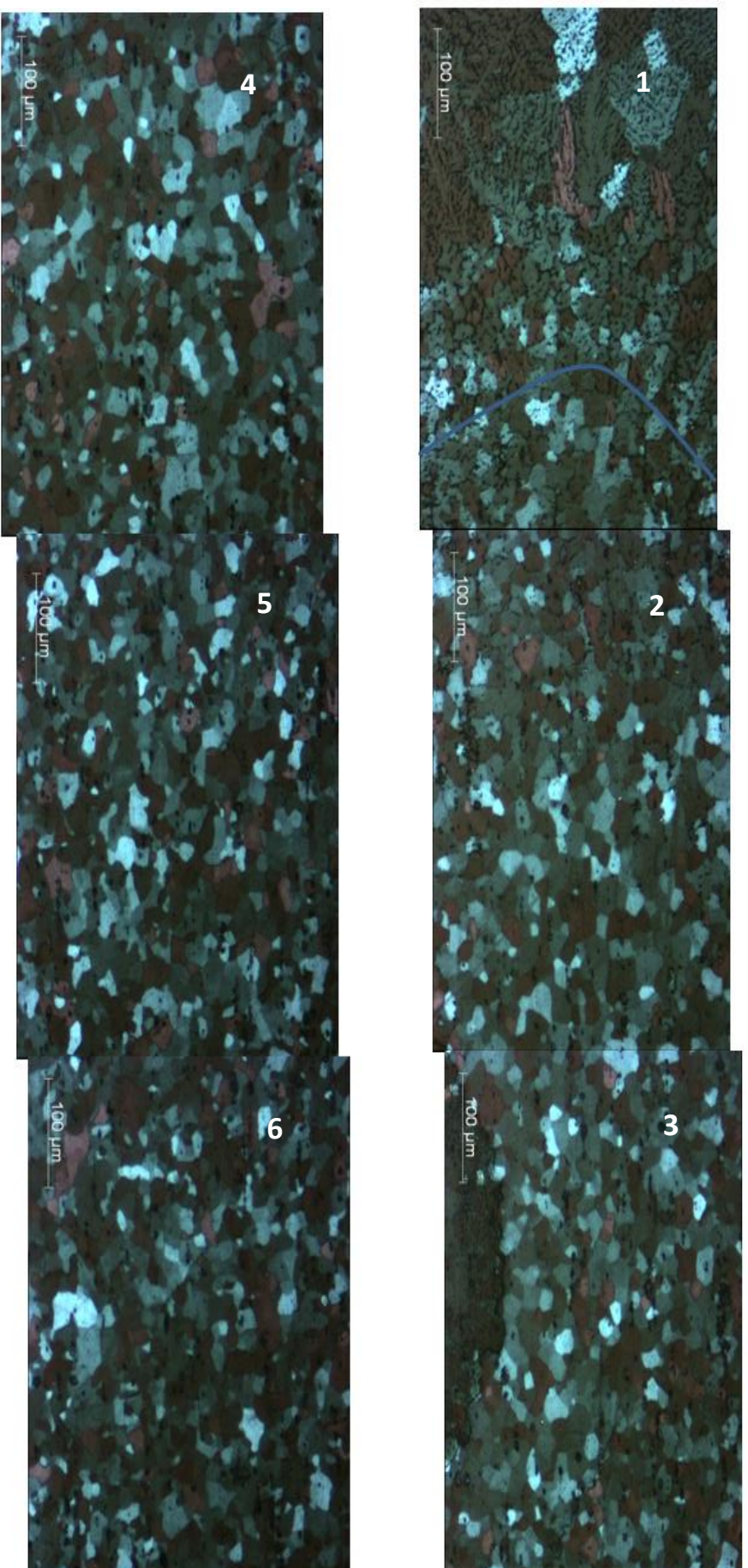


Fig. 6.2 (Fram1 to 6) Microstructure of W8 from fusion boundary to unaffected zone (blue curve is the fusion



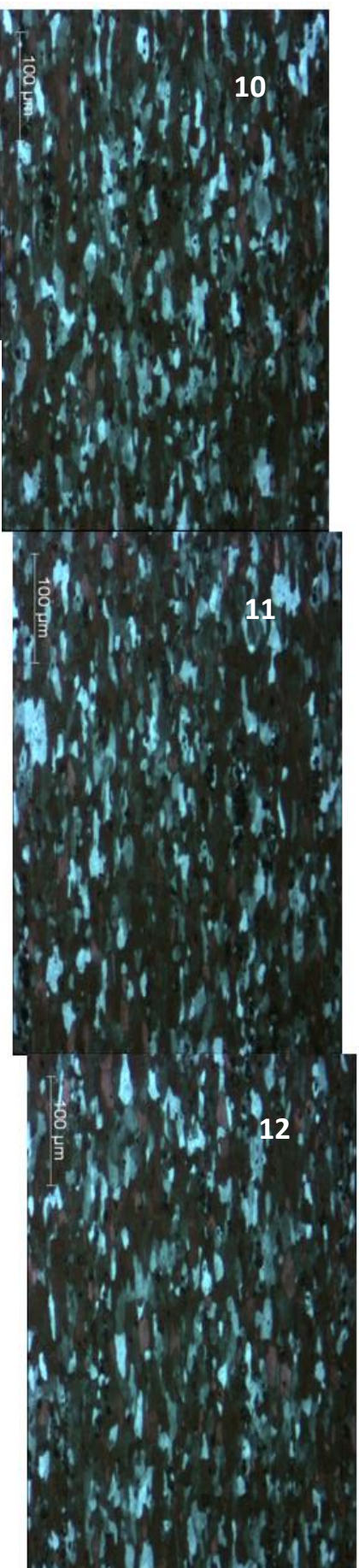
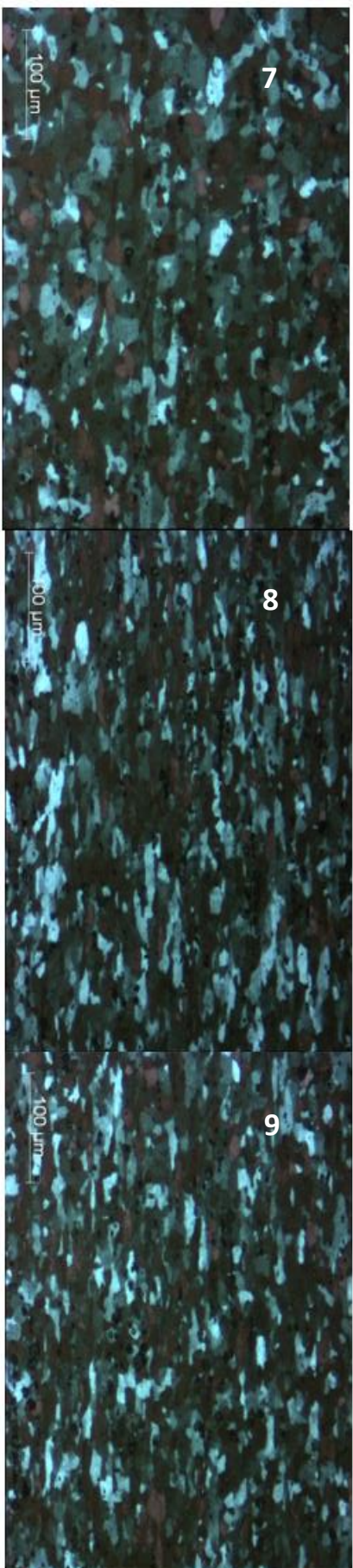


Fig. 6.2 (Fram7 to 12) Microstructure of W8 from fusion boundary to unaffected

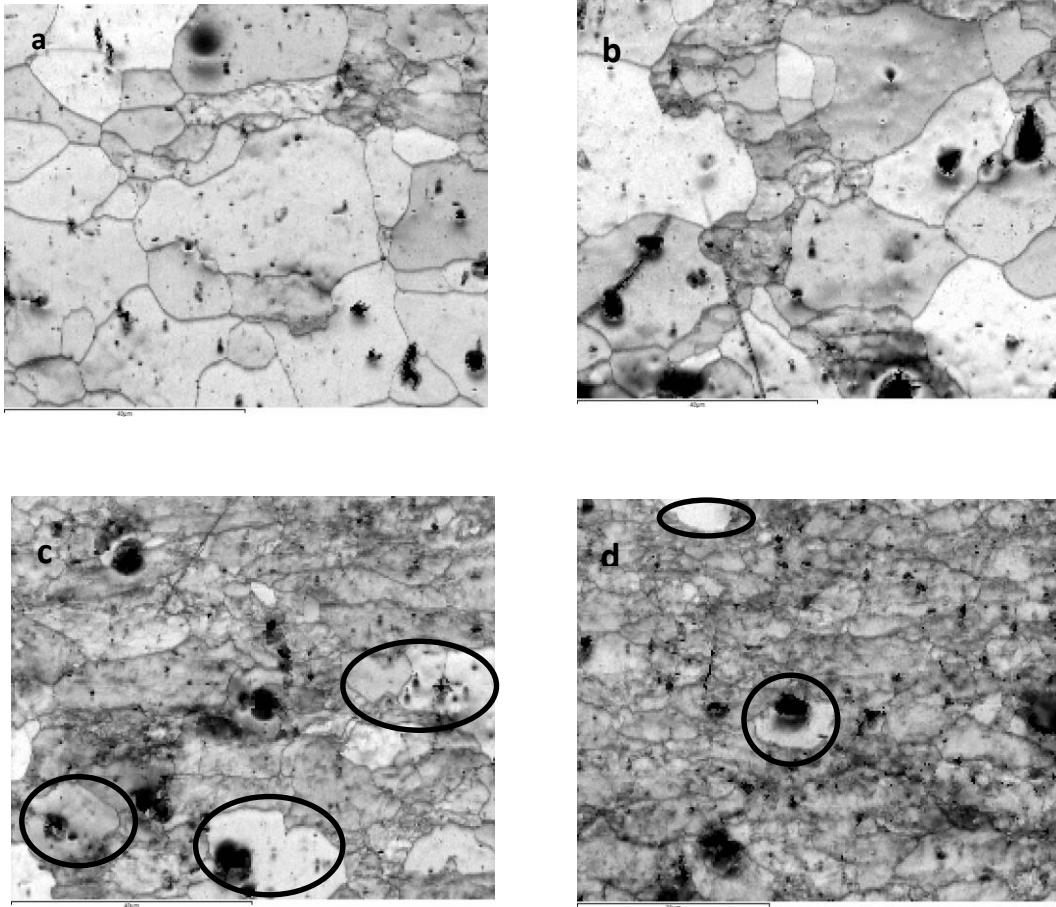


Fig. 6.3 Quality image of EBSD at different distances from fusion boundary, a. -2.5 mm, b. -2.88mm, c. -3.2 mm and d -3.6mm

Fig. 6.3 shows the quality image of the EBSD. Four testing regions were taken at positions: -2.3, -2.88, -3.2 and -3.6mm to the fusion boundary. Most of the grains shown in Fig.6.3-a and -b are recrystallised, and have sharp inverse pole figure points, shown in Fig.6.4-a and Fig.6.4-b. The phenomenon of recrystallisation occurring in the range of DFB of -2.7 to 2.5 mm was confirmed. Fig.3-c was captured at the DFB of -3.2 mm, and the hardness at the same DFB was about 91 Hv, which is the transition point from the second part to the third part in Fig.6.1. In Fig.6.3-c, a few recrystallised grains appear, which have Inverse pole figure points in Fig.6.4-c. Fig.6.3-d was taken at the

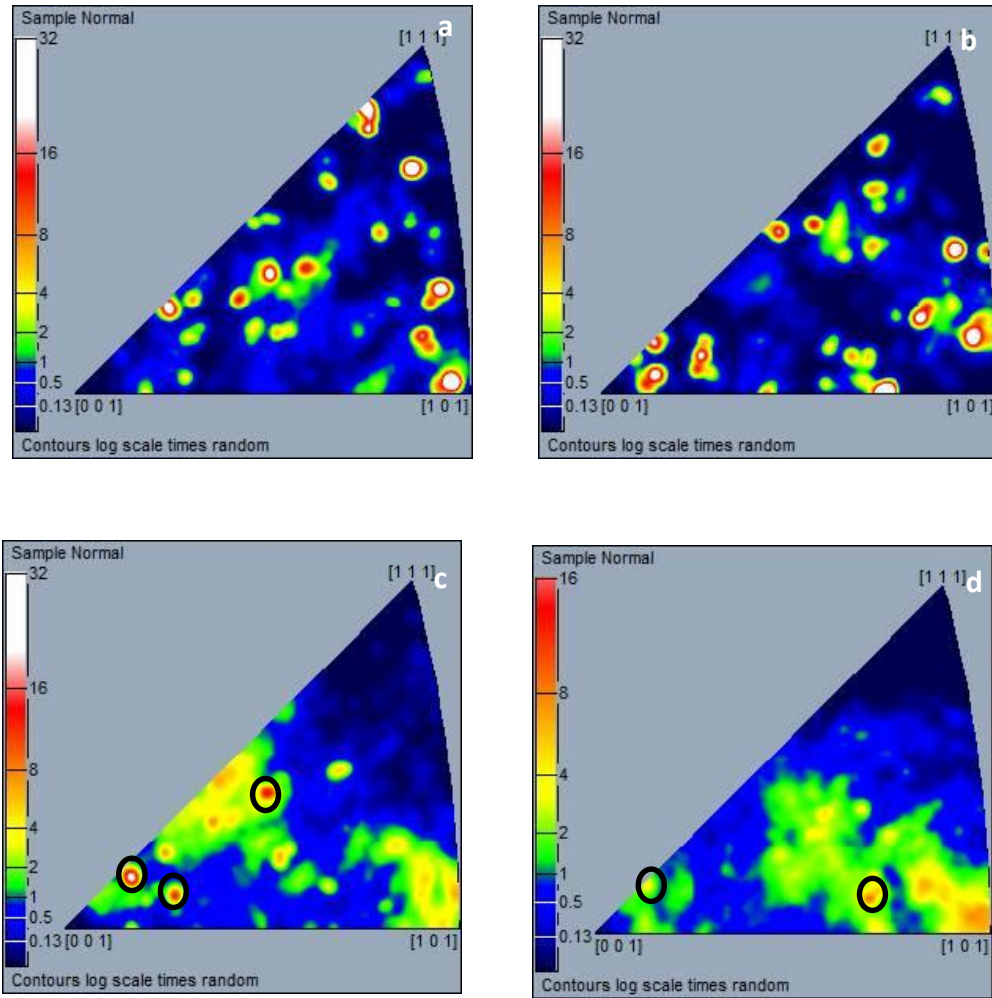


Fig. 6.4 Inverse pole figure of EBSD at different distances from fusion boundary, a. - 2.5 mm, b. -2.88mm, c. -3.2 mm and d -3.52 (black circled areas are the inverse pole figure points corresponding to the circled grains in Fig. 6.3)

DFB of -3.6mm and the hardness at this point is about 94 Hv. Fig. 6.3-d shows that the recrystallisation starts and there are few recrystallised grains growing around the second phase particles. Combining the results of previous chapters, it may be concluded that the gentle hardness change in the third part in Fig. 6.1 was caused by recrystallisation. The reason why the hardness changes gentle is that few nuclei are activated with the increase in DFB.

## 6.2 Grain growth

Grain size was measured by EBSD at three regions, as shown in Fig. 6.5. Table 6.1 shows that the average grain size in the region C was near to the average grain size of the sample heat-treated for 1 hour at 350 °C (shown in Table 5.3).

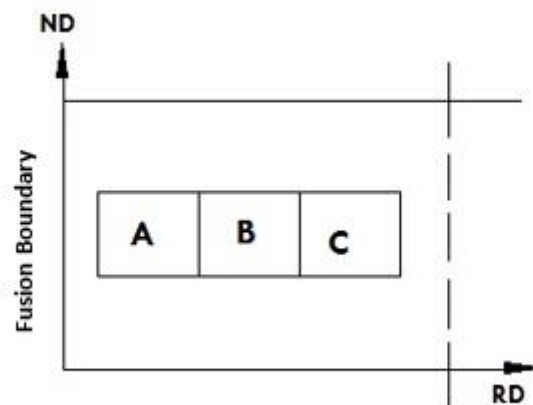


Fig. 6.5 Regions for the grain size measured by EBSD

Table 6.1 Grain size at different regions from the fusion boundary

Regions	ECD (μm)
A	17.5
B	17.2
C	16.2

According to the Hall-Patch equation, the strength decrease is:

$$\Delta\sigma_y = \frac{k_y}{\sqrt{d}} \quad \text{Equation 6.1}$$

$K_y$  was taken as 0.3 [1], and the strength decrease caused by grain growth was about 0.1 MPa. The strength has an empirical relationship with hardness, which is  $\sigma_y =$



$3Hv$  , so the hardness decrease caused by the grain growth was about 0.03 Hv which was much lower than that of the standard deviation of hardness testing.

It may be concluded that the hardness decrease in the range from -2.24 to -0.96 mm of DFB was still caused by recrystallisation. It is the same as the isothermal recrystallisation phenomenon as, when the transformation nearly complete, the kinetic will decrease. The hardness increased from -0.96 to 0 of DFB, caused by the dissolution of second phase particles.

### 6.3 Summary

The microstructure of the weldment 8 was studied by OM and EBSD from the fusion boundary to an un-affected-zone. The hardness decrease in HAZ was mainly caused by recrystallisation. Grain growth has little effect on the hardness decrease after recrystallisation. The hardness increased when the testing point was near to the fusion boundary. A possible reason was the dissolution of second phase particles when the peak temperature near to the fusion boundary exceeded the dissolution temperature.

## Chapter 7 Thermal profile modelling

In order to model the microstructure of a weldment, it is important to model the thermal profile in the weldment during welding. The accuracy of the prediction of the thermal profile will affect the results of the microstructure modelling. Currently, the methods modelling of thermal profile are classified into two groups: analytical and numerical. Both of these two methods will be compared in this chapter.

### 7.1 Analytical method

In analytical methods, the heat source is assumed to be point or line, which is dependent on the penetration of the welding. If the welded plate can be fully penetrated, the line heat source will be applied; if the plate is not penetrated, the point heat source will be applied.

In the current project, the thickness of the plate is only 1.6 mm and 2 mm, and during the welding, the welded sheets were penetrated, so the line heat source is applied in the analytical calculation.

The Green function of the thermal diffusion PDF with the line heat source is:

$$T - T_0 = \frac{q_0}{2\pi\lambda} \exp\left(-\frac{vx'}{2a}\right) K_0\left(\frac{vr}{2a}\right) \quad \text{Equation 7.1 [76]}$$

Where the  $r$  is the distance from the interested point -Q to the heat source-P (shown in Fig.2.8),  $d$  is the thickness of the welded plate,  $T_0$  is the room temperature,  $q_0$  is the net energy input, and  $\lambda$  is the thermal conductivity.

Christensen used a set of dimensionless symbols to simplify the original Rosenthal equations[77]. There are three parts to the Christensen's simplification:

1. dimensionless temperature

$$\theta = (T - T_0)/(T_m - T_0) \quad \text{Equation 7.2}$$

where  $T_m$  is another reference temperature, normally taken as the melting point;

2. dimensionless operating parameter

$$n = \frac{Qv}{4\pi a^2 \rho c((T_m - T_0))} \quad \text{Equation 7.3}$$

3. dimensionless coordinates and radius vector

$$\xi = vx'/2a \quad \text{Equation 7.3.a}$$

$$\psi = vy/2a \quad \text{Equation 7.3.b}$$

$$\phi = vz/2a \quad \text{Equation 7.3.c}$$

$$\sigma_r = vR/2a \quad \text{Equation 7.3.d}$$

The dimensionless equation is:

$$\theta = \frac{ne^{-\xi}K_0(\sigma_r)}{\delta} \quad \text{Equation 7.4}$$

The width of the fusion zone is:

$$\psi_m = 2\sigma_r \sqrt{1 - \frac{[K_0(\sigma_r)]^2}{[K_1(\sigma_r)]^2}} \quad \text{Equation 7.5}$$

Where  $K_0(\sigma_r)$  is the modified Bessel function of the second kind and zero order, and

$K_1(\sigma_r)$  is the modified Bessel function of the second kind and first order.

$q$  and  $Qv$  are the same, which represent the net heat input energy.

$$q = Q * \eta \quad \text{Equation 7.6}$$

Where  $Q$  is the gross energy input ( $Q = I * U$ ), and  $\eta$  is the efficiency of the heat source.

For the analytical method, the efficiency is a very important input parameter which can affect the results of the temperature field. The efficiencies of MIG welding ranges from 0.65 to 0.85 [77, 93, 94]. In Lu and Kou's experimental work [93], aluminum plates and filler were used, and the welding process is similar to the welding process applied in this project. So, the results of Lu and Kou are more valuable. Fig. 7.1 is the re-plotted figure of Lu and Kou's results[93]. In the current modeling work, efficiencies are taken from 0.65 to 0.85 in steps of 0.5.

#### 7.1.1 Input parameters for the analytical method

The welding parameters of W6 are shown in Table 7.1. For the analytical method, the thermal properties of material are assumed to be constants and taken from the literature [95], the thermal conductivity and specific heat capacity Al-Mg alloys are 149 W/mm\*K and  $2.7 \times 10^6$  J/m<sup>3</sup>\*K.

Table 7.1 The welding parameters of AA5251 H34- W8

	Wire feed rate	Weldin -g speed	Arc tim -e	Averag -e voltage	Averag -e current	Net power	Heat input	Filler diameter -r
	m/mi n	m/min	s	V	A	W	kJ/m m	mm
AA5251 -W8	6.0	0.9	30	19.0	111	1669. 5	0.14	1.2

### 7.1.2 Results of the analytical method

All calculations were carried out using Matlab software. The thermal field of the pseudo-steady state changed with efficiency. Fig. 7.1 shows the type thermal field result.

The temperature at the heat source is infinitely large and there is a region that the average temperature is above 3000 K. Normally, the maximum temperature in the fusion zone is 500 K larger than the melting point of the work piece [96]. Because of the over-simplified assumption of the heat source, the analytical method cannot accurately predict the temperature of the fusion zone.

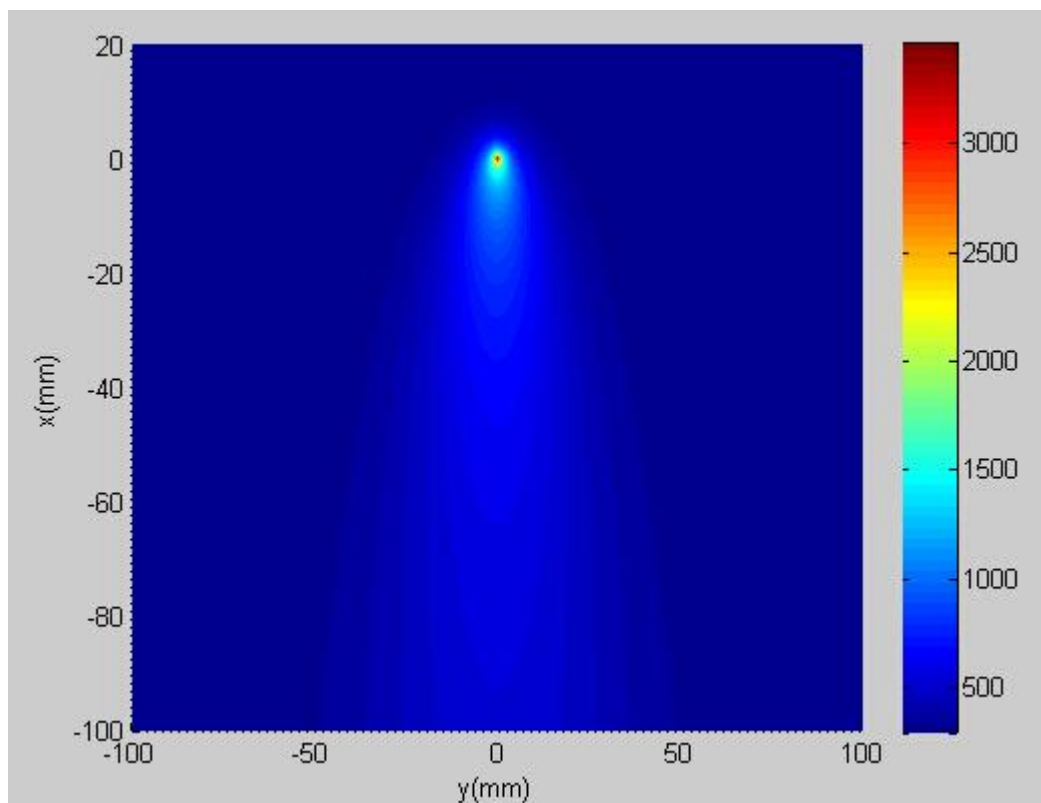


Fig. 7.1 The temperature field of AA5251 W8 with an efficiency of 0.82

The cross-section of W8 is shown in Fig. 7.2. Except for the enforcement layer, the top width of the fusion zone is around 5.7 mm, the bottom width of the fusion zone is only 2.0 mm, and the area of the cross-section is about 7.7 mm<sup>2</sup>. Table 7.2 shows the widths of the fusion zone with different efficiencies. There is a big difference between the predicted results and the experimental results. Even with the lowest efficiency, the area of cross-section is 17.4 mm<sup>2</sup>.

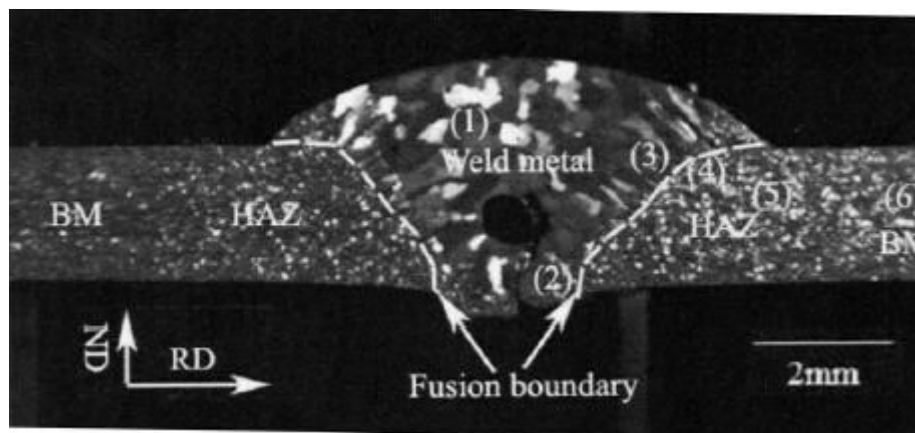


Fig. 7.2 Cross-section of weldment 5 [82]

Table 7.2 Widths of the fusion zone with different efficiencies

Efficiencies	Width of fusion zone (mm)
0.65	6.8
0.70	8.9
0.78	9.0
0.79	9.2
0.80	9.4
0.81	9.5
0.82	9.7

Fig. 7.3 shows the predicted peak temperature distribution along the HAZ. In previous research [82], there are 4 points away from the fusion boundary, of which the thermal profile has been measured (the peak temperature is shown in Table 7.3) [82]. Comparing the experimental results with predicted results, when the efficiency is 0.65, the temperature of 0.5 mm can fit well; but for temperatures further from the fusion boundary, higher efficiency is required so the analytical method is also weak at predicting the temperature distribution in HAZ.

Table 7.3 Peak temperature at different points from the fusion boundary [82]

Distance from the fusion boundary (mm)	Experimental peak temperature (in °C)
0.5	592
2.0	524
2.9	480
4.3	429

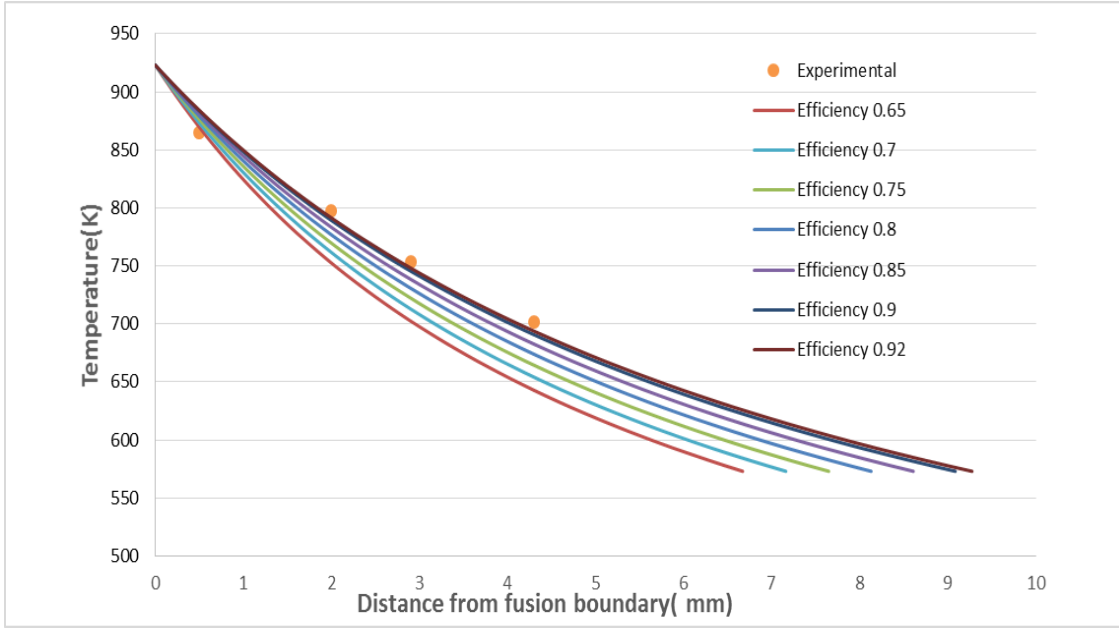


Fig. 7.3 Predicted peak temperature distribution in the HAZ with different efficiencies

## 7.2 Numerical model method

### 7.2.1 The process of building the numerical model

The software Comsol 4.4 was used to model the thermal profile during the welding.

The process modelling is shown in Fig. 7.4. The geometry was built on a simplified weldment (Fig. 7.5). The Gaussian heat source  $Q$  will be used:

$$Q(x, y) = \frac{Q}{2\pi\sigma^2} * \exp\left(-\frac{x^2+y^2}{2\sigma^2}\right) \quad \text{Equation 7.7 [78]}$$

where  $\sigma$  is the characteristic radius of the flux distribution and  $Q$  is the net energy input.

$$Q = \eta * U * I \quad \text{Equation 7.8}$$

where  $U$  and  $I$  are the welding voltage and current, respectively, and  $\eta$  is the efficiency of arc. The material thermal properties were taken from literature with similar material compositions [97].



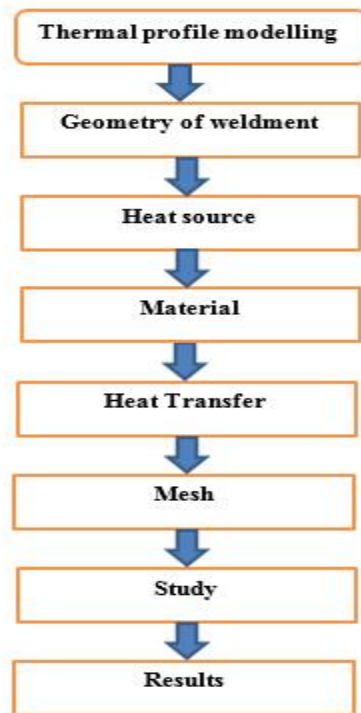


Fig. 7.4 The thermal modelling flow chart

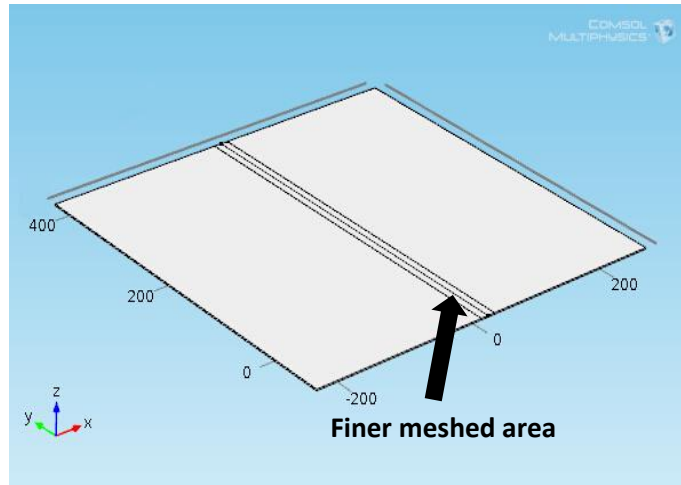


Fig. 7.5 The geometry of modelled weldment

The heat transfer was used to set the boundary conditions. Except for the welding surface, other surfaces were set as thermal insulation. The welding surface was treated as a surface with radiation effect. To optimise the meshing, the weldment was divided

into two areas. A finer mesh was used in the area near to the central welding line, and a fine mesh was applied in the other weldment. The time dependent study method was chosen.

For this thermal model, there are two input parameters which could be adjusted to obtain more accurate results compared with the experimental results; one is efficiency and the other is the radius of the flux distribution. The parameters sweep was used in the thermal model. The radius of the flux distribution ranged from 2mm to 5mm, and the efficiency ranged from 0.30 to 0.80.

### 7.2.2 Results of the numerical model

The larger flux distribution radius and lower efficiency would result in unpenetrated model welding, while smaller and higher efficiency would have a wider fusion zone, which would be much larger than that of the experimental results. For W8 (shown in Fig. 7.2), the cross-section of the fusion zone along the welding direction had an inverted trapezoidal shape: the upper width is 5.7 mm and the lower width is 2.0 mm. Table 7.4 shows parts of the results with different pair efficiencies and radius of flux distributions. To fit the experimental fusion zone, the refined ranges for efficiency and radius of the flux distribution are from 0.5 to 0.6 and from 4.5 to 5mm, respectively. The optimal results which give the best fitting to the experimental fusion zone are 0.53 and 4.9mm for efficiency and the radius, respectively.

Table 7.4 Upper width and lower width with different pairs of efficiencies and radius of flux distributions (in mm)

Efficiency Radius	0.3	0.4	0.5	0.6	0.7	0.8
2.5	▼	▼	5.0/4.3	6.3/5.4	7.1/6.7	7.7/7.4
3	▼	▼	5.0/3.7	6.5/5.3	7.3/6.6	7.9/7.4
3.5	▼	▼	5.0/3.5	6.5/5.2	7.5/6.5	8.0/7.4
4	▼	▼	5.1/2.8	6.6/5.0	7.5/6.4	8.2/7.4
4.5	▼	▼	4.9/1.6	6.6/4.7	7.5/6.3	8.5/7.5
5	▼	▼	▼	6.5/4.4	7.6/6.2	8.5/7.4

(‘▼’ means that the welded sheets have not been penetrated)

The peak temperatures of the model fits well with the experimental data (as shown in Table 7.5); there is only a 2.6% difference at the first observing point and a 2.1% difference at the fourth point.

Table 7.5 Comparison between the experimental results with modeled results

Distance from the fusion boundary (mm)	Experimental peak temperature (in °C)	Results of the thermal model (in °C)
0.5	592	606
2.0	524	535
2.9	480	487
4.3	429	420

The numerical method is successful in predicting the size of the fusion zone and the peak temperature in the HAZ. It should be noticed that the efficiency employed in the thermal model was lower than the suggested value (0.8) in the literature. In MIG

welding (Fig. 7.6), there were clamps and stainless steel under the fusion zone to fix the welded sheets. During welding, heat would be absorbed by the clamps and backing stainless steel bar, and this is attributed to the efficiency reduction from 0.8 to 0.53.

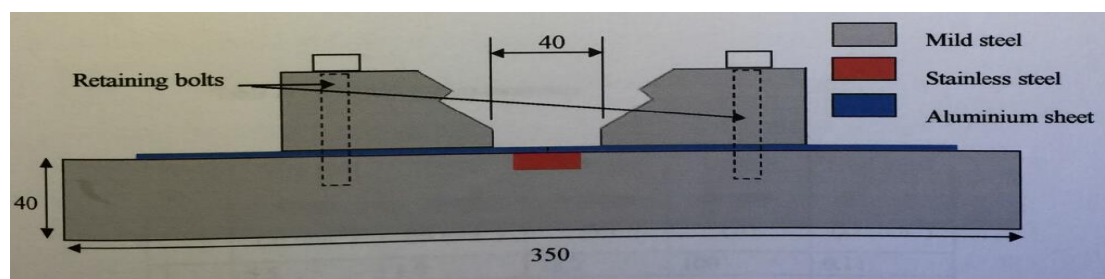


Fig. 7.6 Schematic cross-section of the MIG welding set-up [98]

### 7.3 Summary

The analytical method and numerical method were implemented to model the temperature distribution in the HAZ. The simplified line heat source was used in the analytical method, and the results of the analytical method can predict neither the size of the fusion zone nor the peak temperature at different observation points in the HAZ. Compared with the analytical method, a numerical method based on the Comsol software was found to fit well with the experimental fusion zone through adjusting the efficiency and the radius of the flux distribution. The predicted peak temperatures could fit well with the experimental results. The lower efficiency input in the numerical model was caused by the heat sunk by the clamps and backing stainless steel bar during the welding. The reduction in efficiency could be determined by modelling through comparing the modelled fusion zone size with the experimental result.

## Chapter 8 Conclusions and future work

### 8.1 Conclusions

The present work is mainly about the study of the annealing phenomena of AA5083 H22 sheet for the isothermal heat treatment and microstructure changes in the heat-affected zone (HAZ), and the prediction of thermal profiles in the HAZ has been carried out. The main conclusions are as follows:

Recrystallisation played the most important part during annealing. In the DSC test, there is only one major exothermic peak which corresponds to recrystallisation. The activation energy showed a liner relationship with the fraction of recrystallisation and increased from 126 kJ/mol to 150 kJ/mol. The Avrami exponent for the kinetic JMAK equation has a transit point, and the exponent changed from around 0.9 to 1.9 through the transit point. The Avrami exponent transit point showed that the mechanism of recrystallisation is different from the nucleation of recrystallisation to grain growth of recrystallisation. For future modelling work, the activation energy variation and the transit point Avrami exponent of recrystallisation could be considered.

In the heat affected zone (HAZ), the hardness decrease was mainly caused by recrystallisation. The average grain size only increased by 1.3  $\mu\text{m}$  from the full recrystallisation region to the region near to the fusion boundary, which has little effect on the hardness decrease. The hardness increased near to the fusion boundary, which could be attributed to the dissolution of the second phase particles.

The input efficiency for the thermal modelling is lower than the value suggested in the literature. This was attributed to the heat sunk by the clamps and backing bar under the fusion zone during the welding process. The numerical method using Comsol software could predict the thermal profiles which fit well with the experimental data. All phenomena occurring in the HAZ are linked to the thermal activated process, so the correct thermal would determine the accuracy of the future model.

## 8.2 Future work

The present work has provided activation energy and the Avrami exponent, as input parameters for the isothermal annealing softening kinetic model and studied the microstructure and hardness evolution in the HAZ of AA5083 H22 W8. Future work might concentrate on building a non-isothermal kinetic model to predict the hardness distribution in HAZ.

It would also be possible to study the relationship between the isothermal and non-isothermal softening kinetic and obtain confirmed non-isothermal softening kinetic model to predict the hardness in HAZ (excluding the hardness increase near to the fusion boundary).

Another area of future research would be to study the second phase particles (Fe-rich and Mg-rich particles), dissolution kinetic and effect on the properties in the region of HAZ near to the fusion boundary. After the dissolution kinetic has been determined, it could be combined with the softening kinetic model to predict the hardness distribution from the fusion boundary to the heat un-affected zone.

Another fruitful area would be to validate the model through different welding trials.

## Reference

1. Polmear, I.J., ed. *Light Alloys*. 2006, Butterworth-Heinemann.
2. Hatch, J.E., A. Association, and A.S. Metals, *Aluminum: Properties and Physical Metallurgy*. 1984: American Society for Metals.
3. Mondolfo, L.F., *Aluminum alloys: structure and properties*. 1976: Butterworths.
4. Yu, X.F., Y.M. Zhao, X.Y. Wen, and T. Zhai, A study of mechanical isotropy of continuous cast and direct chill cast AA5182 Al alloys. *Materials Science and Engineering: A*, 2005. 394(1–2): p. 376-384.
5. Zhao, Y.M., W. Wen, and J.G. Morris, The differences in particle structures and recrystallization behaviors between DC and CC AA5052 aluminum alloys. *Materials Science and Engineering*, 2004. A373: p. 167-174.
6. Slámová M., M. Karlík, F. Robaut, P. Sláma, and M. Věron, Differences in microstructure and texture of Al-Mg sheets produced by twin-roll continuous casting and by direct-chill casting. *Materials Characterization*, 2002. 49(3): p. 231-240.
7. Krstić Vukelja, E., I. Duplančić, and B. Lela, CONTINUOUS ROLL CASTING OF ALUMINIUM ALLOYS--CASTING PARAMETERS ANALYSIS. *Metalurgija*, 2010. 49(2).
8. Liu, J. and J.G. Morris, Recrystallization microstructures and textures in AA 5052 continuous cast and direct chill cast aluminum alloy. *Materials Science and Engineering: A*, 2004. 385(1–2): p. 342-351.
9. Liu, J. and J.G. Morris, Macro-, micro- and mesotexture evolutions of continuous cast and direct chill cast AA 3105 aluminum alloy during cold rolling. *Materials Science and Engineering: A*, 2003. 357(1–2): p. 277-296.
10. Liu, W.C. and J.G. Morris, Effect of pre-treatment on recrystallization and recrystallization textures of cold rolled CC AA 5182 aluminum alloy. *Materials Science and Engineering: A*, 2003. 363(1–2): p. 253-262.
11. Liu, W.C., T. Zhai, and J.G. Morris, Comparison of recrystallization and recrystallization textures in cold-rolled DC and CC AA 5182 aluminum alloys. *Materials Science and Engineering: A*, 2003. 358(1–2): p. 84-93.
12. Engler, O., Influence of particle stimulated nucleation on the recrystallization textures in cold deformed Al-alloys Part II—Modeling of recrystallization textures. *Scripta Materialia*, 1997. 37(11): p. 1675-1683.
13. Flood, S.C., Influence of extreme variations in casting parameters and iron & silicon compositions on can-end stock (AA-5182). *Light Metals*, 1995. TMS Warrendale: p. 1127-1135.
14. Zhao, Y.M., W.C. Liu, and J.G. Morris, Quantitative analysis of texture evolution of cold-rolled direct-chill-cast and continuous-cast AA5052 and AA5182 aluminum alloys during isothermal annealing. *Metallurgical and Materials Transactions A*, 2004. 35(11): p. 3613-3629.



15. Li, Y.J. and L. Arnberg, A eutectoid phase transformation for the primary intermetallic particle from Alm(Fe,Mn) to Al<sub>3</sub>(Fe,Mn) in AA5182 alloy. *Acta Materialia*, 2004. 52(10): p. 2945-2952.
16. Vetrano, J.S., S.M. Bruemmer, L.M. Pawlowski, and I.M. Robertson, Influence of the particle size on recrystallization and grain growth in Al-Mg-X alloys. *Materials Science and Engineering*, 1997. A238: p. 101-107.
17. Kaufman, J.G., *Introduction to aluminum alloys and tempers*. 2000: ASM International.
18. <http://www.aalco.co.uk/literature/>.
19. Humphreys, F. and M. Hatherly, *Recrystallization and related annealing phenomena*. 2004: Elsevier.
20. Ashby, M.F., The deformation of plastically non-homogeneous materials. *Philosophical Magazine*, 1970. 21(170): p. 399-424.
21. Rollett, A.D. and U. Kocks, A review of the stages of work hardening. *Solid State Phenomena*, 1993. 35: p. 1-18.
22. Ryen, Ø., H. Laukli, B. Holmedal, and E. Nes, Large strain work hardening of aluminum alloys and the effect of mg in solid solution. *Metallurgical and Materials Transactions A*, 2006. 37(6): p. 2007-2013.
23. Marthinsen, K. and E. Nes, Modelling strain hardening and steady state deformation of Al-Mg alloys. *Materials science and technology*, 2001. 17(4): p. 376-388.
24. Cottrell, A.H. and B.A. Bilby, Dislocation Theory of Yielding and Strain Ageing of Iron. *Proceedings of the Physical Society. Section A*, 1949. 62(1): p. 49.
25. Haasen, P., Chapter 23 - Mechanical Properties of Solid Solutions, in *Physical Metallurgy (Fourth Edition)*, R.W. Cahn and P. Haasen, Editors. 1996, North-Holland: Oxford. p. 2009-2073.
26. Ryen, Ø., B. Holmedal, O. Nijs, E. Nes, E. Sjølander, and H.-E. Ekström, Strengthening mechanisms in solid solution aluminum alloys. *Metallurgical and Materials Transactions A*, 2006. 37(6): p. 1999-2006.
27. Hall, E., The deformation and ageing of mild steel: III discussion of results. *Proceedings of the Physical Society. Section B*, 1951. 64(9): p. 747.
28. Hertzberg, R.W., ed. *Deformation and Fracture Mechanics of Engineering Materials*. 4 ed. 1995, John Wiley & Sons Inc.
29. Hansen, N., The effect of grain size and strain on the tensile flow stress of aluminium at room temperature. *Acta Metallurgica*, 1977. 25(8): p. 863-869.
30. Lloyd, D., Deformation of fine-grained aluminium alloys. *Metal Science*, 1980. 14(5): p. 193-198.
31. Cotterill, P. and P.R. Mould, *Recrystallization and Grain Growth in Metals*. 1976: Surrey University Press.
32. Humphreys, F.J. and M. Hatherly, eds. *Recrystallization and Related Annealing Phenomena*. 2004, ELSEVIER Ltd: Oxford.
33. Martin, J.W., R.D. Doherty, and B. Cantor, eds. *Stability of microstructure in metallic systems*. 1997, Cambridge University Press: Cambridge.

34. Nes, E., Recovery revisited. *Acta Metallurgica et Materialia*, 1995. 43(6): p. 2189-2207.
35. Bate, P.S., R.D. Knutsen, I. Brough, and F.J. Humphreys, The characterization of low-angle boundaries by EBSD. *Journal of Microscopy*, 2005. 220(1): p. 36-46.
36. Doherty, R.D., D.A. Hughes, F.J. Humphreys, J.J. Jonas, D.J. Jensen, M.E. Kassner, W.E. King, T.R. McNelley, H.J. McQueen, and A.D. Rollett, Current issues in recrystallization: a review. *Materials Science and Engineering: A*, 1997. 238(2): p. 219-274.
37. Doherty, R.D., Chapter 15 - Diffusive Phase Transformations in the Solid State, in *Physical Metallurgy (Fourth Edition)*, R.W. Cahn and P. Haasen, Editors. 1996, North-Holland: Oxford. p. 1363-1505.
38. Christian, J.W., Chapter 3 - The Theory of Reaction Rates, in *The Theory of Transformations in Metals and Alloys*, J.W. Christian, Editor. 2002, Pergamon: Oxford. p. 79-94.
39. Christian, J.W., Chapter 19 - Recovery, Recrystallization and Grain Growth, in *The Theory of Transformations in Metals and Alloys*, J.W. Christian, Editor. 2002, Pergamon: Oxford. p. 832-858.
40. Hansen, N. and R.F. Mehl, New discoveries in deformed metals. *Metallurgical and materials transactions A*, 2001. 32(12): p. 2917-2935.
41. Humphreys, F.J., The nucleation of recrystallization at second phase particles in deformed aluminium. *Acta Metallurgica*, 1977. 25(11): p. 1323-1344.
42. Eivani, A.R., J. Zhou, and J. Duszczek, Simulation of transient-state recrystallization of Al-4.5Mg-1Zn alloy after hot deformation. *Computational Materials Science*, 2014. 86(0): p. 193-199.
43. Liu, W.C., J. Li, H. Yuan, and Q.X. Yang, Effect of recovery on the recrystallization texture of an Al-Mg alloy. *Scripta Materialia*, 2007. 57(9): p. 833-836.
44. Huang, Y. and F.J. Humphreys, Subgrain growth and low angle boundary mobility in aluminium crystals of orientation  $\{110\} \langle 001 \rangle$ . *Acta Materialia*, 2000. 48(8): p. 2017-2030.
45. Cahn, R.W., Chapter 28 - Recovery and Recrystallization, in *Physical Metallurgy (Fourth Edition)*, R.W. Cahn and P. Haasen, Editors. 1996, North-Holland: Oxford. p. 2399-2500.
46. Randle, V. and O. Engler, *Introduction to texture analysis: microtexture, microtexture and orientation mapping*. 2000: CRC Press.
47. Cabibbo, M., E. Evangelista, and C. Scalabroni, EBSD FEG-SEM, TEM and XRD techniques applied to grain study of a commercially pure 1200 aluminum subjected to equal-channel angular-pressing. *Micron*, 2005. 36(5): p. 401-414.
48. Humphreys, F.J., Quantitative metallography by electron backscattered diffraction. *Journal of Microscopy*, 1999. 195(3): p. 170-185.
49. Humphreys, F., Review grain and subgrain characterisation by electron backscatter diffraction. *Journal of materials science*, 2001. 36(16): p. 3833-3854.

50. Gundlach, C., W. Pantleon, E.M. Lauridsen, L. Margulies, R.D. Doherty, and H.F. Poulsen, Direct observation of subgrain evolution during recovery of cold-rolled aluminium. *Scripta Materialia*, 2004. 50(4): p. 477-481.
51. Lauridsen, E.M., D.J. Jensen, H.F. Poulsen, and U. Lienert, Kinetics of individual grains during recrystallization. *Scripta Materialia*, 2000. 43(6): p. 561-566.
52. Lauridsen, E.M., H.F. Poulsen, S.F. Nielsen, and D. Juul Jensen, Recrystallization kinetics of individual bulk grains in 90% cold-rolled aluminium. *Acta Materialia*, 2003. 51(15): p. 4423-4435.
53. Poulsen, H.F., E.M. Lauridsen, S. Schmidt, L. Margulies, and J.H. Driver, 3D-characterisation of microstructure evolution during annealing of a deformed aluminum single crystal. *Acta Materialia*, 2003. 51(9): p. 2517-2529.
54. Hirsch, J. and K. Lücke, Overview no. 76: Mechanism of deformation and development of rolling textures in polycrystalline f.c.c. metals—I. Description of rolling texture development in homogeneous CuZn alloys. *Acta Metallurgica*, 1988. 36(11): p. 2863-2882.
55. Helbert, A.-L., W. Wang, F. Brisset, T. Baudin, and R. Penelle, In Situ EBSD Investigation of Recrystallization in a Partially Annealed and Cold-Rolled Aluminum Alloy of Commercial Purity. *Advanced Engineering Materials*, 2012. 14(1-2): p. 39-44.
56. Chang, C.S.T. and B.J. Duggan, Relationships between rolled grain shape, deformation bands, microstructures and recrystallization textures in Al-5%Mg. *Acta Materialia*, 2010. 58(2): p. 476-489.
57. Liu, J., S. Banovic, F. Biancaniello, and R. Jiggetts, Through-thickness texture gradient in an annealed Al-Mg Alloy sheet. *Metallurgical and Materials Transactions A*, 2005. 36(3): p. 869-874.
58. Dillamore, I. and H. Katoh, The mechanisms of recrystallization in cubic metals with particular reference to their orientation-dependence. *Metal Science*, 1974. 8(1): p. 73-83.
59. Vatne, H.E., R. Shahani, and E. Nes, Deformation of cube-oriented grains and formation of recrystallized cube grains in a hot deformed commercial AlMgMn aluminium alloy. *Acta Materialia*, 1996. 44(11): p. 4447-4462.
60. Higginson, R.L., M. Aindow, and P.S. Bate, The effect of finely dispersed particles on primary recrystallisation textures in AlMnSi alloys. *Materials Science and Engineering: A*, 1997. 225(1-2): p. 9-21.
61. Attallah, M.M., Microstructure-property development in friction stir welds of aluminium-based alloys, Ph.D. Metallurgy and Materials School of Engineering. 2007 University of Birmingham, Birmingham
62. Patinet, S. and L. Proville, Dislocation pinning by substitutional impurities in an atomic-scale model for Al (Mg) solid solutions. *Philosophical Magazine*, 2011. 91(11): p. 1581-1606.
63. Poole, W., M. Militzer, and M. Wells, Modelling recovery and recrystallisation during annealing of AA 5754 aluminium alloy. *Materials science and technology*, 2003. 19(10): p. 1361-1368.

64. J., G., P.W. J., M. M., and W.M. A., Modelling recovery and recrystallisation during annealing of AA 5754 aluminium alloy. *Materials Science and Technology*, 2003. 19(10): p. 1361-1368.
65. Marthinsen, K., O. Daaland, and T. Furu, The spatial distribution of nucleation sites and its effect on recrystallization kinetics in commercial aluminum alloys. *Metallurgical and Materials Transactions a-Physical Metallurgy and Materials Science*, 2003. 34A(12): p. 2705-2715.
66. Ahmed, H., M.A. Wells, D.M. Maijer, B.J. Howes, and M.R.v.d. Winden, Modelling of microstructure evolution during hot rolling of AA5083 using an internal state variable approach integrated into an FE model. *Materials Science and Engineering A*, 2005. 390(1-2): p. 278-290.
67. Vandermeer, R.A.a.B.B.R., Modeling recrystallization kinetics in a deformed iron single-crystal. *Metallurgical Transactions Physical Metallurgy and Materials Science*, 1989. 20(3): p. 391-401.
68. Rossi, P.L.O. and C.M. Sellars, Quantitative metallography of recrystallization. *Acta Materialia*, 1997. 45(1): p. 137-148.
69. Peel, M., A. Steuwer, and P. Withers, Dissimilar friction stir welds in AA5083-AA6082. Part II: Process parameter effects on microstructure. *Metallurgical and Materials Transactions A*, 2006. 37(7): p. 2195-2206.
70. Krüger, P., On the relation between non-isothermal and isothermal Kolmogorov-Johnson-Mehl-Avrami crystallization kinetics. *Journal of Physics and Chemistry of Solids*, 1993. 54(11): p. 1549-1555.
71. Cerjak, H. and H.K.D.H. Bhadeshia, *Mathematical Modelling of Weld Phenomena III*. 1997.
72. Burke, J.E. and D. Turnbull, Recrystallization and grain growth. *Progress in Metal Physics*, 1952. 3(0): p. 220-292.
73. Zwieg, T., A Universal Method for the Mechanical Preparation of Aluminium Alloy Specimens with High Edge Retention and their Subsequent Colour Etching. *Praktische Metallographie*, 2001. 32(2).
74. <http://www.oxford-instruments.com/>.
75. Starink, M.J., Analysis of aluminium based alloys by calorimetry: quantitative analysis of reactions and reaction kinetics. *International Materials Reviews*, 2004. 49(3-4): p. 191-226.
76. Rosenthal, D., Mathematical theory of heat distribution during welding and cutting. *Welding journal*, 1941. 20(5): p. 220s-234s.
77. Christensen, N., V.d.L. Davies, and K. Gjermundsen, Distribution of temperatures in arc welding. *British Welding Journal*, 1965. 12(2): p. 54-75.
78. Eagar, T. and N. Tsai, Temperature fields produced by traveling distributed heat sources. *Welding Journal*, 1983. 62(12): p. 346-355.
79. Goldak, J., A. Chakravarti, and M. Bibby, A new finite element model for welding heat sources. *Metallurgical and Materials Transactions B*, 1984. 15(2): p. 299-305.
80. Katsuyama, J., T. Tobita, H. Itoh, and K. Onizawa, Effect of Welding Conditions on Residual Stress and Stress Corrosion Cracking Behavior at Butt-Welding Joints of

- Stainless Steel Pipes. *Journal of Pressure Vessel Technology*, 2012. 134(2): p. 021403-021403.
81. Nguyen, N., A. Ohta, K. Matsuoka, N. Suzuki, and Y. Maeda, Analytical solutions for transient temperature of semi-infinite body subjected to 3-D moving heat sources. *Welding Journal-Including Welding Research Supplement*, 1999. 78: p. 265s-274s.
  82. Wang, Y., *Microstructure Characterisation and Strength Modelling in the HAZ of Al-Mg Alloys*, Ph.D. Metallurgy and Materials School of Engineering. 2007 University of Birmingham, Birmingham
  83. Marthinsen, K., E. Nes, O. Daaland, and T. Furu, The spatial distribution of nucleation sites and its effect on recrystallization kinetics in commercial aluminum alloys. *Metallurgical and Materials Transactions A*, 2003. 34(12): p. 2705-2715.
  84. Li, Y. and L. Arnberg, Evolution of eutectic intermetallic particles in DC-cast AA3003 alloy during heating and homogenization. *Materials Science and Engineering: A*, 2003. 347(1): p. 130-135.
  85. Tanem, B.S., G. Svenningsen, and J. Mårdalen, Relations between sample preparation and SKPFM Volta potential maps on an EN AW-6005 aluminium alloy. *Corrosion science*, 2005. 47(6): p. 1506-1519.
  86. Robert, W., *Corrosion resistance of heat treated and friction stir welded aluminium alloy 5083-H116* Ph.D. Metallurgy and Materials School of Engineering. 2008 University of Birmingham, Birmingham
  87. Jones, R., D. Baer, M. Danielson, and J. Vetrano, Role of Mg in the stress corrosion cracking of an Al-Mg alloy. *Metallurgical and Materials Transactions A*, 2001. 32(7): p. 1699-1711.
  88. Price, C., *The Rapra Collection of DSC Thermograms of Semi-crystalline Thermoplastic Materials*. 1997: iSmithers Rapra Publishing.
  89. Kissinger, H.E., Reaction kinetics in differential thermal analysis. *Analytical chemistry*, 1957. 29(11): p. 1702-1706.
  90. Raghunathan, N., M. Zaidi, and T. Sheppard, Recrystallization kinetics of Al-Mg alloys AA 5056 and AA 5083 after hot deformation. *Materials science and technology*, 1986. 2(9): p. 938-945.
  91. Peel, M.J., A. Steuwer, and P.J. Withers, Dissimilar friction stir welds in AA5083-AA6082. Part II: Process parameter effects on microstructure. *Metallurgical and Materials Transactions A*, 2006. 37(7): p. 2195-2206.
  92. Ahmed, H., M.A. Wells, D.M. Maijer, B.J. Howes, and M.R.v.d. Winden, Modelling of microstructure evolution during hot rolling of AA5083 using an internal state variable approach integrated into an FE model. *Materials Science and Engineering: A*, 2005. 390(1-2): p. 278-290.
  93. Lu, M. and S. Kou, Power inputs in gas metal arc welding of aluminum—Part 1. *Welding Journal*, 1989. 68(11): p. 452S-456S.
  94. DuPont, J. and A. Marder, Thermal efficiency of arc welding processes. *Welding Journal-Including Welding Research Supplement*, 1995. 74(12): p. 406s.
  95. Grong, Ø. and D. Grong, *Metallurgical modelling of welding*. Vol. 2. 1997: Institute of materials London.

96. Goldak, J.A. and M. Akhlaghi, Computational welding mechanics. 2006: Springer.
97. Mills, K.C., Recommended values of thermophysical properties for selected commercial alloys. 2002: Woodhead Publishing.
98. Holmes, T., Characterisation of weld metal microstructure and texture from the the HAZ in fusion welds, Doctor of Philosophy. Metallurgy and Materials. 2007 University of Birmingham, Birmingham